

**RAMAN SPECTROSCOPY OF TERNARY III-V
SEMICONDUCTING FILMS**

DONALD MASHIGO

**Submitted in partial fulfillment of the
requirements of the degree of**

MAGISTER SCIENTIAE

**in the Faculty of Science at the
Nelson Mandela Metropolitan University**

January 2009

Supervisor: Prof. J.R. Botha

Co-supervisor: Mr. J. Jonker

In the loving memory of
Uncle Leslie and Grandma Johanna

ACKNOWLEDGEMENTS

First I would like to express my gratitude to my supervisor, Professor J.R. Botha for giving me the opportunity to be a part of his research group. Also thanks for constant guidance and encouragement throughout my studies.

I also wish to thank my co-supervisor Mr J. Jonker for his valuable assistance and encouragement.

Many thanks to Prof. E.E. van Dyk, Dr. V. Wagener and Miss L. Botha for growing samples used in this study.

A word of thanks to Messrs. D. O'Connor and J. Wessels for the technical assistance.

I am grateful to my fellow students and friends Dr. K.T. Roro, Julien, Chantelle, Nashwa Kharouna, David, Vitalis and Romeo for their outstanding contribution.

I would also like to thank all members of Physics Department for their assistance in completing this thesis.

I want to express my greatest appreciation to my family for their love and support.

The financial assistance from NRF and Nelson Mandela Metropolitan University is gratefully acknowledged.

CONTENTS

SUMMARY.....	vii
CHAPTER 1: INTRODUCTION.....	1
CHAPTER 2: RAMAN SPECTROSCOPY.....	5
2.1 Historical background of Raman spectroscopy.....	5
2.2 Theory of Raman spectroscopy.....	7
2.3 Molecular vibrations.....	14
2.4 Selection rules.....	15
2.5 Raman scattering geometry.....	17
2.6 Applications of Raman spectroscopy.....	19
2.6.1 Stress and Strain.....	19
2.6.2 Crystal orientation.....	19
2.6.3 Temperature determination.....	21
CHAPTER 3: BASIC PROPERTIES OF III-V SEMICONDUCTOR COMPUNDS...	22
3.1 Introduction.....	22
3.2 Properties of III-V semiconductors.....	22
3.2.1 In GaAs.....	22
3.2.2 AlGaAs.....	30
3.2.3 InAsSb and InGaSb.....	31
3.3 Vibrational properties of III-V semiconducting materials.....	35
3.3.1 Introduction.....	35
3.3.2 Local phonon modes.....	35
3.3.3 Mode behaviour of the zone centre optical phonons.....	37
3.3.4 Criteria for mode behaviour.....	38
3.3.5 Previous reports.....	39
CHAPTER 4: STRAIN AND CRITICAL LAYER THICKNESS.....	44
4.1 Introduction.....	44
4.1.1 Strain.....	44
4.1.2 Critical layer thickness models.....	46

<i>van der Merwe</i>	46
<i>Matthews and Blakeslee</i>	46
<i>People and Bean</i>	48
<i>Marée et al.</i>	49
<i>Dodson and Tsao</i>	50
CHAPTER 5: EXPERIMENTAL SETUP AND SAMPLE GROWTH.....	52
5.1 Introduction.....	52
5.2 Raman experimental setup.....	52
5.2.1 Excitation source.....	53
5.2.2 Raman spectrometer.....	54
5.2.3 Detector.....	55
5.3 X-ray Diffraction (XRD).....	58
5.4 Growth of III-V thin films.....	59
5.4.1 $\text{In}_x\text{Ga}_{1-x}\text{As}$	59
5.4.2 $\text{Al}_x\text{Ga}_{1-x}\text{As}$	60
5.4.3 $\text{InAs}_{1-x}\text{Sb}$ and $\text{In}_x\text{Ga}_{1-x}\text{Sb}$	61
CHAPTER 6: RESULTS AND DISCUSSIONS.....	63
6.1. Introduction.....	63
6.2 InGaAs.....	63
6.2.1 Incorporation of indium into the GaAs lattice.....	63
6.2.2 Compositional dependence of optical phonon frequencies.....	64
6.2.3 Variation of strain with layer thickness.....	70
6.2.4 Critical layer thickness.....	75
6.3 InAsSb.....	85
6.3.1 Compositional dependence of optical phonon frequencies.....	85
6.4 InGaSb.....	89
6.4.1 Incorporation of indium into the GaSb lattice.....	89
6.4.2 Compositional dependence of optical phonon frequencies.....	89
6.4.3 Variation in optical phonon frequency with layer thickness.....	92
6.5 AlGaAs.....	93
6.5.1 Compositional dependence of optical phonon frequencies.....	93

CHAPTER 7: CONCLUSIONS.....	97
REFERENCES.....	101

SUMMARY

The III-V semiconductor compounds (i.e. $\text{In}_x\text{Ga}_{1-x}\text{As}$, $\text{InAs}_{1-x}\text{Sb}_x$, $\text{In}_x\text{Ga}_{1-x}\text{Sb}$ and $\text{Al}_x\text{Ga}_{1-x}\text{As}$) have been studied using room temperature Raman spectroscopy. X-ray diffraction has been used as a complementary characterization technique. In this study all the III-V semiconductor compounds were grown by metal organic chemical vapour deposition (MOCVD) on GaAs and GaSb substrates. The layers were studied with respect to composition, strain variation and critical thickness.

Raman spectroscopy has been employed to assess the composition dependence of optical phonons in the layers. The alloy composition was varied, while the thickness was kept constant in order to investigate compositional effects. A significant frequency shift of the phonon modes were observed as the composition changed. The composition dependence of the phonon frequencies were described by linear and polynomial expressions. The results of this study were compared with previous Raman and infrared work on III-V semiconductor compounds.

Strain relaxation in InGaAs and InGaSb has been investigated by Raman and X-ray diffraction. Measurements were performed on several series of layers. For each series, the thickness was varied, while keeping the composition constant. For a given composition, the layer thicknesses were such that some layers should be fully strained, some partially relaxed and some fully relaxed. The Raman peak shifts and XRD confirm that a layer grows up to the critical thickness and then releases the strain as the thickness increases. Critical layer thickness values measured in this study were compared with published data, in which various techniques had been used to estimate the critical thickness.

CHAPTER 1

INTRODUCTION

Over the past few years there has been considerable interest in exploring the fundamental limits of semiconductor device operation. The concept of band gap engineering makes it possible to meet the needs of a particular application. Semiconductor alloys provide a means of tuning the magnitude of the forbidden gap and other material properties with the purpose of optimizing and widening the applications of semiconductor devices (Bouarissa *et al.*, 1995).

The III-V semiconductor alloys of particular interest in this work are based on the binaries GaAs, InAs, GaSb, InSb and AlAs. At present, III-V alloys provide the basis materials for a number of well-established commercial technologies, as well as new cutting-edge classes of electronic and optoelectronic devices, such as photodetectors, heterojunction bipolar transistors, diode lasers, high electron-mobility transistors and modulators.

One of the major advantages of ternary alloys with respect to binary compounds is the possibility to tune, in the range defined by the constituent binaries, their physical properties such as band gap and effective mass, by changing the alloy composition. This has led to a focus on heteroepitaxial systems that are lattice matched. Probably the best two examples are $\text{Al}_x\text{Ga}_{1-x}\text{As}$ latticed matched to GaAs, and $\text{In}_x\text{Ga}_{1-x}\text{As}$ latticed matched to InP (for an indium content x of 0.53). The $\text{Al}_x\text{Ga}_{1-x}\text{As}/\text{GaAs}$ system has been widely used in the fabrication of visible light emitting diodes (LED), laser diodes (LD) and solar cells (Jeganathan *et al.*, 1999). There is considerable interest in low-temperature $\text{Al}_x\text{Ga}_{1-x}\text{As}/\text{GaAs}$ grown for the fabrication of ultrafast optical devices due to their ultrafast carrier recombination (Gau *et al.*, 2002). The $\text{In}_{0.53}\text{Ga}_{0.47}\text{As}/\text{InP}$ system

is widely used in light-emitters for optical fibre communications since its emission wavelength of 1.55 μm is within the optimum transmission window of silica fibers.

The disadvantage of lattice matched systems is that they are very limited in their applications, because the extension of the above mentioned devices requires access to a greater range of heteroepitaxial systems (Hull and Bean, 1992). So the focus has been shifted to lattice-mismatched heteroepitaxial systems in the past two decades. Lattice-mismatched systems provide new prospects, such as the use of strain to modify electronic properties and integration of semiconductor materials with different electronic, optical and mechanical properties (Hull and Bean, 1992).

Even though lattice-mismatched heteroepitaxial systems have been grown successfully, the principal problem is the lack of substrates with suitable lattice parameters. The requirements for epitaxial growth are that the atomic spacing of the layer and substrate must not differ by more than a few percent, and that they have the same crystal structure. Lattice matching imposes a serious constraint on the range of compositions that can be grown on a particular substrate. Traditionally InP and GaAs have provided good templates, but substantial effort has been concentrated on the use of InAs and GaSb as substrates in recent years. The energy gap as a function of lattice constant for ternary III-V compounds, as depicted in figure 1.1, clearly illustrates the limitations imposed by lattice mismatch. Although the composition (and hence the band gap) of ternary systems can be varied over wide ranges, in practice only a limited number of materials of sufficiently high quality are available commercially as substrates (these are indicated by red dots).

Strain that results from lattice mismatch has a significant impact on the fundamental properties and the characteristics of the materials, as it may change the electronic band structure (Adachi, 1992, p. 274). In small structures such as quantum wells and superlattices, the effects of lattice strain can be used to achieve maximum performance. An example of the application of quantum well structures is the strained layer quantum well laser (Fekete *et al.*, 1986).

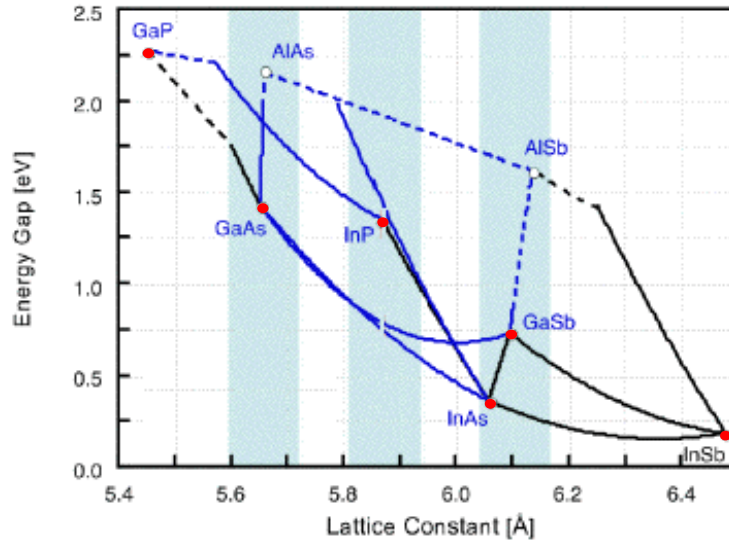


Figure 1.1: Lattice constant versus energy band gap for ternary III-V semiconductors.¹ Solid lines indicate direct band gap and dotted lines indicates indirect band gap. Commercially available substrates are GaAs, InAs, InSb, GaSb, InP and GaP.

Elastic strain in an epitaxial layer can be released by the formation of misfit dislocations at the interface, provided that the layer thickness exceeds a certain critical value. Therefore in order to obtain high performance devices based on lattice-mismatched epitaxial layers, the density of dislocations must be kept at an acceptable level. This study is basically concerned with the limits to which lattice-mismatched epilayers can be grown without the introduction of misfit dislocations. Also in this study the concept of mode behaviour of mixed crystal systems will be discussed. The III-V semiconductor compounds studied are InGaAs, InAsSb, InGaSb and AlGaAs.

¹ http://people.seas.harvard.edu/~jones/ap216/images/bandgap_engineering/bandgap_engineering.html

This dissertation is organized as follows:

In chapter 2, the fundamentals of Raman spectroscopy and its applications are discussed. Material properties of the III-V semiconductor compounds, such as crystal structure, energy band structure and optical vibrational properties are reviewed in chapter 3. In chapter 4, the strain epilayers, the critical layer thickness as well as various models for the prediction of the critical layer thickness, are summarised. In chapter 5, the experimental techniques and procedures used in this study are presented. The results obtained in this study are presented and discussed in chapter 6. Finally, the important conclusions regarding this study are presented in chapter 7.

CHAPTER 2

RAMAN SPECTROSCOPY

In this chapter, the basic theory of Raman spectroscopy will be presented. An historical overview, theory of the Raman effect, molecular vibrations, Raman scattering geometry, as well as the applications of Raman spectroscopy, are discussed.

2.1 Historical background of Raman spectroscopy

The Raman spectroscopy finds its origin in Planck and Einstein's formulation about the dual nature of light (i.e. light is not only wavelike in nature, but it also has a particle nature)². Ever since scientists began thinking about the idea of light as particles, the possibility of inelastic scattering of these particles became a method of proof of this new theory. It was proven by Compton in 1923, that there is an inelastic scattering of x-rays from a graphite target. That very same year, Smekal (1923) theoretically predicted that photons should inelastically scatter from molecular transitions. In 1928, an Indian physicist, C.V. Raman, discovered the optical phenomenon that would later be named Raman scattering (Raman and Krishnan, 1928). He was awarded the Nobel Prize for his discovery in 1930. Raman observed the weak scattering effect by using the sun as the source of light, a telescope as a collector, a narrow band photographic filter to create monochromatic light and a filter to block this monochromatic light. He then noticed that there was a change in frequency as light passed through the filter¹.

Subsequently, a mercury lamp became the principal source of light in Raman scattering experiments. The diagram in figure 2.1 shows the components for observing the Raman phenomena. From the mercury lamp (1) the radiation goes through a filter (2). The monochromatic light obtained is used to illuminate the sample (3). The scattered radiation is observed at an angle of 90 degrees to the incident beam. A glass prism (4) is used to disperse scattered radiation and finally it is recorded on a photographic plate (5).

¹ <http://www.deltanu.com/dn06/tutorials.htm>.

The spectrum is observed on the photographic plate, and is composed of a very strong line (0) corresponding to the incident wavelength (Rayleigh scattered light). On both sides of the strong line are the Raman bands (I, II), for which the wavelengths of the scattered beams are different from that of the incident beam.

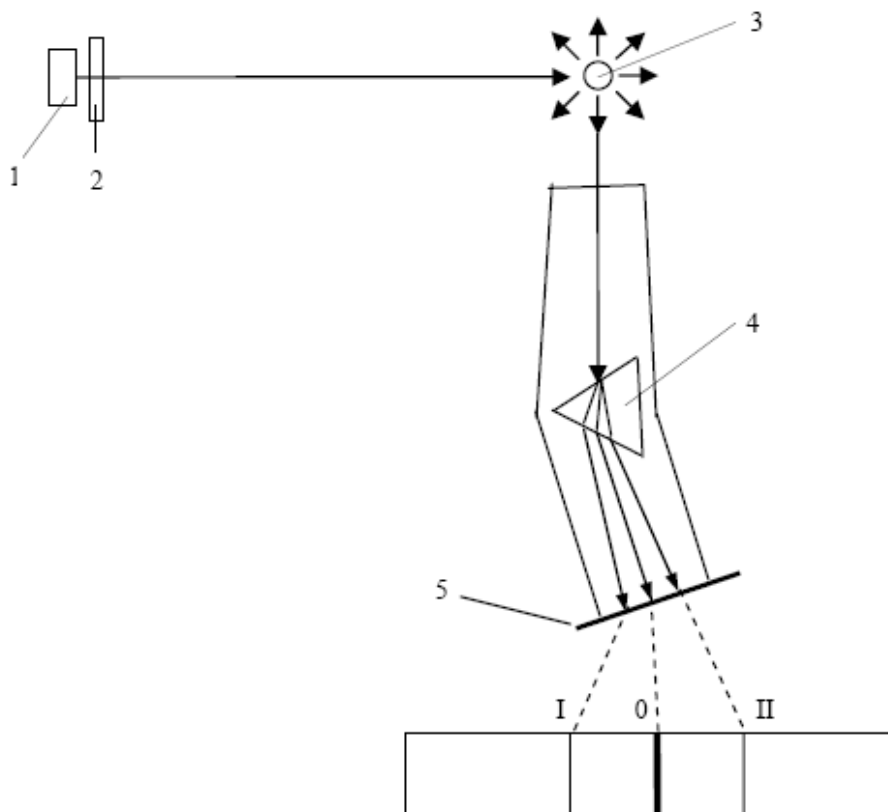


Figure 2.1: The first Raman spectrographs. The diagram illustrates different components used record to Raman spectra. (Baranska *et al.* (1987), p. 10).

Before the laser was invented, mercury arc lamps emitting intense radiation at 435.8 nm and 546.1 nm were used. Samples of relatively large volumes (up to a few ml) were required when using light sources of this type. It was difficult to examine the spectra of

solids and gases under these conditions. The quality of Raman spectra improved with the invention of the laser in 1960 (Maiman, 1960). The advantages of the lasers for Raman spectroscopy also include its monochromatic nature and intensity. In modern Raman spectroscopy, only laser light sources are used (Baranska *et al.* (1987), p. 56).

2.2 Theory of Raman spectroscopy

Oscillating electric and magnetic fields of electromagnetic radiation can interact with a molecule in different ways, for example by scattering or absorption of light (Ingle *et al.* 1988). Raman scattering is the inelastic scattering of electromagnetic radiation by molecular vibrations or optical phonons in a solid. This process of inelastic scattering involves the simultaneous annihilation of incident photons and the creation of scattered photons (Born and Huang, 1954, p. 367). The frequency (ν_0) of the incident photons changes upon interaction with matter, and the frequency of the reemitted photons is shifted up or down with respect to the frequency of the incident photons. This is known as the Raman Effect. For this effect to occur, the laser beam has to be of a particular wavelength so that it is not absorbed by the molecule (Skoog and Leary, 1992).

Absorption occurs if the photon energy corresponds to the difference between two energy levels of the molecule (Baranska *et al.* (1987), p. 12). The requirement for absorption to occur is therefore that the source has to have enough energy to bring the molecule into an excited electronic state. This is illustrated in figure 2.2. The resulting observed light radiating from the sample is in the form of luminescence (Granados, 2003)[♦]. In order to prevent this absorption from occurring, the source must have energy lower than the one required to bring a molecule from the ground state to the lowest excited electronic state (Granados, 2003). Since $E = h \nu = h (c/\lambda)$, where the energy is the product of Planck's constant, h , and the frequency, ν (in hertz), it suggests that a source of light with a longer wavelength would be ideal.

[♦] <http://www.physics.arizona.edu/~thews/reu/Raman%20Spectroscopy.doc>

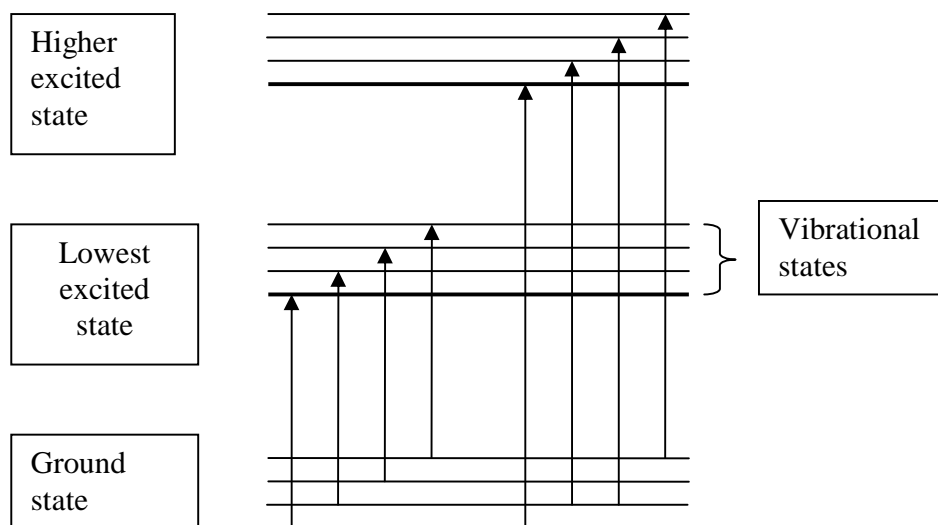


Figure 2.2: Diagram illustrating molecular absorption (adopted from Granados, 2003)[♦].

According to quantum theory, the Raman shift can be explained by considering the exciting light to have photons with energy $h\nu_0$ (Baranska *et al.* (1987), p. 14). When photons collide with a molecule, the molecule is brought to a virtual energy state between the ground state and the lowest excited state. The virtual energy state is not a real energy state, but exists due to a distortion of the electron distribution in a molecule (Pelletier, 1999). The molecule will return to its original state by emitting Rayleigh scattering, with no change in energy. This is illustrated in figure 2.3. Rayleigh scattering is the most intense form of scattering.

[♦] <http://www.physics.arizona.edu/~thews/reu/Raman%20Spectroscopy.doc>

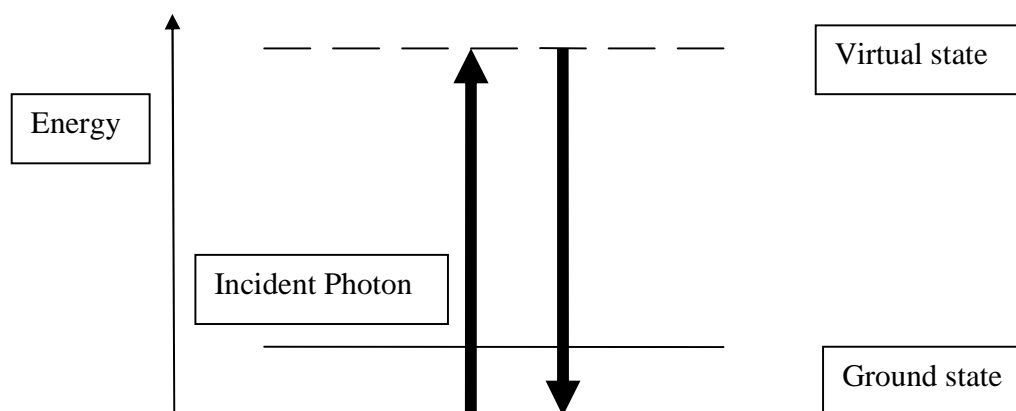


Figure 2.3: Illustration of Rayleigh scattering.

If there is a change in photon energy due to a collision, the molecule leaves the virtual state and ends up in the first excited vibrational energy level of the electronic ground state. Since the energy of the photon has decreased, the wavelength is longer, and this is called Stokes emission (illustrated in figure 2.4a). However, if the molecule is already in an excited vibrational energy level, the collision with the photon can cause the molecule to experience a transition to a lower energy level (Granados, 2003). The photon energy will increase, causing an emission of shorter wavelength, i.e. anti-Stokes emission. This is illustrated in figure 2.4b. Hence, Raman frequency shifts are similar to the changes in energy involved in transitions of the scattering sample and are thus characteristic of a sample (Baranska *et al.* (1987), p. 14).

Actually, Raman frequency shifts correspond to the rotational and vibrational transitions of the molecule which cause the scattering (Ferraro *et al.* (2003), p. 6). Stokes and anti-stokes emissions are symmetric about the Rayleigh line because both correspond to vibrational quanta (Δv) which are either gained or lost by incident photons of radiation. This is shown in figure 2.5 (Ferraro *et al.* (2003), p. 16).

Stokes emission lines are much more intense than the anti-Stokes emission lines at room temperature due to the fact that anti-Stokes transitions can only occur from an excited vibrational state which is less probable to occur than transitions originating from the

electronic ground state. Therefore Raman spectrometry mostly measures the Stokes bands (Baranska *et al.* (1987), p. 15).

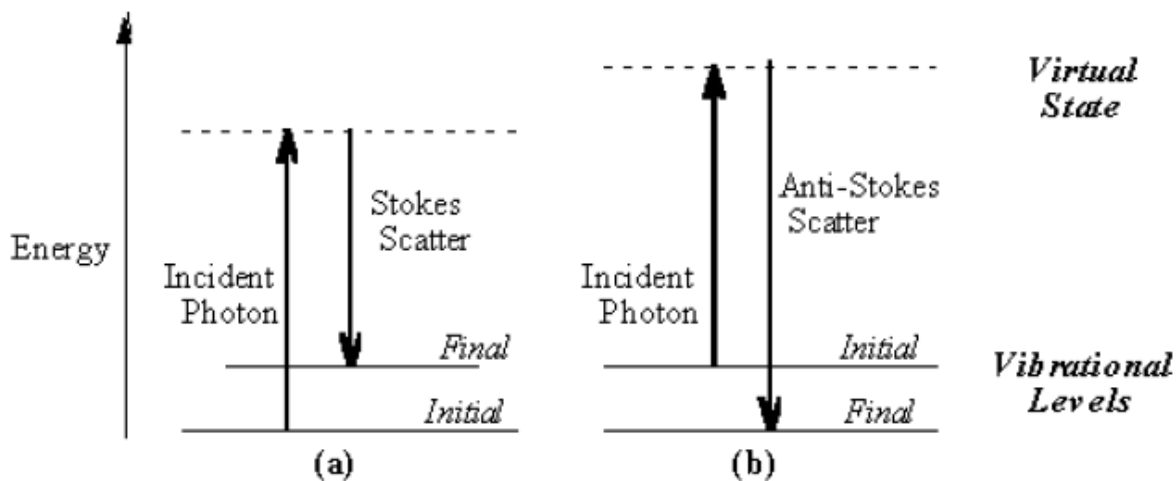


Figure 2.4: (a) Stokes scattering (b) anti-Stokes scattering (Lee and Mousavi, 2004).

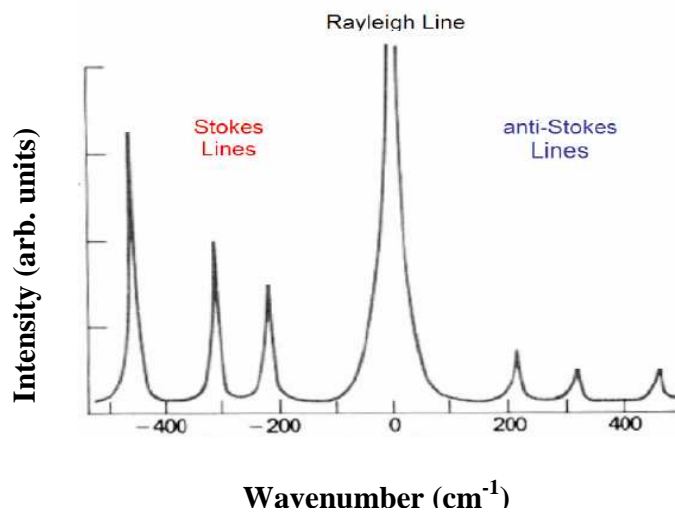


Figure 2.5: Raman spectrum which shows the Rayleigh, Stokes and anti-stokes lines (Ferraro *et al.* (2003), p. 16).

From classical theory, in order for Raman scattering to be observed, there must be electric dipole radiation from a molecule (i.e. the molecule acts as the source of radiation). Generally, inelastic scattering occurs because a dipole is generated when the electric component of light interacts with the molecule (illustrated in Figure 2.6). This means that the polarizability (i.e. distortion of the electron cloud within the molecule) of the molecule must change with the motion (i.e. rotational or vibrational) of the molecule (Baranska *et al.* (1987), p. 18).

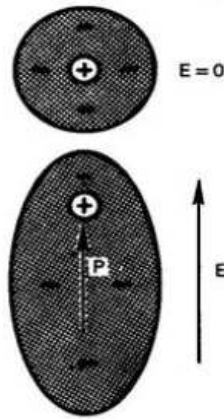


Figure 2.6: Visualization of an induced dipole moment before and after an electric field is applied to an atom (Eckbreth, 1988).

The expression for the induced dipole is given by:

$$\vec{\mu} = \alpha \cdot \vec{E}$$

or

$$\begin{pmatrix} \mu_x \\ \mu_y \\ \mu_z \end{pmatrix} = \begin{pmatrix} \alpha_{xx} & \alpha_{xy} & \alpha_{xz} \\ \alpha_{yx} & \alpha_{yy} & \alpha_{yz} \\ \alpha_{zx} & \alpha_{zy} & \alpha_{zz} \end{pmatrix} \begin{pmatrix} E_x \\ E_y \\ E_z \end{pmatrix} \quad (2.1)$$

where α is the polarizability tensor. Tensors are quantities that transform under change of coordinates (Dettman, 1986). If the molecule is undergoing internal motion, such as vibration or rotation, it can change the polarizability of the molecule (Baranska *et al.* (1987), p. 15-17).

When the electric field vector (\vec{E}) which interacts with the molecule is assumed to be sinusoidal, it is given by the equation:

$$\vec{E} = \vec{E}_0 \cos 2\pi \nu_0 t \quad (2.2)$$

where \vec{E}_0 is the amplitude of the electric field component, ν_0 is the frequency of the wave, and t is time.

Equation 2.1 can be now expressed as follows:

$$\mu = \alpha E_0 \cos 2\pi \nu_0 t \quad (2.3)$$

If the molecule is vibrating with a frequency ν_m , the nuclear displacement Q_k is expressed as:

$$Q_k = Q_0 \cos 2\pi \nu_m t \quad (2.4)$$

where Q_0 is the vibrational amplitude. For small amplitudes of vibration, α is a linear function of Q_k ($k = x, y, z$). The polarizability tensor α , can therefore be expanded:

$$\alpha = \alpha_0 + \left(\frac{\partial \alpha}{\partial Q_k} \right)_0 Q_k + \dots \quad (2.5)$$

where α_0 is the polarizability at the equilibrium position, and $\left(\frac{\partial \alpha}{\partial Q_k} \right)_0$ is the change of the polarizability component α with respect to displacement Q_k relative to the

equilibrium position. If equation 2.4 is substituted into equation 2.5, the following expression is obtained:

$$\alpha = \alpha_0 + \left(\frac{\partial \alpha}{\partial Q_k} \right)_0 Q_0 \cos(2\pi \nu_m t) \quad (2.6)$$

From equations (2.2) and (2.6), we now find the equation which describes the polarizability induced in a molecule with vibrational frequency ν_m , by the incident radiation of frequency ν_0 :

$$\begin{aligned} \mu &= \alpha_0 E_0 \cos(2\pi \nu_0 t) \\ &= \alpha_0 E_0 \cos(2\pi \nu_0 t) + \left(\frac{\partial \alpha}{\partial Q_k} \right)_0 Q_k E_0 \cos(2\pi \nu_0 t) \\ &= \alpha_0 E_0 \cos(2\pi \nu_0 t) + \left(\frac{\partial \alpha}{\partial Q_k} \right)_0 Q_0 E_0 \cos(2\pi \nu_0 t) \cos(2\pi \nu_m t) \end{aligned} \quad (2.7)$$

The trigonometrical identity

$$\cos A \cos B = \frac{1}{2} \cos(A - B) + \frac{1}{2} \cos(A + B),$$

is then applied, to obtain:

$$\mu = \alpha_0 E_0 \cos(2\pi \nu_0 t) + \frac{1}{2} \left(\frac{\partial \alpha}{\partial Q_k} \right)_0 Q_0 E_0 [\cos\{2\pi(\nu_0 - \nu_m)t\} + \cos\{2\pi(\nu_0 + \nu_m)t\}] \quad (2.8)$$

The first term of equation 2.8 corresponds to unchanged scattered light of frequency ν_0 , or Rayleigh scattering. The second term represents Raman scattering with frequency $\nu_0 - \nu_m$ (Stokes) and $\nu_0 + \nu_m$ (anti-Stokes). Thus, the vibrating molecule can be a source of scattered light with three different frequencies (Ferraro *et al.* (2003), p. 15-16).

2.3 Molecular vibrations

In a diatomic molecule, vibration occurs only along the bond connecting the atoms (Ferraro *et al.* (2003), p. 19). For polyatomic molecules the situation is different because there are more possible types of motion. A set of possible atomic motions is known as normal vibrational modes.

To picture these normal vibrational modes, the mechanical model of the CO_2 molecule, illustrated in figure 2.7, is used. Atoms are represented by balls and they are connected together by identical springs. If the C-O springs (i.e. bonds) are stretched and then released at the same time (figure 2.7a), the balls will move back and forth. This motion is known as a symmetric (i.e. in phase) stretching vibration. In the situation where one C-O bond is stretched and the other is compressed (figure 2.7b), antisymmetric (i.e. out of phase) stretching vibration occurs. There is also a third type of motion called bending vibration, which is also symmetric; this is shown figure 2.7c. In this type of motion the balls are moving perpendicular to the direction of the springs. These three types of vibrations have frequencies which are different from each other. However, there are vibrational motions which are different from the three above and that are more complicated. These types of motions involve angular deformations and occur in nonlinear molecules (Davydov, 2003).

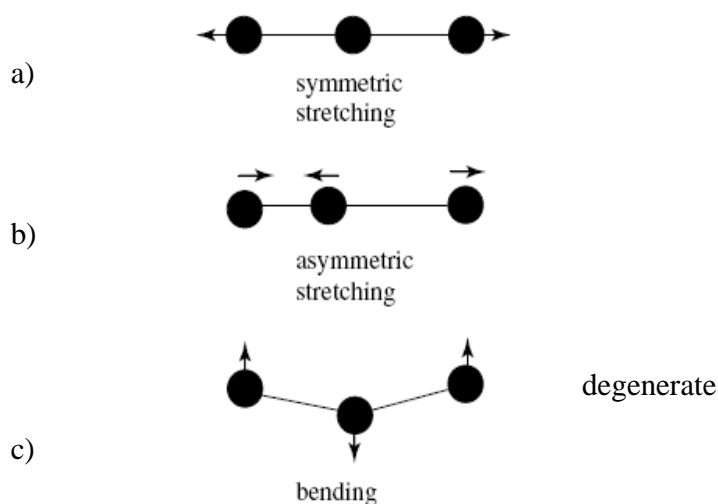


Figure 2.7: Fundamental modes of vibrations in CO_2 (Davydov, 2003).

There are $3N - 6$ fundamental normal modes in a non-linear molecule, where N is the number of atoms (Schroeder, 2002). The six fundamental modes that are subtracted include three translational and three rotational modes. In case of the water molecule (H_2O) for example, there are three modes: $(3 \times 3) - 6 = 3$, where, $\nu_1 = 3652 \text{ cm}^{-1}$, $\nu_2 = 1595 \text{ cm}^{-1}$ and $\nu_3 = 3756 \text{ cm}^{-1}$ (Schroeder, 2002). A linear molecule has $3N - 5$ modes because intra-molecular rotational motion does not exist. There are thus $(3 \times 3) - 5 = 4$ fundamental modes of vibration in case of CO_2 , two of these modes have the same vibrational frequency i.e. they are degenerate.

In order to detect these normal vibrations, Raman and Infrared spectroscopy techniques are used.

2.4 Selection rules

Raman and infrared (IR) spectroscopy both provide information about the vibrational spectrum of a molecule. They consist of sets of vibrational-rotational bands related to the combination of vibrations and rotations of atoms in the molecule. The molecule is characterized by the number, frequency and the amplitude of vibrations. The spectra that are observed from both these techniques show characteristic positions for the bands, that are dictated by the vibrational modes of the molecule (Baranska *et al.* (1987), p. 25).

In IR spectroscopy, light of a certain frequency is absorbed by a molecule. Experimentally it is observed that the light is attenuated when it passes through the sample. In IR spectroscopy, light of infra-red frequencies is passed through a sample and the intensity of the transmitted light is measured at each frequency. This means light absorbed by a sample at a given frequency is determined. In the case of Raman spectroscopy, the light interacts with the vibrating molecule and the changed frequency of scattered light is measured. The two techniques give similar, but complimentary information. They both measure the vibrational energies of molecules, but they rely on different selection rules. These selection rules determine whether the vibrations are active

in IR absorption or Raman scattering. From quantum mechanics, if a vibration causes a change in the dipole moment, the symmetry of the charge distribution has changed (Baranska *et al.* (1987), p. 25), i.e., if $\left(\frac{\partial \mu}{\partial Q_k}\right)_0 \neq 0$, the mode is infrared active. However,

if the vibration causes a change of the molecular polarizability, i.e. if $\left(\frac{\partial \alpha}{\partial Q_k}\right)_0 \neq 0$, it is

Raman active. The selection rules are based on the symmetry of the molecule (Baranska *et al.* (1987), p. 25). According to group theory, phonons or molecular vibrations can be observed either in IR or Raman spectroscopy for crystal lattices or molecules that possess a center of inversion. This is called the rule of mutual exclusion (Baranska *et al.* (1987), p. 25). Molecules or lattices which do not possess a center of symmetry, vibrations can be seen both in Infrared and Raman spectra.

The selection rules for Raman spectroscopy are dependent on the polarizability, α , as shown in the equation:

$$\int \psi^*(\nu') \alpha \psi(\nu) d\tau \quad (2.9)$$

where $\psi^*(\nu')$ represents the excited state and $\psi(\nu)$ corresponds to the ground state of the molecule. If the integrand is totally symmetric, then the integral will be nonzero, which means that the product of the ground state, operator, and the excited state symmetry must be totally symmetric (Ingle *et al.* 1988). This is the selection rule which states that the vibration will only be observed when the polarizability changes during the transition.

In the case of the CO_2 molecule, which is linear as discussed above, it has four degrees of freedom, hence four vibrational modes: symmetrical stretch, antisymmetric stretch and two degenerate bending modes. Only one vibrational mode is observed in the Raman spectrum, namely the symmetric stretch vibration. The other vibrational modes are Infrared active.

2.5 Raman scattering geometry

For modes to be Raman active they have to obey certain symmetry conditions in order to fulfill the selection rules. As mentioned, selection rules are deduced from group theory and are associated with crystal symmetry. These rules associated with crystal symmetry will be discussed with the aid of an example of Raman scattering by optical phonons in zinc-blende crystals.

In a zinc-blende crystal the zone center optical phonon has symmetry Γ_{15} (Yu and Cardona, 1996, p. 366). This is a triply degenerate representation with components denoted as x , y , and z . An optical phonon polarized along the x direction has two nonzero components, denoted by a . This also applies to optical phonons along the y and z directions. The Raman tensors of symmetry Γ_{15} of optical phonons polarized along the x , y , and z directions, are given by (Yu and Cardona, 1996, p. 367):

$$\mathbf{R}_x = \begin{pmatrix} 0 & 0 & 0 \\ 0 & 0 & a \\ 0 & a & 0 \end{pmatrix}, \quad \mathbf{R}_y = \begin{pmatrix} 0 & 0 & a \\ 0 & 0 & 0 \\ a & 0 & 0 \end{pmatrix} \quad \text{and} \quad \mathbf{R}_z = \begin{pmatrix} 0 & a & 0 \\ a & 0 & 0 \\ 0 & 0 & 0 \end{pmatrix} \quad (2.10)$$

Using the Raman tensor defined in (2.10) the selection rules for Raman scattering can be derived for the zinc-blende structure. To describe the Raman scattering geometry and polarization configuration, the notation introduced by Porto (1962) is applied. Raman tensors and vectors are used for this purpose. The vectors are the directions of the incident photon k_L , the scattered photon k_S , the polarization of the incident photon e_L , and the scattered photon e_S . These four vectors define the scattering configurations usually represented as $k_L(e_L, e_S)k_S$. Direction vectors in space are defined as $x \parallel [100]$, $y \parallel [010]$ and $z \parallel [001]$.

For backscattering from a (100) surface the wavevector \bar{q} of the phonon must be along the [100] direction due to wavevector conservation. For the TO phonon, its polarization must be perpendicular to \bar{q} and therefore its Raman tensor is a linear combination of R_y and R_z . The nonzero components of both R_y and R_z impose the requirement that e_L or e_S must have a projection along the x-axis. If both k_L and k_S are parallel to the x-axis, e_L and e_S are both perpendicular to the x-axis, and hence Raman scattering by the TO phonon is not allowed in this geometry. The LO phonon is allowed because its wavevector \bar{q} is along the x-axis and its Raman tensor is given by R_x . For the scattering configuration $x(y,z)\bar{x}$ or $x(z,y)\bar{x}$ the corresponding scattered intensity is proportional to $|a_{LO}|^2$. On the other hand, LO phonon scattering is forbidden in the scattering configuration $x(y,y)\bar{x}$ and $x(z,z)\bar{x}$ (Yu and Cardona, 1996, p. 367). The selection rules and their corresponding scattering configurations are summarized in table 2.1.

Table 2.1 Backscattering configurations in zinc-blende crystals. a_{LO} and a_{TO} denote the nonzero Raman tensor elements for the LO and TO phonons, respectively. y' and z' denote the [011] and $[0\bar{1}1]$ axes (Yu and Cardona, 1996, p. 368).

Surface	Selection rule	
	LO	TO
$x(y,y)\bar{x}$; $x(z,z)\bar{x}$	0	0
$x(y,z)\bar{x}$; $x(z,y)\bar{x}$	$ a_{LO} ^2$	0
$x(y',z')\bar{x}$; $x(z',y')\bar{x}$	0	0
$x(y',y')\bar{x}$; $x(z',z')\bar{x}$	$ a_{LO} ^2$	0
$y'(x,x)\bar{y}'$	0	0
$y'(z',x)\bar{y}'$	0	$ a_{TO} ^2$
$y'(z',z')\bar{y}'$	0	$ a_{TO} ^2$

2.6 Applications of Raman spectroscopy

Among a variety of spectroscopic techniques, vibrational spectroscopy is most widely used in structural characterization. Due to its contactless and non-destructive nature, Raman spectroscopy is one of the most versatile tools in the material sciences. Raman spectroscopy provides a way to determine a variety of sample properties, such as information about the crystal lattice, orientation, structure, composition and stress. The electronic properties, such as the carrier concentration and impurity concentration can also be assessed. Scattering by lattice vibrational modes can be used to characterise semiconductor heterostructures and interfaces (Bauer and Richter, 1996).

2.6.1 Stress and Strain

There are several techniques for measurement of stress and strain, of which Raman spectroscopy is one of the widely used techniques in semiconductors. So the strain in a layer can be monitored through evaluation of the phonon frequencies in the Raman spectrum. It is particularly good in establishing the characteristics of microelectronic devices, because the performance of semiconductor based devices is highly dependent on the knowledge of the stress and the strain in the layer. The determination of the strain is important for the calibration of the growth process and control of the electrical and optical behaviour of the layer. The presence of stress or strain affects the frequencies of the Raman vibrational modes and changes their degeneracies (Cerdeira *et al.* 1972).

2.6.2 Crystal orientation

Raman scattering by crystals provide information on the crystal orientation. The polarization of the Raman scattered light with respect to the crystal and the polarization of the laser light can be used to find the orientation of a crystal. As mentioned in section 2.5, a Raman scattered photon backscatters from crystal plane, such as the growth plane. For example in a zinc-blende-type crystal, the longitudinal optical (LO) vibrational modes are only permitted in the (100) backscattering configuration, while transverse optical (TO) modes are only permitted in the (011) backscattering configuration. Both LO and TO modes are permitted in the (111) configuration.

Figures 2.8 and 2.9 illustrate the Raman spectra of undoped GaAs (100) and GaAs (111), obtained in a pseudo $x(z,z)\bar{x}$ backscattering configuration.

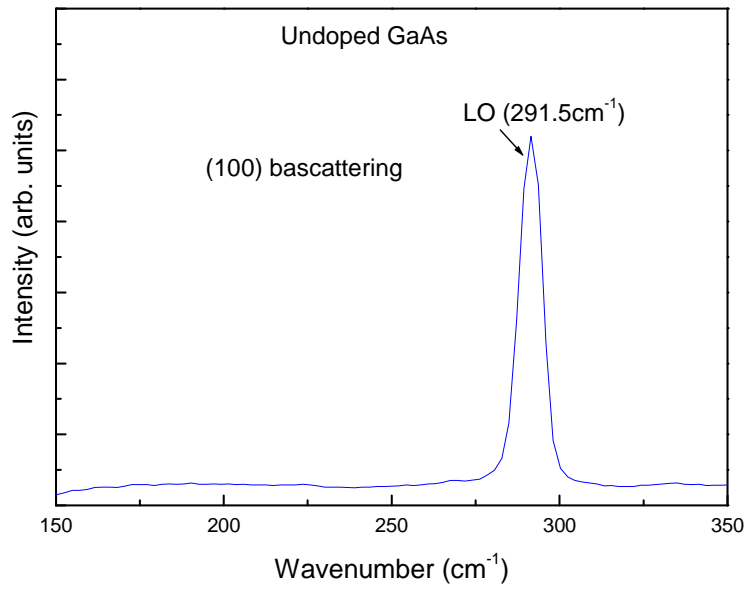


Figure 2.8: Raman spectrum of undoped GaAs (100), showing the LO mode.

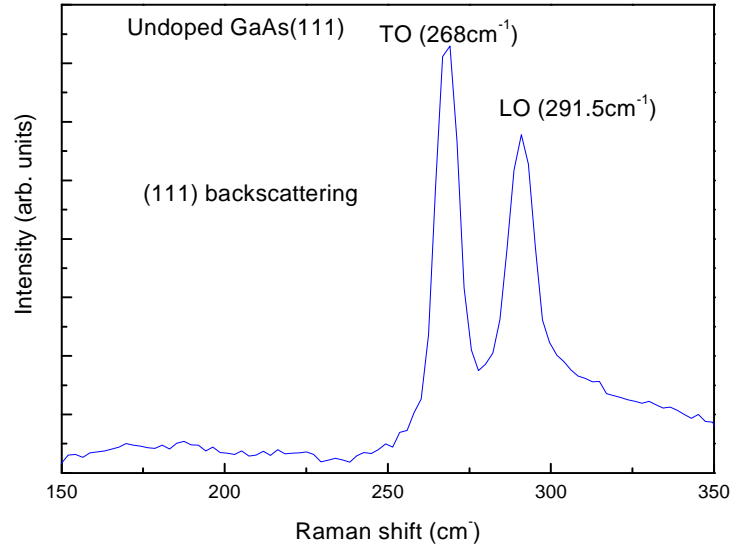


Figure 2.9: Raman spectrum of undoped GaAs (111), showing LO and TO modes.

2.6.3 Temperature determination

Raman spectroscopy can also be used as a tool to determine the temperature of a sample. The temperature of a sample can be estimated from the intensity ratios of the Stokes and anti-Stokes Raman lines by applying the following equation (Ferraro *et al.* (2003), p. 17):

$$\frac{I(\text{Stokes})}{I(\text{anti-Stokes})} = \frac{(\nu_0 - \nu_m)^4}{(\nu_0 + \nu_m)^4} \exp\{hc\nu_m/kT\} \quad (2.11)$$

where ν_0 (cm⁻¹) is the excitation frequency of the laser, ν_m (cm⁻¹) is the Raman shift of the phonon peak, h is Planck's constant, c is the velocity of light, k is Boltzmann's constant, and T is the absolute temperature.

CHAPTER 3

BASIC PROPERTIES OF III-V SEMICONDUCTOR COMPOUNDS

3.1 Introduction

In this chapter, details about the basic properties of the III-V semiconductor compounds relevant to this study will be discussed. Their structural properties and band structures will be presented. The chapter will be concluded with a discussion of optical vibrational properties of these compounds.

3.2 Properties of III-V semiconductors

A great deal of theoretical and experimental work on the III-V compound semiconducting materials have been carried out. Their properties have been reviewed extensively and the reader is referred to literature reviews by Adachi (1992) and a useful more recent compilation, which provides a comprehensive and consistent review of these materials, by Vurgaftman *et al.* (2001).

3.2.1 InGaAs

Crystal structure

Nearly all the III-V semiconducting compounds crystallize in an arrangement where each group III atom is at the centre of a tetrahedron and bound to four group V atoms, one each at the four corners of the tetrahedron (Hilsum and Rose-Innes, 1961). This type of tetrahedral arrangement is called zinc-blende and it is cubic (figure 3.1). The zinc blende crystal consists of two interpenetrating face-centred-cubic lattices, one having an atom from group-III (e.g. Ga) and the other atom from group-V (e.g. As). A zinc blende crystal is characterized by a single lattice constant (Vurgaftman *et al.* 2001).

The semiconductors GaAs and InAs have a zinc blende crystal structure, and the ternary compound $\text{In}_x\text{Ga}_{1-x}\text{As}$ also exhibits the same structure. $\text{In}_x\text{Ga}_{1-x}\text{As}$ exists as a

disordered alloy for the entire compositional range, meaning that atoms are randomly arranged i.e. there is no periodicity (Adachi, 1993). Only five kinds of tetrahedral cells (figure 3.2) are possible (Ichimura and Sasaki, 1986).

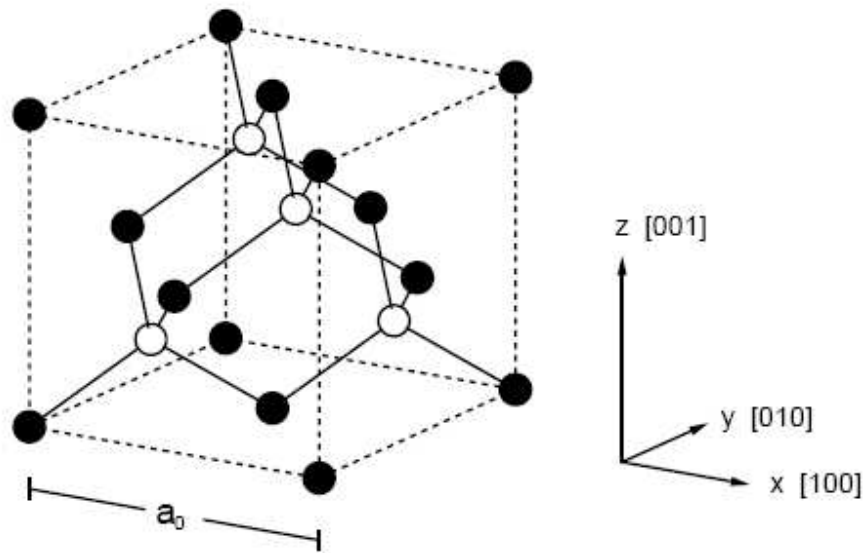


Figure 3.1: Zinc blende crystal structure (Ashcroft, 1976).

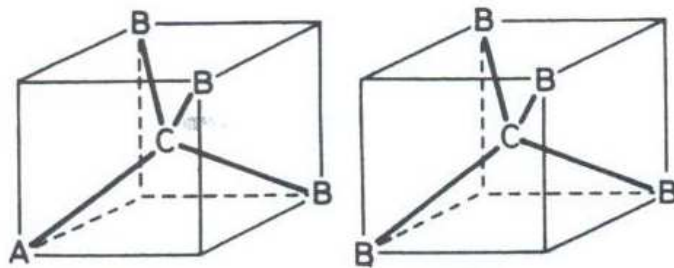
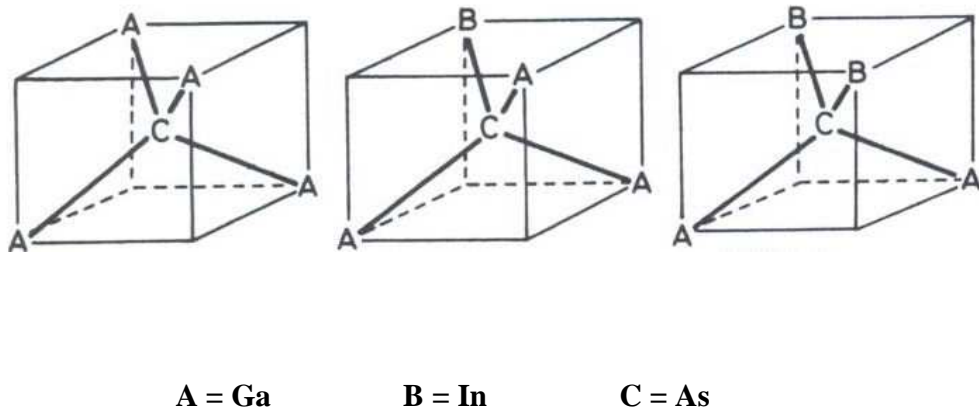


Figure 3.2: Illustration of five possible tetrahedral cells in $\text{In}_x\text{Ga}_{1-x}\text{As}$ (Ichimura and Sasaki, 1986).

In the case of binary end members, X-ray diffraction measurements at room temperature and atmospheric pressure have yielded the lattice constant values with great accuracy. The determined value of the lattice constant at 300 K for GaAs is 5.6532 \AA (Shahid *et al.*, 1987), while that of InAs is 6.0583 \AA at 298.15 K (Ozolinsh *et al.*, 1963). Some fundamental properties of these binaries are summarized in table 3.1.

Due to the random distribution of atoms from the same group within the alloy lattice, precise determination of lattice parameters of the alloy cannot be achieved. A linear interpolation between the lattice constants of the constituent binaries is used rather, for

determining the lattice constant of the alloy. The lattice constant of the ternary system $A_xB_{1-x}C$ is given by Vegard's law expressed as (Vurgaftman, 2001):

$$a(x) = a_0^A x + a_0^B (1 - x) \quad (3.1)$$

The lattice constant as a function of solid composition was found experimentally to vary linearly for $In_xGa_{1-x}As$ alloys. The variation is given by the expression (Adachi, 1982):

$$a = 6.0583 - 0.4050x \quad (3.2)$$

Table 3.1: Room temperature properties of GaAs and InAs.

Properties	Parameter	
	GaAs	InAs
Crystal structure	Zinc blende	Zinc blende
Lattice constant	5.6532 Å	6.0583 Å
Elastic constant (C_{11}) [#]	12.11×10^{10} Pa	8.33×10^{10} Pa
Elastic constant (C_{12}) [#]	5.48×10^{10} Pa	4.53×10^{10} Pa
Density	5.32 g/cm ³	5.68 g/cm ³
Bulk modulus	7.55×10^{11} dyn/cm ²	5.81×10^{11} dyn/cm ²
Sheer modulus	3.26×10^{11} dyn/cm ²	1.90×10^{11} dyn/cm ²
Thermal expansion	5.8×10^{-6} K ⁻¹	4.52×10^{-6} K ⁻¹
Specific heat	0.327 J/g-K	0.25 J/g-K
Thermal conductivity	0.55 W/cm-°C	0.27 W/cm-°C
Dielectric constant	12.85	15.15
Band gap	1.42 eV	0.35 eV
Electron mobility (undoped)	8500 cm ² /V-s	4×10^4 cm ² /V-s

GaAs: (Mikhailova, 1996)

InAs: (Welker, 1952), (Sze, 1981) and (Pierret, 1989)

[#] Tabata *et al.*, 1994

Energy band structure

Both GaAs and InAs are direct band gap materials (figure 3.3(a)), meaning that the minimum of the conduction band is directly above the maximum of the valence band in the momentum space. For transitions between the valence and conduction band to occur, only a change in energy of an electron is needed, and no change in momentum, unlike for an indirect band gap (figure 3.3(b)) material such as silicon (Si). $\text{In}_x\text{Ga}_{1-x}\text{As}$ as an alloy of these binaries is also a direct band gap semiconductor over its entire composition range (Vurgaftman, 2001).

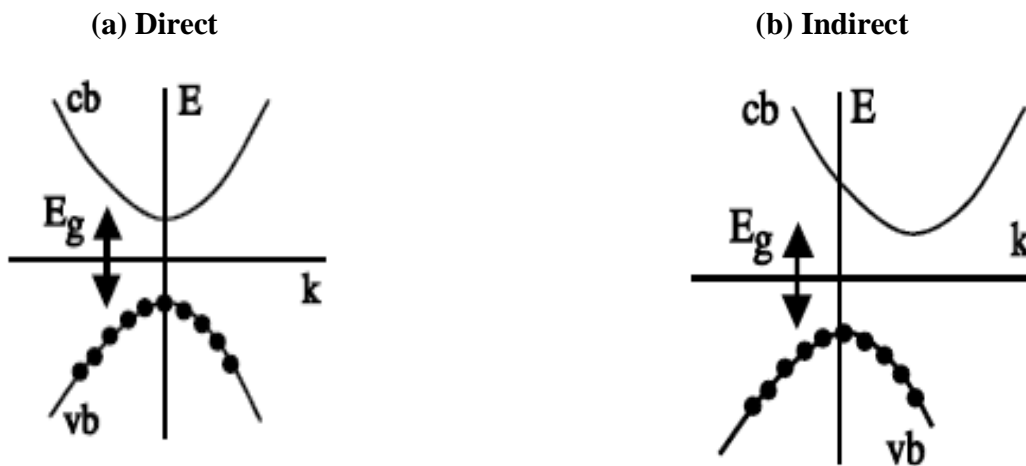


Figure 3.3: Elementary direct (a) and indirect (b) band gap diagrams at 0 K.³

In the III-V ternary systems ($\text{A}_x\text{B}_{1-x}\text{C}$) the dependence of the energy band gap on composition is nonlinear and it is expressed in terms of a quadratic expression (van Vechten and Bergstresser, 1970):

$$E_g(\text{A}_x\text{B}_{1-x}\text{C}) = xE_g^{\text{A}} + (1-x)E_g^{\text{B}} + x(1-x)c \quad (3.3)$$

³ <http://www.ece.rutgers.edu/~maparker/classes/591-LasersChapts/Ch01-Intro/Ch01Sec05BandsTransitions.pdf>

where E_g^A and E_g^B are the energy gaps of the two binaries AC and BC, respectively. In the case of $\text{In}_x\text{Ga}_{1-x}\text{As}$, the energy gaps will be those of InAs and GaAs. The parameter c is called the bowing parameter. The bowing parameter for III-V ternary systems is positive (i.e., the band gap of the alloy is smaller than what a linear interpolation would predict) and can be a function of the temperature (Vurgaftman, 2001).

There have been extensive studies concerning thin film growth on substrates with different lattice constants, particularly in GaAs and InP (Jain *et al.*, 1996). $\text{In}_x\text{Ga}_{1-x}\text{As}$ is subjected to biaxial strain in the plane of the layer, which leads to a tetragonal distortion of the lattice. This will be discussed further in chapter 4.

The strain changes the band gap and causes splitting of the fourfold degenerate valence band into separate light hole and heavy hole bands. These effects are shown in figure 3.4 (Adachi, 1992, p. 274), where k_x lies in the growth plane and k_z lies along the growth direction (Adachi, 1992, p.274). The band gap decreases under tension, while under compression it increases. The change in band gap due to strain can be written as (Asai and Oe, 1983):

$$\Delta E_g \left(\frac{3}{2}; \pm \frac{3}{2} \right) = A_1 \varepsilon \quad (3.4a)$$

$$\Delta E_{\sigma_g} \left(\frac{3}{2}; \pm \frac{1}{2} \right) = A_2 \varepsilon \quad (3.4b)$$

where ε is the strain and its components along (100) directions are given by:

$$\varepsilon_{xx} = \varepsilon_{yy} = \frac{a_0(x) - a_s}{a_s} \quad (3.5)$$

where $a_0(x)$ and a_0 are the layer and substrate lattice constants, respectively. The perpendicular component of the strain is given by (Bauer and Richter, 1996):

$$\varepsilon_{zz} = -2 \left(\frac{C_{12}}{C_{11}} \right) \varepsilon_{xx} \quad (3.6)$$

where C_{11} and C_{12} are the elastic constants which may be obtained by:

$$C_{11} = 11.88 - 3.55x \quad (3.7)$$

and

$$C_{12} = 5.37 - 0.84x \quad (3.8)$$

with x being the indium content (Hornstra and Bartels, 1978).

The parameters A_1 and A_2 are functions of C_{11} and C_{12} , hydrostatic deformation potential a and shear deformation potential b (Jain *et al.*, 1996).

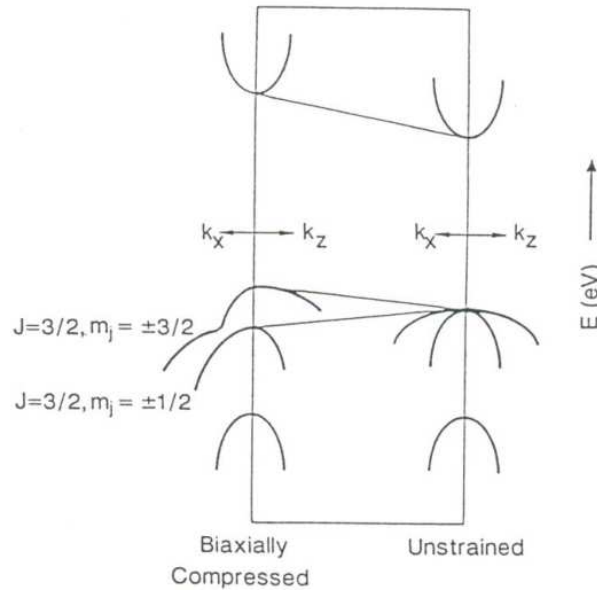


Figure 3.4: Illustration of the effect of biaxial compression on the electronic band structure near the Γ point in $\text{In}_x\text{Ga}_{1-x}\text{As}$ (adapted from Adachi, 1992).

3.2.2 AlGaAs

Crystal structure

$\text{Al}_x\text{Ga}_{1-x}\text{As}$ alloys crystallize in the zinc-blende structure, which consist of two face-centred cubic (fcc) sublattices displaced from each other by one-quarter of a body diagonal. One sublattice is occupied by Al and Ga atoms and the other by As atoms (Kaun *et al.*, 1985).

Energy Band structure

The energy band structure of $\text{Al}_x\text{Ga}_{1-x}\text{As}$ has been studied by various techniques, such as ellipsometry, photoreflectance and photoluminescence (Adachi, 1993). Its vital role in optoelectronic devices requires an exact knowledge of the alignment of the three main conduction valleys (Vurgaftman *et al.* 2001). GaAs is a direct band gap material with Γ - L - X valley ordering, while AlAs is an indirect band gap material with the reverse ordering. This has made the investigation complicated. Most studies have focused on the point where the Γ and X valley minima have the same energies i.e. the so-called cross-over point, where the band gap of AlGaAs becomes indirect (Vurgaftman *et al.* 2001).

Bowing parameters from 0.14 eV to 0.66 eV have been suggested for the Γ -valley energy gap when equation 3.3 is used for the entire composition of $\text{Al}_x\text{Ga}_{1-x}\text{As}$ (Vurgaftman *et al.* 2001). Casey and Panish (1978) proposed that the Γ band gap may be represented at 300 K by linear or quadratic expressions:

$$E_g^{\Gamma}(x) = 1.424 + 1.247x \quad (0 \leq x \leq 0.45) \quad (3.9a)$$

$$E_g^{\Gamma}(x) = 1.4224 + 1.247x + 1.147(x - 0.45)^2 \quad (0.45 < x \leq 1.0) \quad (3.9b)$$

The two indirect gaps, X and L are expressed as:

$$E_g^X(x) = 1.90 + 0.125x + 0.143x^2 \quad (3.10a)$$

$$E_g^L(x) = 1.708 + 0.642x \quad (3.10b)$$

This data indicates that the Γ -X crossover point occurs in the compositional range of $0.4 \leq x \leq 0.5$. Figure 3.5 shows this crossover point in $\text{Al}_x\text{Ga}_{1-x}\text{As}$.

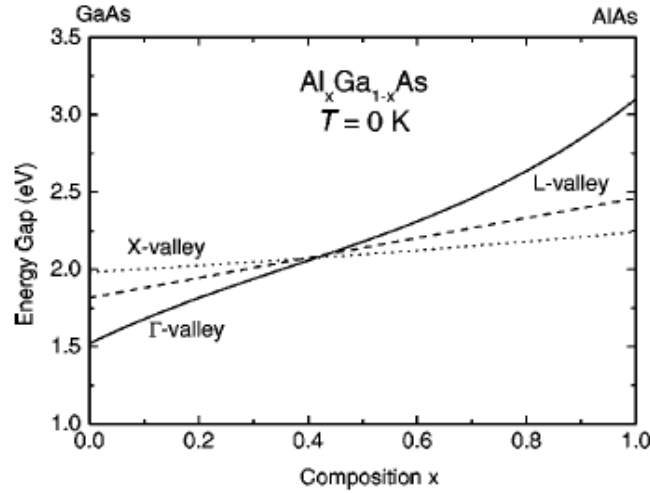


Figure 3.5: Illustration of the cross over point in AlGaAs alloy at $T = 0 \text{ K}$ (Vurgaftman *et al.* 2001).

3.2.3 InAsSb and InGaSb

Crystal structure

Sb-based III-V materials are important for long-wave optoelectronic devices (Woolley and Warner, 1964). A knowledge of the physical properties and intrinsic characteristics, such as band gap and band offsets, is important for the design of devices (Rakovska *et al.* 2000).

As mentioned in section 3.2.1, an interpolation method between the constituent binaries is used to derive the physical properties of ternary alloys. Some of the material properties

of $\text{InAs}_{1-x}\text{Sb}_x$ (Vankova, 2002) and $\text{In}_x\text{Ga}_{1-x}\text{Sb}$ (Goldberg, 1996) are summarised in Table 3.2.

Table 3.2: Basic parameters for $\text{InAs}_{1-x}\text{Sb}_x$ and $\text{In}_x\text{Ga}_{1-x}\text{Sb}$. The free electron mass is denoted by m_0 .

Parameter	* $\text{InAs}_{1-x}\text{Sb}_x$	** $\text{In}_x\text{Ga}_{1-x}\text{Sb}$
Crystal structure	Zinc-blende	Zinc-blende
Density (g. cm^{-3})	$5.68 + 0.09x$	$5.61 + 0.16x$
Dielectric constant (static)	$14.6 + 3.1x$	$15.7 + 1.1x$
Dielectric constant (high frequency)	$11.6 + 5.2x$	$14.4 + 1.3x$
Effective electrons mass m_e^*	$(0.023-0.039x + 0.03x^2) m_0$	$(0.014 + 0.01(1-x) + 0.025(1-x)^2) m_0$
Effective heavy hole mass m_{hh}^*	$(0.40 + 0.03x) m_0$	$(0.40 + 0.03x) m_0$
Effective light hole mass m_{lh}^*	$(0.26 - 0.011x) m_0$	$(0.05 + 0.035x) m_0$
Electron affinity (eV)	$4.9 - 0.31x$	$4.06 + 0.53x$
Lattice constant (\AA)	$6.0584 + 0.420x$	$6.0959 + 0.3835x$
Thermal expansion coefficient α_{th} ($10^{-6}/\text{K}$)	$5.02 + 0.02x$	$7.75 - 2.38x$

** (Goldberg, 1996)

* (Vankova, 2002)

Energy band structure

Antimony based semiconductors represents the smallest bandgap III-V semiconductor materials.

InAsSb

The semiconductors InAs and InSb are both direct band gap materials, and the $\text{InAs}_{1-x}\text{Sb}_x$ ternary system is also a direct band gap semiconductor. $\text{InAs}_{1-x}\text{Sb}_x$ has the lowest band gap among all the III-V semiconductor materials. Previous studies of the

fundamental direct band gap energy, E_g , gave a bowing parameter range between 570 meV and 690 meV ((Thompson and Woolley, 1967), (Yen *et al.* (1988), and Fang *et al.* 1990)). In the review by Vurgaftman *et al.* (2001), a bowing parameter of 670 meV was recommended, giving band gap values in the range $\lambda = 3.5 \mu\text{m}$ ($x = 0$) to $7.1 \mu\text{m}$ ($x = 1$) at 300 K, using equation 3.3.

Recently, Cripps *et al.* (2008) reported on the mid-infrared photo-modulated reflectance (PR) of E_g and Δ (spin-orbit-splitting) transitions in high quality $\text{InAs}_{1-x}\text{Sb}_x$ as a function of composition. The results for the compositional dependence were in good agreement with the bowing parameter recommended by Vurgaftman *et al.* (i.e. $c = 670$ meV at 10K). For Δ , a negative bowing parameter (i.e. -165 ± 30 meV at 10 K) was reported. Figure 3.6 illustrates the results of E_g and Δ as a function of composition. Also included are the results of previous studies ((Berolo and Woolley (1972)); (Coderre and Woolley (1968)) and (Yen *et al.* 1988)).

Figure 3.6a shows the 10 K energy gap of $\text{InAs}_{1-x}\text{Sb}_x$ continuously decreasing with increasing Sb content, and reaching a minimum value for $x = 0.65$. Figure 3.6b shows the results of $\text{InAs}_{1-x}\text{Sb}_x$ spin-orbit splitting energy Δ as a function of Sb composition as determined by PR at 10 K. The dashed curve illustrates the results of Berolo and Woolley (1972) with their positive bowing parameter, which is different from the one reported by Cripps *et al.* (2008).

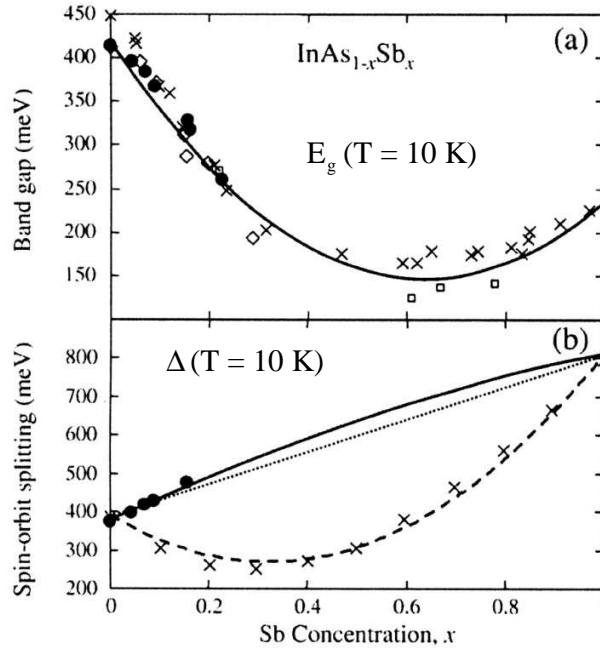


Figure 3.6: The dependence of bandgap of $\text{InAs}_{1-x}\text{Sb}_x$. The solid circles represent the results by Cripps *et al.* (2008) as measured by PR. Also included are results of previous studies of $\text{InAs}_{1-x}\text{Sb}_x$: the crosses are electron-modulated reflectance results of Coderre and Woolley (1968), while the diamonds and squares are photoluminescence results of Berolo and Woolley (1972); and (Yen *et al.* 1988), respectively.

InGaSb

The semiconductors GaSb and InSb are both direct band gap materials, and the $\text{In}_x\text{Ga}_{1-x}\text{Sb}$ ternary system is also a direct band gap semiconductor. The direct energy bandgap of $\text{In}_x\text{Ga}_{1-x}\text{Sb}$ can be tuned in the range 1.7- 6.8 μm by varying the indium composition for infrared applications (Murakami *et al.* 2005). Figure 3.7 shows a lowering in the energy band gap when the indium content increases.

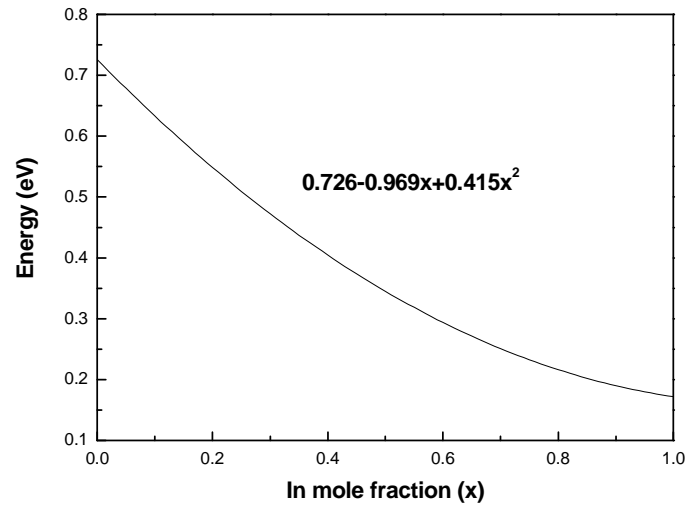


Figure 3.7: The room temperature dependence of band gap energy of $\text{In}_x\text{Ga}_{1-x}\text{Sb}$ ternary system on In composition.

3.3 Vibrational properties of III-V semiconducting materials

3.3.1 Introduction

In this section some of the vibrational properties of III-V semiconducting materials are discussed. The symmetry of a perfect pure lattice is broken when defects are introduced. The introduction of defects into a pure crystal can be viewed as causing shifts in its vibrational states. The new vibrational states serve as a tool for examining both the defects and the host lattice (Barker and Sievers, 1975).

3.3.2 Local phonon modes

The presence of the substitutional impurity atoms with a mass different from those of the host lattice will (a) slightly perturb the frequencies of the normal vibrational modes, and

(b) create vibrational states within the forbidden frequency range (see figure 3.8) below the optical branch and above the acoustic branch (Barker and Sievers, 1975). Such a frequency mode is well away from the band of normal frequencies of the host crystal. This has led to the term “localized mode” (Barker and Sievers, 1975). This localized mode lies above the optic mode band of the host lattice. The localized vibrational state will also appear if the impurities have the same mass as the host crystal, but different charge. In general, impurities have different mass and charge compared to the host crystal. The distortion of the symmetry of the pure lattice by the introduction of impurities makes it possible for the electric vector associated with an electromagnetic field to interact with localized vibrational modes (Barker and Sievers, 1975). Hence, when the symmetry is distorted it is possible for the electromagnetic wave to interact with (slightly shifted) normal vibrational modes of the crystal (Barker and Sievers, 1975).

Localized mode studies have been used as a method to identify the impurity type and actual location in the lattice.

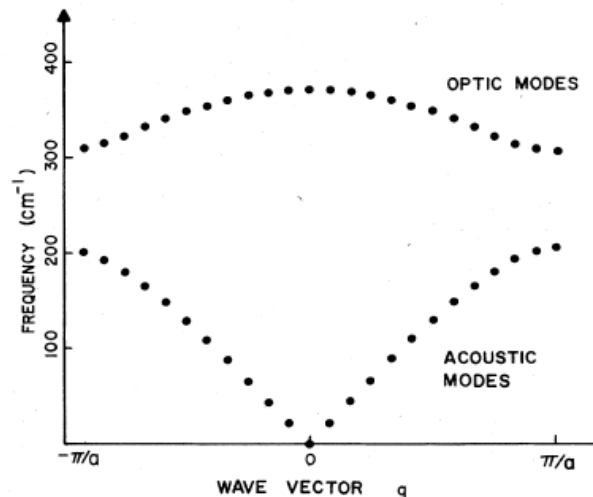


Figure 3.8: Dispersion relationship for propagation of a longitudinal wave in a linear diatomic lattice (Barker and Sievers, 1975).

3.3.3 Mode behaviour of the zone centre optical phonons

In a mixed crystal $A_xB_{1-x}C$, the concentration (mole fraction x) dependence of the zone centre optical phonon frequency exhibits one-, two- or intermediate (mixed) mode behaviour, which depends on the relative masses of the constituent atoms and the interatomic force constants (Barker and Sievers, 1975). These mode behaviours are illustrated in figure 3.9. For one-mode behaviour, the optical phonon frequency varies as the alloy composition varies from one end member to the other (i.e. AC to BC), with the mode intensity remaining almost constant. For two-mode behaviour, two distinct sets of optical modes exist, with frequencies characteristic of each member and intensity approximately proportional to the mole fraction x of the component it represents (Chang and Mitra, 1968). In the case of intermediate mode or mixed mode behaviour, a band which is intermediate to that observed in the one- or two- mode cases, occurs. This behaviour is characterised by a single mode (AB or AC) over only a part of the composition range, while two modes are observed over the remaining range of the composition (Adachi, 1993).

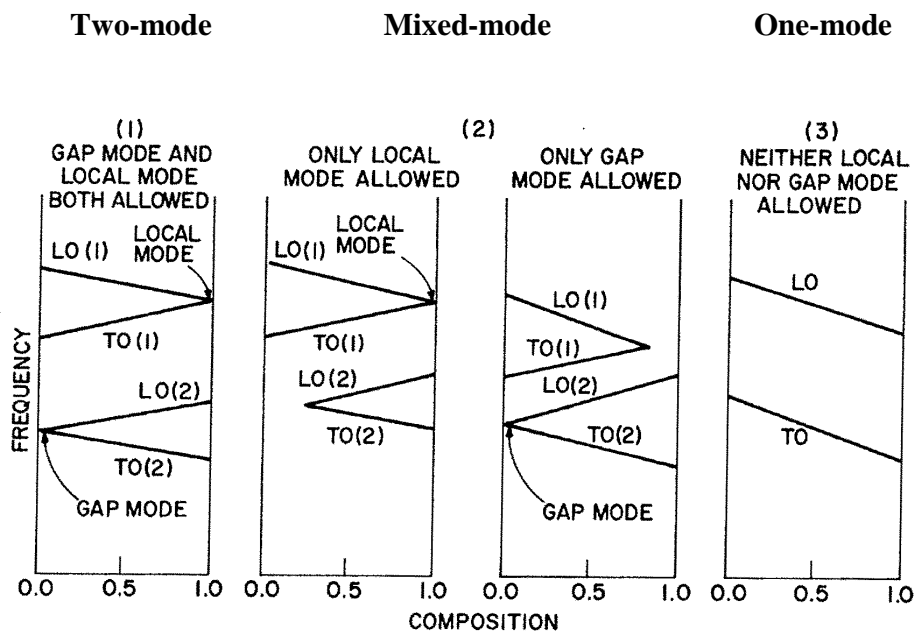


Figure 3.9: Schematic representation of the mode behaviour in mixed crystals (Brodsky *et al.*, 1970).

3.3.4 Criteria for mode behaviour

Many attempts have been made to account for the mode behaviour of mixed crystal systems. A linear diatomic chain model was proposed by Matossi (1951), in which only nearest-neighbour force constants are considered to explain the one-mode behaviour of $K_xNa_{1-x}Cl$. This model is idealized with a periodic regular distribution of A and B atoms in the $A_xB_{1-x}C$ ternary system, whereas the true distribution is believed to be random. For this model, only a 50-50 mixed case was considered. The calculation for $K_xNa_{1-x}Cl$ yielded two infrared-active modes: one was found between the interval of frequencies of the two binary members (i.e. NaCl and KCl); the other one lay outside this interval (Chang and Mitra, 1968).

Barker and Verleur (1967) proposed a simple model to account for the one-mode behaviour of $Sr_xBa_{1-x}F_2$. Using six fitting parameters, they showed that the model could yield one-mode or two-mode behaviour, depending on the values of certain parameters. It was also shown that one-mode behaviour resulted from the approximate equality of the mode frequencies of pure BaF_2 and SrF_2 binaries. The problem with this model is that this criterion does not seem to hold well for $GaAs_{1-x}Sb_x$, where the optical frequencies of the binaries are well separated, yet the mixed ternary system exhibits one-mode behaviour.

Brodsky and Lucovsky (1968) reviewed the models which have been used to explain the variation of the observed vibrational frequencies with concentration. They proposed criteria which are based on whether or not localized mode and gap-mode occur when predicting the behaviour of the phonons of mixed crystals. The gap mode is an impurity mode that lies below the optic band of the host lattice.

The criteria are based on the mass of the substituting ion in a mixed crystal. The mixed crystal system $A_xB_{1-x}C$ was considered. The criteria for two-mode behaviour are those that permit a localized mode above the optical branch of AC and a gap mode between the acoustical and optical branches of BC to exist for small alloy concentrations. GaAs does

not exhibit this gap (Dolling and Waugh, 1965), hence any alloy of GaAs with a binary having a larger cation mass (e. g. InAs) should not display two-mode behaviour over the entire composition range.

From the above discussion, the criterion for one-mode behaviour is that gap and localized modes do not exist for small concentrations of substitutional ions; hence the formation of the second mode is prevented. In a mixed crystal such as InGaAs, the criterion for one- or two mode behaviour are not satisfied, and hence the intermediate (mixed mode) behaviour is observed (Brodsky and Lucovsky, 1968).

Chang and Mitra (1971) summarized the determining conditions for the mode behaviour in a mixed crystal by using the mass difference theory. In a two-mode system, the mass of the substituting element, M_B , must be smaller than the reduced mass of the compound in which the substitution is been made, μ_{AC} , defined by:

$$\frac{1}{\mu_{AC}} = \frac{1}{M_A} + \frac{1}{M_C} \quad (3.11)$$

Mixed crystals which obey the inequality $M_B < \mu_{AC}$ exhibit two-mode behaviour, whereas the opposite is true for one-mode behaviour.

3.3.5 Previous reports

Raman scattering has been performed on III-V ternary alloys by several investigators to identify modes and relate these modes to composition.

In_xGa_{1-x}As

The first investigation on In_xGa_{1-x}As was done by Brodsky and Lucovsky (1968) using infrared reflectivity at room temperature on thick (12 to 102 μm) layers. They observed two-mode behaviour at the In rich end of the alloy system, one-mode behaviour near the Ga rich end, and a transition between the two at intermediate frequencies. They stressed the variation in the frequencies of the LO and TO phonons as a function of composition,

in particular the decrease in the GaAs-like LO and TO phonon frequencies with increasing composition of In.

Lucovsky and Chen (1970) conducted a study of the infrared reflectivity of both lower indium content ($x = 0.16, 0.25, 0.47$) and also higher indium content ($x = 0.84, 0.92$) layers. For the higher indium content, only one infrared band was observed, whereas in other layers there were two modes (i.e., the alloy displayed mixed mode behaviour). A shoulder near 260cm^{-1} was also observed in the layers with $x = 0.84$ and 0.92 . This shoulder was attributed to disorder within the layer.

Yamazaki *et al.* (1980) studied the infrared reflectivity of $\text{In}_x\text{Ga}_{1-x}\text{As}$ over the entire composition range. The samples studied were single-crystalline films grown on semi-insulating GaAs substrate. They observed only one infrared band (GaAs-like) for $x \geq 0.8$ and two bands for the remaining range of composition. The data were analyzed by using the Kramers-Kronig relationship, and the dependence of the mode frequencies on the alloy composition was interpreted based on the modified cluster model. It was found that the model qualitatively explains the composition dependence of the phonon frequencies in both the one- and two- mode regions.

Emura *et al.* (1988) conducted Raman studies on $\text{In}_x\text{Ga}_{1-x}\text{As}$ over a wide range of the alloy composition ($0 < x < 1$). The samples were grown epitaxially by molecular beam epitaxy on InP (100) substrates. Their results using Raman spectra from the In rich samples support the conclusion that this alloy system displays a mixed mode behaviour. The variations in the Raman mode frequency were found to be nonlinear with composition; the expressions are given by:

$$\nu_{\text{InAs(LO)}} (\text{cm}^{-1}) = 234.9 - 7.7x + 8.92x^2 \quad (3.12a)$$

$$\nu_{\text{InAs(TO)}} (\text{cm}^{-1}) = 233.7 - 16.5x \quad (3.12b)$$

$$\nu_{\text{GaAs(LO)}} (\text{cm}^{-1}) = 290.0 - 18.6x - 32.4x^2 \quad (3.12c)$$

$$\nu_{\text{GaAs(TO)}} (\text{cm}^{-1}) = 265.1 - 5.3x + 29.0x^2 \quad (3.12d)$$

Estrera *et al.* (1992), identified the four allowable vibrational modes in $\text{In}_x\text{Ga}_{1-x}\text{As}$ on InP using Raman scattering off the (100) normal surface and the (011) cleaved plane. The molecular beam epitaxially grown samples were 1.0-1.5 μm thick. They reported a linear compositional variation, given by the following expressions:

$$\nu_{\text{InAs(LO)}} (\text{cm}^{-1}) = 240.4 - 15.5x \quad (3.13a)$$

$$\nu_{\text{GaAs(LO)}} (\text{cm}^{-1}) = 261.7 + 15.8x \quad (3.13b)$$

$$\nu_{\text{GaAs(TO)}} (\text{cm}^{-1}) = 252.5 + 5.6x \quad (3.13c)$$

for the (100) backscattering configuration, and

$$\nu_{\text{InAs(TO)}} (\text{cm}^{-1}) = 236.5 - 24.0x \quad (3.13d)$$

$$\nu_{\text{GaAs(TO)}} (\text{cm}^{-1}) = 247.2 + 15.7x \quad (3.13e)$$

for the (011) backscattering configuration.

A mode at 244cm^{-1} , which was attributed to alloy disorder, was observed in these films and was verified by Pearsall *et al.* (1983).

Strain relaxation has been investigated by means of Raman scattering in strained samples over the entire range ($0 < x < 1$) by Groenen *et al.* (1997). The samples were grown on InP (100). A marked dissymmetry in strain relief was found over the whole composition range between equivalent tensile and compressive misfits. Disorder activated Raman peaks were analyzed and correlated to the structural defects resulting from the strain relief.

Very recently, Bellani *et al.* (2007) investigated the strain relaxation mechanism in $\text{In}_x\text{Ga}_{1-x}\text{As}$ metamorphic buffers grown on GaAs substrate. The residual strain was measured using Raman scattering and X-ray diffraction. The results of Raman and XRD measurements were in satisfactory agreement. The strain values versus thickness were compared to the results of strain relaxation models; the experimental results confirmed the validity of the energy-balance model by Marée *et al.* (1987).

$\text{Al}_x\text{Ga}_{1-x}\text{As}$

The first investigations of the compositional dependence of the optical phonons in $\text{Al}_x\text{Ga}_{1-x}\text{As}$ were done by Ilegems and Pearson (1970), using infrared reflectivity. The samples were grown on (111) oriented GaAs. The thickness of the samples varied between 50 and 100 μm . Two distinct reststrahlen bands with frequencies near those of pure GaAs and pure AlAs were observed over the entire compositional range. These observed bands shifted to lower frequencies, and decreased in amplitude as the composition of the corresponding compound in the alloy was decreased. The data were analyzed using the Kramers-Kronig technique, the modes were traced from binary compounds, where the vibrational modes are the fundamental lattice reststrahlen modes, through to the range of composition where the modes become local or impurity modes. The shift in mode frequencies was interpreted on the basis of the random isodisplacement model (Ilegems and Pearson, 1970).

Kim and Spitzer (1979) studied thick layers (150 μm) with uniform composition. Infrared reflectivity and Raman scattering measurements were performed. A two-mode behaviour was confirmed and a nonlinear dependence of the modes on composition was reported. Atomic disorder induced effects were observed in Raman scattering near 200 cm^{-1} .

Guo *et al.* (2002) reported the observation of resonant Raman scattering in a low-temperature-grown $\text{Al}_{0.29}\text{Ga}_{0.71}\text{As}/\text{GaAs}$ sample. Two laser lines, 632.8 nm and 488 nm, were used to detect scattering from different regions at different depths. Raman scattering

was used to investigate the crystalline characteristics and defect-related features in as-grown and post-annealed AlGaAs material. All the higher order resonant peaks were assigned according to their fundamental modes. From their results they showed that Raman scattering performed at low temperature can be used to probe weak local ordering and disordering.

InAs_{1-x}Sb_x

The first Raman scattering investigations of InAs_{1-x}Sb_x were performed by Cherng *et al.* (1988). The layers were grown by organometallic vapour phase epitaxy on InAs (100) and InSb (100) substrates over the entire compositional range. A one-mode behaviour was reported for all compositions with $x \leq 0.6$, and two mode behaviour for larger values of x . The InAs_{1-x}Sb_x ternary alloy was therefore concluded to be a one-two-mode or mixed mode system. Disorder-activated acoustic and optical modes were also reported.

Li *et al.* (1992) studied InAs_{1-x}Sb_x ternary alloys, grown on GaAs by molecular beam epitaxy using Raman scattering. From their Raman studies, two-mode behaviour was reported: both InAs-like LO and InSb-like LO peaks were observed throughout the entire compositional range. The frequency dependence on composition was found to be linear for all the observed modes. Weak peaks of unknown origin (at 154 cm⁻¹ and 138 cm⁻¹) and a shoulder between the InAs-like LO peak and InSb-like peak for $x \sim 0.6$ were observed. This shoulder which is due to disorder-activated phonons, was also reported by Cherng *et al.* (1988).

In_xGa_{1-x}Sb

Brodsky *et al.* (1970) reported room temperature infrared reflectivity for the In_xGa_{1-x}Sb ternary system. Their spectra were similar to those obtained for In_xGa_{1-x}As and helped to explain the general nature of two-mode behaviour and to define the criteria for its occurrence. For $x < 0.30$, one reflectance band was observed, while for samples with indium mole fraction $x > 0.30$, two bands were observed. As the composition increased, a frequency shift from the GaSb to InSb reststrahlen regions was observed.

CHAPTER 4

STRAIN AND CRITICAL LAYER THICKNESS

4.1 Introduction

Strain has an important influence on the physical properties of semiconductor films, and it provides a way to engineer the band structure and modify optical and transport properties of semiconductors. Band edges can be controlled by adjusting the strain; in this way improved heterostructure devices can be designed, for example optical detectors and bipolar transistors (Jain *et al.*, 1996).

4.1.1 Strain

A pseudomorphic epilayer can be grown on a substrate of different lattice constant provided that the layer is thin enough. Figure 4.1 illustrates an epilayer grown on an infinitely thick substrate with a different lattice constant (e.g. InGaAs grown on GaAs). If the lattice constant of the epilayer is different from that of a substrate, the misfit between them will be accommodated by a tetragonal distortion of the unit cell of the layer, as illustrated in figures 4.1(a) and 4.1(b). If the lattice constant of an epilayer is larger than that of the substrate it will be compressed in the plane of the interface, while along the direction normal to the growth plane, the lattice constant will be increased.

An epilayer can remain coherent i.e. totally elastically strained (figure 4.1(b)) as long as its thickness, h , does not exceed a certain thickness called the critical thickness, h_c . If the critical thickness is exceeded, misfit strain will be relaxed partially by the introduction of misfit dislocations, as illustrated in figure 4.1(c). If the thickness of the layer is further increased, the epilayer will relax towards its bulk structure and it will be completely relaxed (i.e. no strain). This is illustrated in figure 4.1(d).

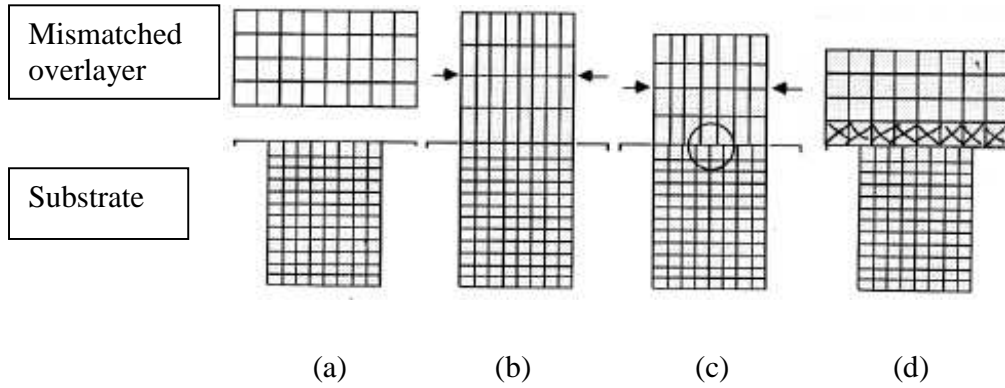


Figure 4.1: Structure of an epilayer under biaxial compression, (a) mismatched (b) strained (c) partially relaxed and (d) completely relaxed^Y.

The lattice match (misfit), f , is defined by the following equation (Jain *et al.*, 1996):

$$f(x) = \frac{a_l(x) - a_s}{a_s} \quad (4.1)$$

where $a_l(x)$ and a_s are the lattice constants of the epilayer and the substrate, respectively. As mentioned in section 3.2.1, the lattice constant of the epilayer can be determined from Vegard's law.

The in-plane strain in the x and y directions are given by (Jain *et al.*, 1996):

$$\varepsilon_{xx} = \varepsilon_{yy} = -f(x) \quad (4.2)$$

The strain in the perpendicular direction is given by (Jain *et al.*, 1996):

$$\varepsilon_{zz} = \frac{2C_{12}}{C_{11}} f(x) \quad (4.3)$$

^Y http://eeclass.stanford.edu/cgi-bin/handouts.cgi?s=&t=1188608741&cc=ee327&action=handout_download&handout_id=ID11765171134973&viewfile=EE327_Lecture_4.pdf.

4.1.2 Critical layer thickness models

There have been many attempts to model the critical thickness for the introduction of misfit dislocations in the epitaxial layer. In this section various models for the calculation of critical angle will be presented.

van der Merwe

The existence of the critical thickness was first detailed by van der Merwe. A thermodynamic model by van der Merwe (van der Merwe, 1963) describes the critical thickness by analyzing the energy of the system as it is minimized by the generation of a periodic array of dislocations. The critical thickness is given by the expression:

$$h_c \approx \left(\frac{19}{16\pi^2} \right) \left(\frac{1+\nu}{1-\nu} \right) \frac{b}{f} \quad (4.4)$$

where ν is Poisson's ratio and is given by:

$$\nu = \frac{C_{12}}{C_{11} + C_{12}} \quad (4.5)$$

and b is the magnitude of the Burger's vector, which is given by:

$$b = \frac{a}{\sqrt{2}} \quad (4.6)$$

Matthews and Blakeslee

The Matthew and Blakeslee model (1974) is widely accepted to realistically predict the critical layer thickness (Hull and Bean, 1992). This model is based on mechanical equilibrium theory. In this model, a threading dislocation elongates to form a misfit dislocation segment due to mismatch stress, and the critical thickness is estimated from the forces acting on these dislocations. The forces applied are F_a , which acts to elongate

the threading dislocation in the interface due to the misfit strain; and the line tension F_T , which resists the elongation of the dislocation. This is schematically illustrated in figure 4.2.

There are three stages of threading dislocation evolution which have been predicted (Hull and Bean, 1992). In stage 1, where $h < h_c$, the threading dislocation line will propagate through the epilayer and the interface remains coherent (illustrated in figure 4.2(a)). In stage 2, where $F_a = 2F_T$, the dislocation becomes bowed (illustrated in figure 4.2(b)). Finally, in stage 3, where $F_a > 2F_T$, the threading dislocation elongates along the plane of the interface, producing a misfit dislocation segment (illustrated in figure 4.2(c)).

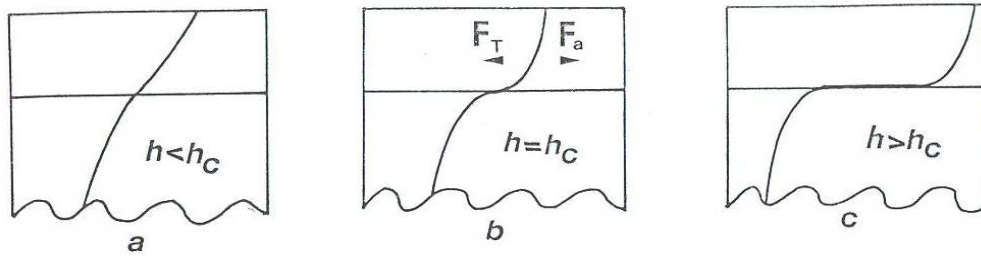


Figure 4.2: Schematic illustration of the Matthews and Blakeslee model of critical thickness (after Hull and Bean, 1992).

The applied force is given by the following equation (Hull and Bean, 1992):

$$F_a = 2Gbhf \frac{1+\nu}{1-\nu} \cos \lambda \quad (4.7)$$

where λ is the angle between the Burgers vector and that direction in the interface that is perpendicular to the line of intersection of the slip plane and the interface. The line tension is given by the following equation (Hull and Bean, 1992):

$$F_T = \frac{Gb^2(1-\nu \cos^2 \theta)}{4\pi(1-\nu)} \ln\left(\frac{h}{b}\right) \quad (4.8)$$

where θ is the angle between the Burgers vector and the length of the dislocation line that lies in the interface normal to the line of intersection of the slip plane and the interface.

Equating equations 4.7 and 4.8, the equation for the critical layer thickness for a single layer is (Hull and Bean, 1992):

$$h_c = \frac{b(1-\nu \cos^2 \theta)}{8\pi f(1+\nu) \cos \lambda} \ln\left(\frac{h_c}{b}\right) \quad (4.9)$$

People and Bean

People and Bean (1985) in their approach considered the critical thickness based on the local strain energy density necessary for the nucleation of misfit dislocations (Hull and Bean, 1992). Their approach differs from that of Matthews and Blakeslee, in which mechanical equilibrium of a preexisting threading dislocation determines the onset of interfacial misfit dislocations. In this model, it is assumed that the growing epilayer is initially free of threading dislocations and that interfacial misfit dislocations will be generated when areal strain energy density E_H exceeds the self energy of an isolated dislocation such as a screw or edge dislocation (People and Bean 1985).

People and Bean's energy balance model gives the critical thickness as (Orders and Usher, 1987)

$$h_c = \frac{(1-\nu)b}{(1+\nu)32\pi f^2} \ln\left(\frac{h_c}{b}\right) \quad (4.10)$$

Marée et al.

Marée *et al.* (1987) in their approach for the calculation of critical thickness and strain relaxation, considered an expression for the areal energy density E_c associated with the homogenous nucleation in the slip system of half-loops at the surface. The model for the generation of the dislocation was found to describe the experimental data better than previously suggested models.

The equilibrium models of van der Merwe and Matthews and Blakeslee assumed that misfit segments are formed by movement of preexisting threading dislocations. In carefully grown semiconductor crystals on low-defect substrates, the number of available threading dislocations might not be enough. In that case, new dislocations must nucleate before misfit segments can be formed. The effects of this process on the critical thickness of $\text{Ge}_x\text{Si}_{1-x}/\text{Si}$ (001) system was calculated by People and Bean (1985). Their approach was similar to that of van der Merwe: as mentioned above they equated the strain areal energy density to the interfacial energy density. A disadvantage of this method is that the release of strain energy during the nucleation and dissociation of dislocations are not taken into account. The model by Marée *et al.* describes the nucleation of misfit dislocation in a strained semiconductor layer by taking strain release and dissociation into account. Their strain/thickness relation is given by (Marée *et al.* 1987):

$$\varepsilon_0^2 h = \frac{b(1-\nu/2)}{160\sqrt{3}(1+\nu)} \left(-1 + \ln \frac{\alpha r_c}{b_0} \right), \quad \text{for tensile stress} \quad (4.11a)$$

$$\varepsilon_0^2 h = \frac{b(1-\nu/2)}{80\sqrt{3}(1+\nu)} \left(-\frac{1}{2} + \ln \frac{\alpha r_c}{b_0} \right), \quad \text{for compressive stress} \quad (4.11b)$$

where α is the core parameter, r_c is the critical radius of the nucleating loop and the Burgers vector b_0 is related to a perfect dislocation.

For small h , an epitaxial layer is pseudomorphic ($\varepsilon = f$). Above the critical thickness $h = h_c$, $\varepsilon_0 < f$ and part of the mismatch-induced strain will be relaxed.

Dodson and Tsao

The first approach in the study of the kinetics of strain relaxation in semiconductors was by Dodson and Tsao (1987). Their model is based on the experimental observation of strain relaxation in metastable strained-layer structures. In this model the rates of both nucleation and propagation were considered, in order to estimate an overall strain relaxation rate as a function of time and temperature. The model predicts that there are several stages involved in the strain relaxation as the thickness increases during the growth of the epilayer. This is illustrated in figure 4.3.

Step (i): there is no relaxation until the critical thickness is reached.

Step (ii): beyond the critical thickness the strain relaxation is sluggish because at this stage the excess stress is relatively low.

Step (iii): with a further increase in the layer thickness, the residual strain decreases and there is an increase in dislocation propagation velocities.

Step (iv): with the thick layer, the rate at which dislocations are formed slows down and the strain asymptotically approaches zero.

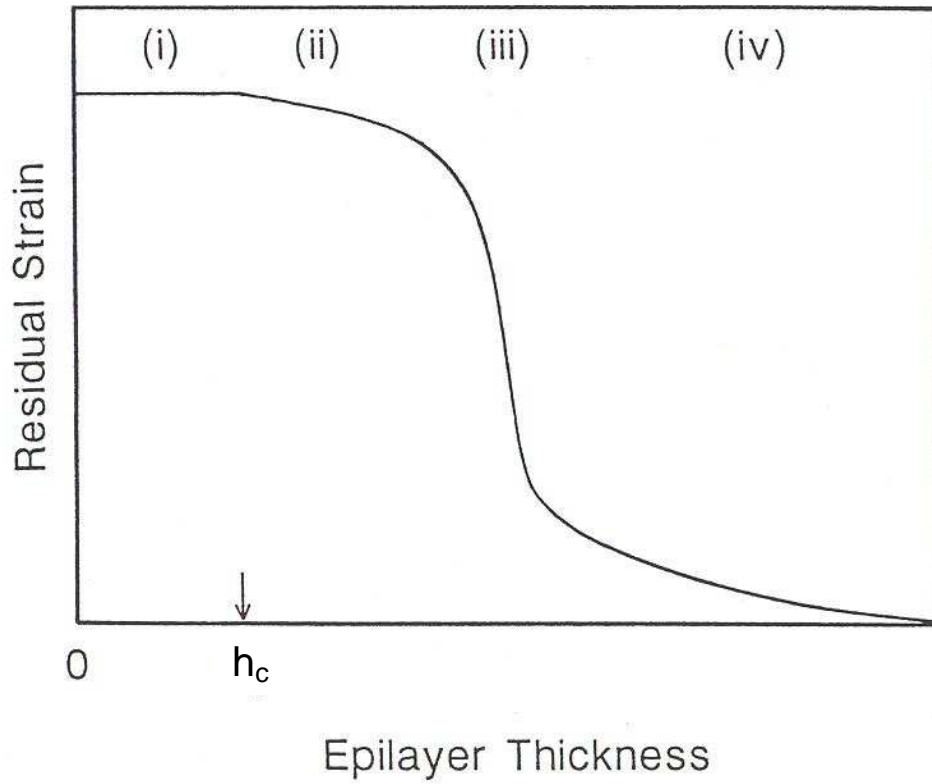


Figure 4.3: Schematic illustration of different steps of the strain relation in the Dodson/Tsao model (after Hull and Bean, 1992).

CHAPTER 5

EXPERIMENTAL SETUP AND SAMPLE GROWTH

5.1 Introduction

This study involves the characterization of $\text{In}_x\text{Ga}_{1-x}\text{As}$, $\text{Al}_x\text{Ga}_{1-x}\text{As}$, $\text{InAs}_{1-x}\text{Sb}_x$ and $\text{In}_x\text{Ga}_{1-x}\text{Sb}$ ternary systems. All the epitaxial layers characterized in this study were grown by metal organic chemical vapour deposition (MOCVD) at the Nelson Mandela Metropolitan University (NMMU). The compositional effect and the variation of strain with layer thickness have been investigated using Raman and X-ray diffraction techniques.

In this chapter, the basic components of the Raman system will be discussed in detail. A short discussion on the X-ray diffraction technique will also be presented. Finally, details of the sample growth will be briefly discussed.

5.2 Raman experimental setup

Figure 5.1 shows a schematic diagram of components of the Raman spectroscopy system built at the NMMU Physics Department. It consists of the following parts: exciting laser, reflecting mirror to direct the laser beam to the sample mounted on the sample holder, optical system for illuminating the sample and collecting the scattered radiation, the spectrometer and the CCD detector connected to a computer for the collection of the Raman spectra. There are two filters used in this system, namely a line filter and a supernotch filter.

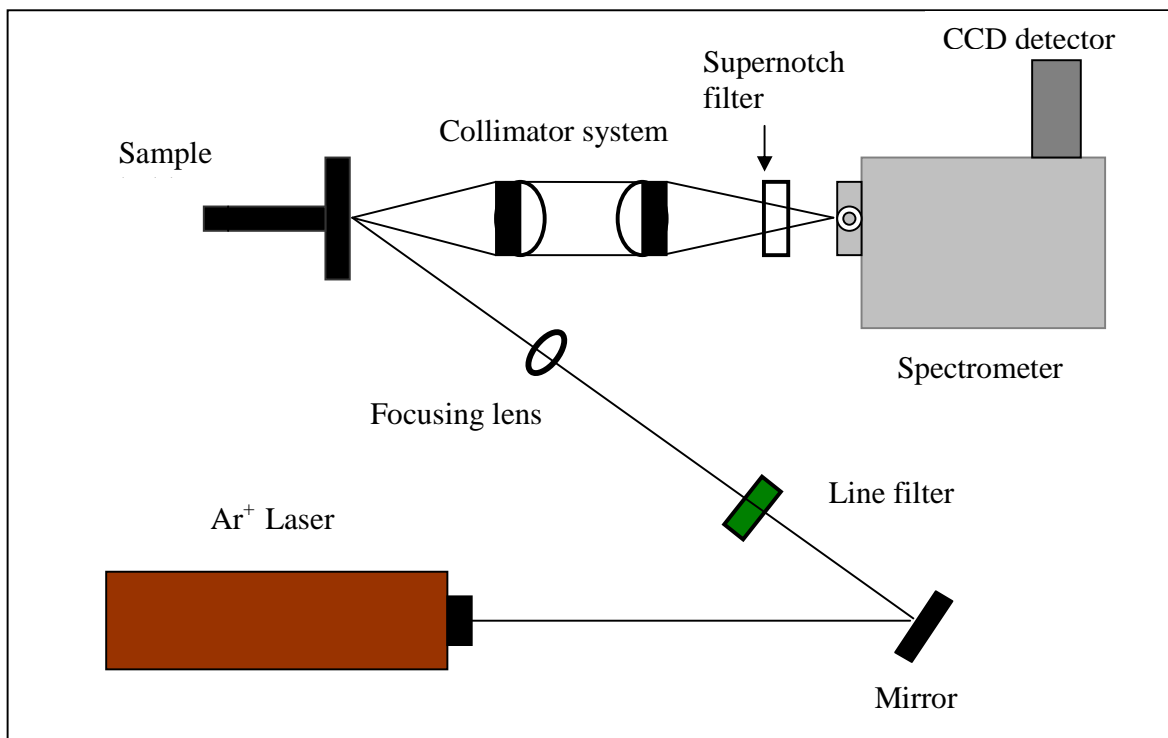


Figure 5.1: Schematic diagram of the Raman spectroscopy set-up. The angle between incident beam and collection direction was approximately 45° .

5.2.1 Excitation source

The Rayleigh line intensity is $10^3 - 10^4$ times that of the Raman bands i.e. Stokes and anti-Stokes bands (Baranska *et al.*, (1987), p.14), as discussed in chapter 2. Therefore, Raman spectroscopy requires a powerful monochromatic excitation signal, which provides sufficient intensity to produce a readily detectable Raman signal (Baranska *et al.*, (1987), p.14). The laser used in this study is an argon-ion (Ar^+) laser. The Ar^+ lasers have up to 10 lines in the spectral range from green to ultraviolet, the strongest being at 514.5 nm, 488 nm and 457 nm (Bauer and Richter, 1996). For our room temperature measurements, the 514.5 nm line was used and the output power of the laser was kept at 200 mW.

A spectral filter is used to eliminate non-lasing emission lines from the radiation source. In most cases a line filter is used to suppress these emissions.

5.2.2 Raman spectrometer

One of the problems in Raman spectroscopy is the high level of elastic scattering. The situation can be dealt with by using a spectrometer which gives a high contrast (Bauer and Richter, 1996). Hence, a double or a triple grating spectrometer is often used. This system may reduce the level of Rayleigh scattering by 10 or more orders of magnitude. However, using a double or triple grating spectrometer decreases the throughput of the optical system. High efficiency holographic notch filters that reject Rayleigh light may therefore be used to significantly increase the luminosity of the inelastically scattered light (Bauer and Richter, 1996). This is the approach followed in the present experimental set-up.

The scattered radiation from the sample is collected by the collimator system and directed to the spectrometer (see figure 5.1 for details). The elastically scattered light is then filtered from the scattered radiation by the holographic supernotch filter (with spectral bandwidth of $\leq 350 \text{ cm}^{-1}$). The beam of Raman light then enters the spectrometer. Figure 5.2 shows a schematic diagram of the spectrometer used in this study (with spectral resolution of 1 cm^{-1}). It has a 0.3 m focal length, adjustable entrance slit, a mirror at the entrance slit that directs the light onto a polished aspheric mirror, which collimates the incident light and reflects it onto a dispersive 1200 lines/mm grating mounted on a triple grating turret. The dispersed light is then collected by a second mirror and projected as a continuous band of wavelengths onto a CCD at the focal plane. The typical slit width of the spectrometer for our measurements was $80 \text{ }\mu\text{m}$.

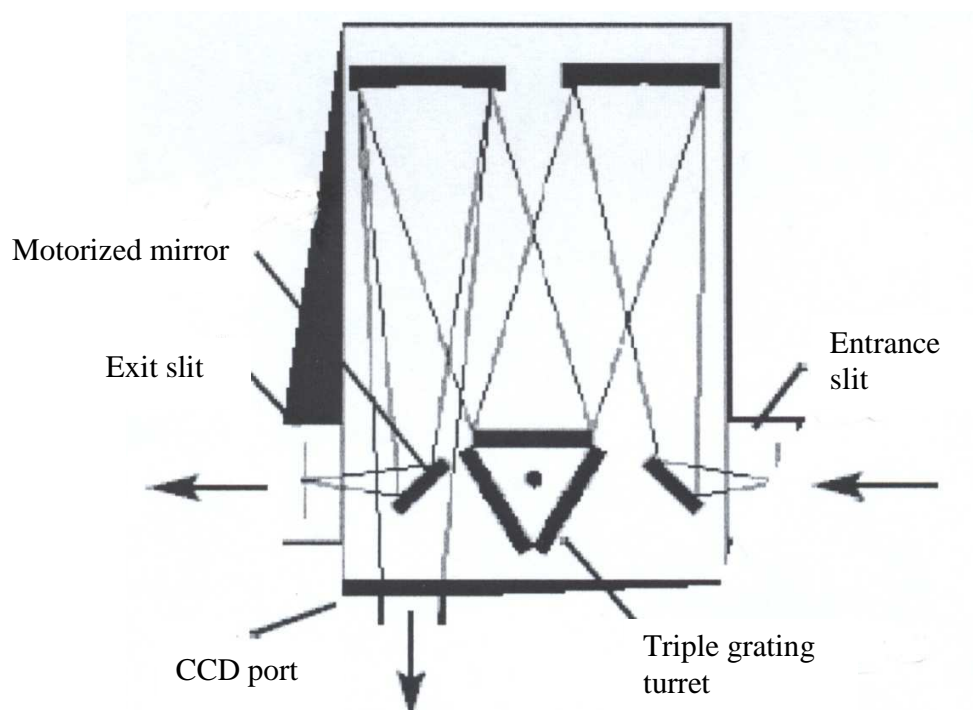


Figure 5.2: Schematic diagram of Acton SP-308 spectrometer used in a Raman spectroscopy system (Acton manual).

5.2.3 Detector

The detector used in the Raman system is a thermoelectrically cooled, DV 420 back-illuminated charge coupled device (CCD), from Andor Technology. Figure 5.3 illustrates a CCD, which consists of an array of pixels on a silicon integrated circuit. This array is usually referred to as the image area. The pixels are often described as being arranged in rows and columns. The CCD-chip in this study comprises 256 rows and 1024 columns.

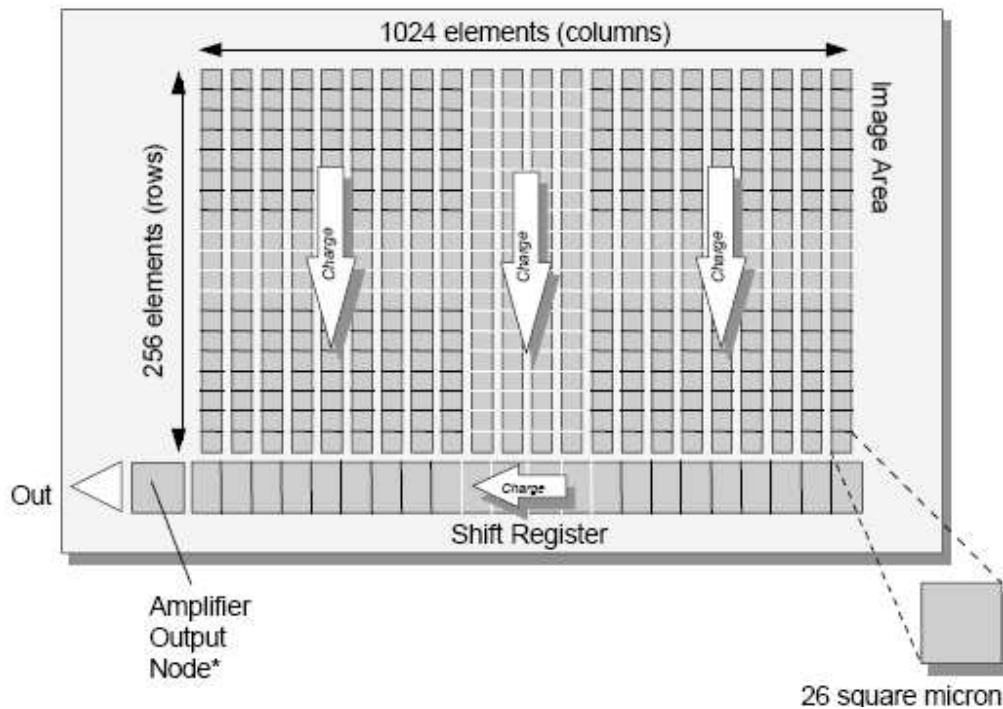


Figure 5.3: Schematic diagram of a CCD-chip (Andor CCD manual).

The adjustment of the spectrometer's slit has a direct effect on the spectral resolution of the Raman spectrometer, as the image which is focused on the CCD is proportional to the slit width. As the slit width decreases, the size of the focused image on the CCD detector decreases. Hence, the ratio of the linewidth of the Raman band to the corresponding amount of pixels exposed after separation into individual wavelengths by the grating decreases, improving spectral resolution.

When scattered light falls on the CCD's sensitive image area, photoelectrons are generated. The dispersed beam is spread vertically across horizontal lines of pixels, which are binned or summed up. Raman counts are based on analog-to-digital conversion, in which photoelectrons are converted to digital signal. The digital signal is interpreted using the computer software.

Before acquiring the data, the CCD detector was cooled down. It is cooled by a Peltier cooler. Figure 5.3 shows a photograph of the Andor CCD camera mounted on the monochromator and connected to the computer and cooling system. The temperature of the detector was kept at $-55\text{ }^{\circ}\text{C}$ in all the measurements in order to reduce the dark current.

Once the detector was cooled, the Raman system was calibrated in order to ensure that the collected data could be trusted. This was accomplished by making sure that there was proper optical alignment, and then collecting data from a standard reference sample. In this study, silicon was used as the reference because it has been extensively studied using Raman spectroscopy and its properties are well known. Once the correct vibrational wavenumber of a silicon sample had been allocated, its peak height was optimised by adjusting the optical systems before actual measurements of the samples commenced.



Figure 5.4: Photograph of Nelson Mandela Metropolitan University Raman setup.

5.3 X-ray Diffraction (XRD)

X-ray diffraction (XRD) is a powerful non-destructive tool for the structural characterisation of materials. It provides information such as orientation, lattice constant, composition, built-in strain and strain relaxation. In XRD measurements, X-ray radiation (e.g. from CuK α source) is focused on the sample at a certain angle with respect to the sample surface. The incident beam is scattered by the atoms in the sample that are ordered in crystal planes. Constructive interference occurs when the photon path difference between two planes is an integer number of the wavelengths. This condition is described by Bragg's law:

$$2 d_{hkl} \sin \theta = n \lambda \quad (5.1)$$

where d_{hkl} is the distance between the planes, θ is the angle between the incident X-ray beam and the plane, λ is the wavelength of the beam ($\lambda = 1.5405 \text{ \AA}$ for CuK α) and n is an integer. Figure 5.3 illustrates the geometry of an XRD setup. The system used in the present work is a Philips P W 1840 powder diffractometer.

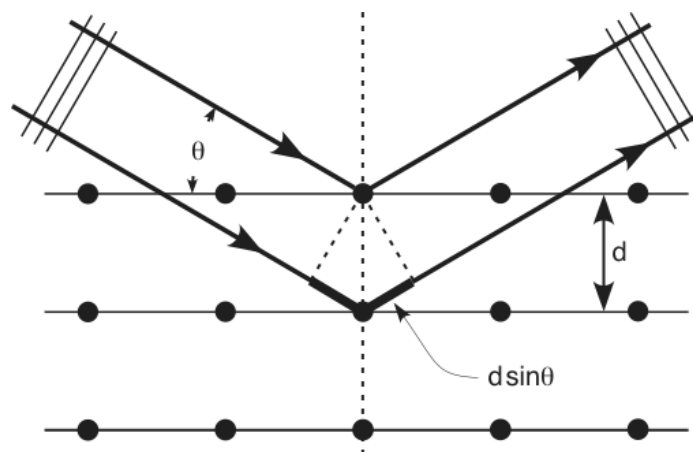


Figure 5.5: Schematic diagram of the diffraction geometry.⁴

⁴ http://en.wikipedia.org/wiki/File:Bragg_diffraction.png

To measure the lattice constant of a layer, the (400) reflection was used to obtain the lattice constant normal to the layer surface. The inter-planar spacing for a cubic structure is given by the following expression:

$$d_{hkl} = \frac{a}{\sqrt{h^2 + k^2 + l^2}} \quad (5.2)$$

where a is the out-of-plane lattice constant and hkl are the Miller indices of the diffraction plane (Culitty, 1967). From the calculated lattice constant, the composition could then be determined using Vegard's law.

5.4 Growth of III-V thin films

All the films were deposited in an Epitor 04 MOCVD reactor. Palladium-diffused H_2 was used as a carrier gas. The thicknesses of epilayers ($> 2 \mu m$) were measured using a Nomarski differential interference contrast microscope. The thicknesses of strained/partially strained films (less than a few hundred nanometres) were extrapolated based on growth rate of thick layers.

5.4.1 $In_xGa_{1-x}As$

Trimethylgallium (TMG) and trimethylindium (TMI) were used as organometallic sources for gallium and indium, respectively. Arsine (AsH_3) diluted at 10 % in H_2 was used as group-V source. Palladium-diffused H_2 was the carrier gas. Table 5.1 lists the growth conditions used for the layers.

Semi-insulating (SI) GaAs substrates oriented 2° off (100) towards the nearest $\langle 110 \rangle$ were used. X-ray diffraction was used to determine the indium content in the epilayers.

Table 5.1: Growth condition for $\text{In}_x\text{Ga}_{1-x}\text{As}$ thin films.

X	≤ 0.3
n_{TMI}	$\leq 5 \mu\text{mol}/\text{min}$
n_{TMG}	$7.6 \mu\text{mol}/\text{min}$
n_{AsH_3}	$4.0 \times 10^{-4} \text{ mol}/\text{min} - 4.8 \times 10^{-4} \text{ mol}/\text{min}$
T_g	$610 \text{ }^\circ\text{C} - 690 \text{ }^\circ\text{C}$
T_{TMI}	$27 \text{ }^\circ\text{C}$
T_{TMG}	$-9 \text{ }^\circ\text{C}$
V/III	$5 - 280$

5.4.2 $\text{Al}_x\text{Ga}_{1-x}\text{As}$

For $\text{Al}_x\text{Ga}_{1-x}\text{As}$ growth, trimethylgallium (TMG) and trimethylaluminium (TMA) were used as sources for gallium and aluminium, respectively. A 10 % mixture of AsH_3 in ultra-pure H_2 was used as the group-V source. Table 5.2 lists the growth conditions used for the layers.

The Al mole fraction was determined by photoluminescence (PL) using the relation (Stringfellow and Linnebach, 1980):

$$x = 0.8032 (h\nu_{\text{BE}} - 1.512) \quad (5.3)$$

where $h\nu_{\text{BE}}$ is the bound exciton peak energy measured at 12 K.

The $\text{Al}_x\text{Ga}_{1-x}\text{As}$ samples were grown on a 2° off (100) semi-insulating (SI) GaAs substrate.

Table 5.2: Growth condition for $\text{Al}_x\text{Ga}_{1-x}\text{As}$ thin films.

X	≤ 0.36
T_g	745 °C
T_{TMA}	18.5 °C
T_{TMG}	-9 °C
V/ III	90

5.4.3 $\text{InAs}_{1-x}\text{Sb}_x$ and $\text{In}_x\text{Ga}_{1-x}\text{Sb}$

Trimethylgallium (TMG), trimethylantimony (TMS) and trimethylindium (TMI) were the organometallic precursors used. Tables 5.3 and 5.4 list the growth conditions used for the layers.

The epitaxial layers were grown on GaSb and GaAs substrates oriented at 2° off (100) towards $\langle 110 \rangle$. X-ray diffraction was performed to determine the alloy composition of the epilayers.

Table 5.3: Growth condition for $\text{InAs}_{1-x}\text{Sb}_x$ thin films.

X	≤ 0.17
T_g	500 °C
T_{TMI}	25 °C
T_{TMS}	0 °C
T_{TBA}	5.5 °C
V/ III	5 – 30

Table 5.4: Growth condition for $\text{In}_x\text{Ga}_{1-x}\text{Sb}$ thin films.

X	≤ 0.24
T_g	$550\text{ }^\circ\text{C} - 600\text{ }^\circ\text{C}$
T_{TMI}	$25\text{ }^\circ\text{C}$
T_{TMG}	$-9\text{ }^\circ\text{C}$
T_{TMS}	$0\text{ }^\circ\text{C}$
V/ III	$0.3 - 1.25$

Chapter 6

RESULTS AND DISCUSSION

6.1 Introduction

Stress and strain in III-V semiconductor alloys have been extensively studied in recent years, because they offer interesting design possibilities for high speed electronic and optoelectronic devices (Groenen *et al.* 1997). Normally, the internal strain in a layer arises during the growth of a layer on a lattice mismatched substrate. As mentioned previously in section 4.1.1, the growth of pseudomorphic layers is limited by the critical thickness above which structural defects are generated. These defects degrade the crystalline quality. Many physical properties of these types of heterostructures depend on the strain. In this chapter the results of strain variation in terms of composition and layer thickness will be presented.

6.2 InGaAs

6.2.1 Incorporation of indium into the GaAs lattice

A series of six $\text{In}_x\text{Ga}_{1-x}\text{As}$ samples with composition ranging from $x = 0$ to $x = 0.25$ were grown on GaAs 2° off (100) to observe the effect of the incorporation of indium into the GaAs lattice. These samples have nominally the same thickness ($\sim 4\mu\text{m}$). Figure 6.1 shows the X-ray diffraction (XRD) spectra for these layers. The spectra clearly show strong 400 peaks, with the $K\alpha_1$ and $K\alpha_2$ peaks well defined. There is a shift of the $K\alpha_1$ and $K\alpha_2$ peaks of $\text{In}_x\text{Ga}_{1-x}\text{As}$ with an increase in indium content. The angular separation between the substrate and epilayer peaks indicates the increasing lattice mismatch, which is caused by an increasing indium content of the $\text{In}_x\text{Ga}_{1-x}\text{As}$ layers.

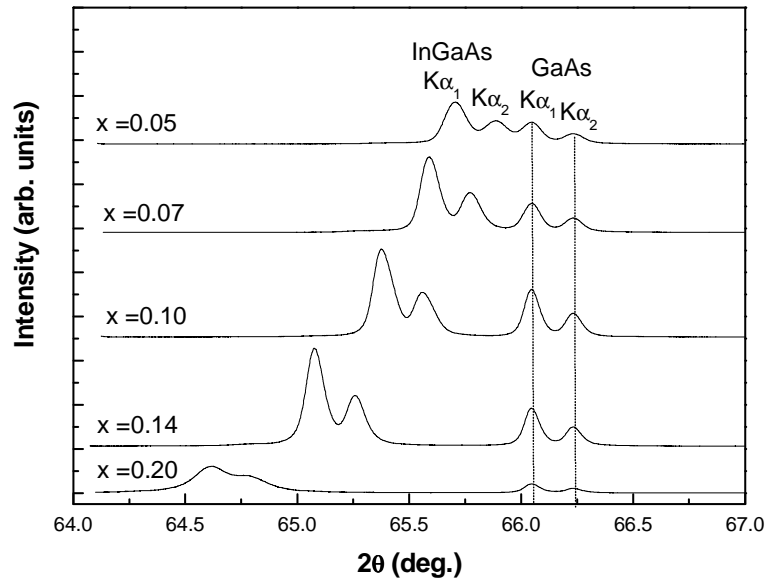


Figure 6.1: X-ray diffraction spectra for the (400) reflection from $\text{In}_x\text{Ga}_{1-x}\text{As}$ layers of various compositions grown on GaAs substrates.

6.2.2 Compositional dependence of optical phonon frequencies

The local vibrational properties of the host lattice are modified by the presence of a substitutional atom (Taylor, 1966). If it is light enough, it causes a mode to split off the vibrational continuum of the pure crystal to create a local mode. It is termed a local mode because the amplitude of the vibrations of this mode is localized around the defect. There is a change in force constants during the substitution and this affects lattice vibrational modes. The more defects that are added, the more they interact and additional modes are produced (Taylor, 1966). The effect of compositional variation on the optical phonon frequencies in $\text{In}_x\text{Ga}_{1-x}\text{As}$, grown on 2° off (100) GaAs substrate, has been studied by Raman spectroscopy in this work. The series of six relaxed $\text{In}_x\text{Ga}_{1-x}\text{As}$ samples is the same as that discussed in section 6.2.1. The thickness of the layers was kept constant in order to study the effect of changes in composition only. The effects of thickness on the phonon frequencies will be presented in section 6.4.

Figure 6.2 shows the influence of composition on the optical phonon frequencies for this series, as well as a spectrum of an $\text{In}_{0.53}\text{Ga}_{0.47}\text{As}$ layer nominally lattice matched to InP (100). It is evident that the spectra are dominated by GaAs-like LO modes at higher wavenumbers and weak GaAs TO modes. Above an indium mole fraction of 0.10 the InAs-like LO phonon signal is also weakly observed.

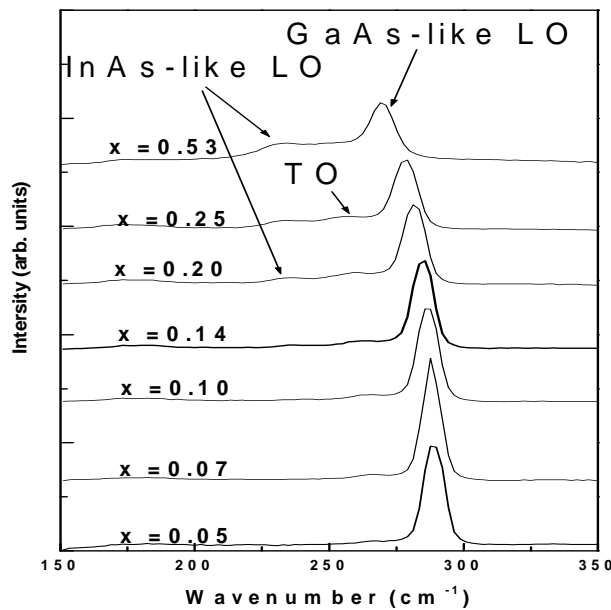


Figure 6.2: Room temperature Raman spectra of $\text{In}_x\text{Ga}_{1-x}\text{As}/\text{GaAs}$. Also included is the spectrum of $\text{In}_{0.53}\text{Ga}_{0.47}\text{As}/\text{InP}$ (100).

The zone-centre optical phonons in alloys may exhibit a variety of behaviours depending on the vibrational characteristics of the binary end members, which are GaAs and InAs in the case of InGaAs (Genzel *et al.* 1974), as discussed in section 3.3.3. The LO and TO phonon vibrational frequencies in GaAs are 292 cm^{-1} and 269 cm^{-1} , respectively (Carles *et al.* 1980). For InAs, the LO phonon frequency is 238.8 cm^{-1} and the TO frequency is

217.3cm^{-1} (Vorlicek *et al.* 2002). $\text{In}_x\text{Ga}_{1-x}\text{As}$ is expected to show a “mixed-mode” behaviour in which the GaAs-like LO and TO pair is observed over a certain composition range and the InAs-like LO and TO pair is observed over the remaining composition range (Brodsky and Lucovsky, 1968). As mentioned in previous paragraph, only the LO vibrational mode is strongly observed from (100) orientated layers for the pseudo-backscattering configuration used here.

The introduction of indium into the GaAs lattice is expected to cause a shift in the GaAs phonon modes towards lower vibrational frequencies. Early Raman spectroscopy work by Emura *et al.* (1988) showed that $\text{In}_x\text{Ga}_{1-x}\text{As}$ alloys exhibit a mixed mode behaviour over a wide range of composition, meaning that the spectra show one mode for a certain range of composition and two modes for the remaining range of composition. Our results confirm that $\text{In}_x\text{Ga}_{1-x}\text{As}$ displays mixed mode behaviour: for $\text{In}_x\text{Ga}_{1-x}\text{As}$ with $x < 0.14$, the spectra consist of one mode only. For $x \geq 0.14$ two bands, i.e. GaAs-like and InAs-like modes, are observed. For higher compositions, the GaAs-like LO modes are expected to gradually converge to that of InAs.

Figure 6.3 shows the Raman spectra of $\text{In}_x\text{Ga}_{1-x}\text{As}$ nominally lattice matched to InP. A dominant GaAs-like LO phonon mode at 270cm^{-1} and InAs-like LO mode at 233cm^{-1} are observed. An additional peak at 244cm^{-1} is also detected. For $\text{In}_x\text{Ga}_{1-x}\text{As}$ grown on InP ($x = 0.53$), Pickering *et al.* (1981), using infrared spectroscopy, found GaAs-like LO and TO frequencies of 272cm^{-1} and 254cm^{-1} and InAs-like LO and TO phonon frequencies at 230cm^{-1} and 224cm^{-1} , respectively. The LO modes frequencies have been confirmed by Raman backscattering investigations by Emura *et al.* (1988), (Kakimoto and Katoda, 1982) and Pinczuk *et al.* (1978). Pearsall *et al.* (1983) identified the GaAs-like LO mode at 270cm^{-1} and InAs-like TO mode at 226cm^{-1} using Raman spectroscopy and two modes of intermediate frequencies at 254cm^{-1} and 244cm^{-1} . The peak at 254cm^{-1} was not detected in this work. The peak at 244cm^{-1} is attributed to disorder-activated lattice vibrations which are thought to exist in this alloy (Kakimoto and Katoda, 1982).

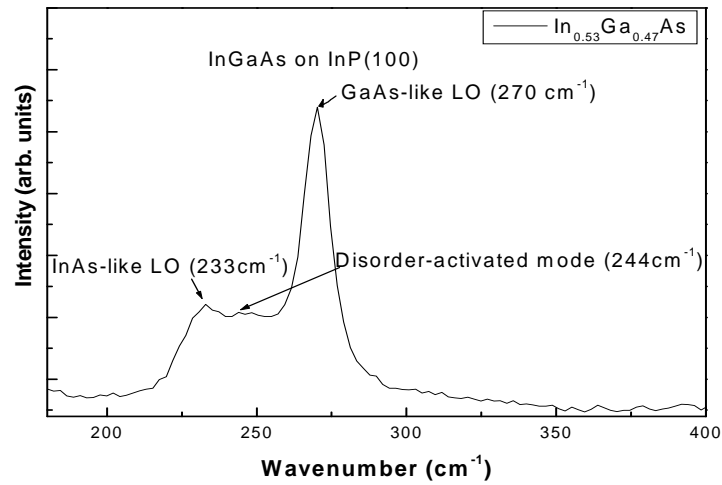


Figure 6.3: Room temperature Raman spectra of $\text{In}_x\text{Ga}_{1-x}\text{As}$ grown on InP (100) with $x = 0.53$.

The measured peak positions for the entire series of layers are shown in figure 6.4 as a function of the indium mole fraction x . The figure also shows the compositional dependence of the four Raman-active vibrational modes in $\text{In}_x\text{Ga}_{1-x}\text{As}$ reported by various other groups. The solid lines are least-squares fits to all the data, using second order polynomial expressions.

As discussed above, the mode behaviour in figure 6.4 represents a third type of behaviour which is intermediate to that observed in the “one-” or “two-” mode system discussed in section 3.3.3.

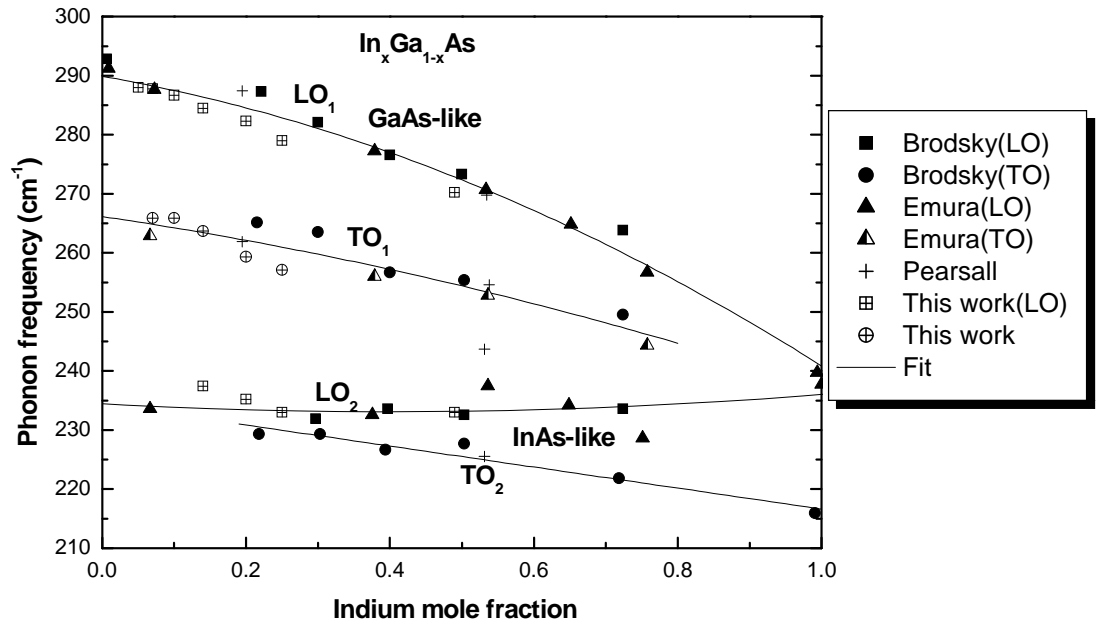


Figure 6.4: Compositional dependence of the phonon frequency in $\text{In}_x\text{Ga}_{1-x}\text{As}$.

The solid lines are least-squares polynomial fits to the data.

Since no InAs-like TO mode signals could be detected in this work, the solid line through the relevant data is a least-squares linear regression performed by Brodsky and Lucovsky (1968).

The GaAs-like LO frequency dependence on composition is adequately described by the expression:

$$\nu_{\text{GaAs(LO)}} (\text{cm}^{-1}) = 289.9 - 21.0x - 28.0x^2 \quad (6.1)$$

The compositional variation of the GaAs-like TO phonon frequency is given by the expression (Brodsky and Lucovsky, 1968):

$$\nu_{\text{GaAs(TO)}} (\text{cm}^{-1}) = 266.2 - 18.0x + 11.1x^2 \quad (6.2)$$

The InAs-like LO compositional variation is given by:

$$\nu_{\text{InAs(LO)}}(\text{cm}^{-1}) = 234.4 - 6.5x + 8.1x^2 \quad (6.3)$$

Finally, the InAs-like TO phonon frequency, can be described by linear relationship:

$$\nu_{\text{InAs(TO)}}(\text{cm}^{-1}) = 234.4 - 17.8x \quad (6.4)$$

Emura *et al.* (1988) also showed that the compositional variations in the optical phonon frequencies of $\text{In}_x\text{Ga}_{1-x}\text{As}$ are generally not linear. For other III-V ternary alloys such as $\text{Al}_x\text{Ga}_{1-x}\text{As}$ (discussed in section 6.5), for example, both the LO mode frequencies decrease with increasing mole fraction x and the optical bands related to each binary constituent remain separated. Clearly figure 6.4 shows this is not the case in $\text{In}_x\text{Ga}_{1-x}\text{As}$: the InAs-like LO mode remains almost constant in frequency, while the GaAs-like LO mode frequency decreases strongly with increasing indium mole fraction. To explain this kind of behaviour, Raman studies on $\text{In}_{0.53}\text{Ga}_{0.47}\text{As}/\text{InP}$ (100) by Groenen *et al.* (1997) considered an effect: disorder (chemically and structurally) lowers both the GaAs-like and InAs-like mode frequencies.

For the InAs-like modes the above effects cause opposite frequency shifts, leading to an almost independence of frequency on composition. For the GaAs-like mode the effects combine to cause a large shift. In addition, the GaAs-like and InAs-like polar LO modes couple together due to the small gap between the optical modes of bulk InAs and GaAs. So their repelling accounts for the nonlinear frequency variation with composition (Groenen *et al.* 1997).

6.2.3 Variation of strain with layer thickness

The $\text{In}_x\text{Ga}_{1-x}\text{As}/\text{GaAs}$ alloy system is a lattice-mismatched system. Unlike the lattice matched $\text{Al}_x\text{Ga}_{1-x}\text{As}/\text{GaAs}$ system, $\text{In}_x\text{Ga}_{1-x}\text{As}$ and GaAs have different lattice parameters. As mentioned in section 4.1.1, when grown on GaAs substrate, the alloy is subjected to biaxial compression so that its in-plane lattice constant is equal to that of bulk GaAs. The extent to which lattice mismatch can be accommodated by strain of the InGaAs layer depends on the thickness of the layer. As long as the layer thickness is less than a given critical thickness (which depends on the composition), the layer can be grown without the introduction of misfit dislocation. The experimental determination of critical thickness for $\text{In}_x\text{Ga}_{1-x}\text{As}/\text{GaAs}$ depends on the technique used for measuring this thickness. In essence, the critical thickness determined experimentally depends on the sensitivity of the technique to either detecting misfit dislocations directly (e.g. PL spectroscopy and Hall measurements) or to detecting lattice relaxation (e.g. X-ray diffraction).

In this section, Raman spectroscopy is used to provide quantitative measurements of the amount of strain present in each sample, which allows one to get an indication of the critical thicknesses. It is assumed that the strain is uniform in each film, irrespective of the thickness. Raman measurements were performed on $\text{In}_x\text{Ga}_{1-x}\text{As}/\text{GaAs}$ layers with different thicknesses and indium mole fractions $x = 0.07, 0.12$ and 0.14 , respectively. For a given composition, the layer thicknesses were such that some layers should be fully strained, some partially relaxed and some fully relaxed. The spectra obtained for the three series of samples are shown in figures 6.5, 6.6 and 6.7. Each spectrum is dominated by the GaAs-like LO phonon signal. The absence of the InAs-like LO mode for $x = 0.07$ and $x = 0.12$ is due to the low concentration of indium in these samples.

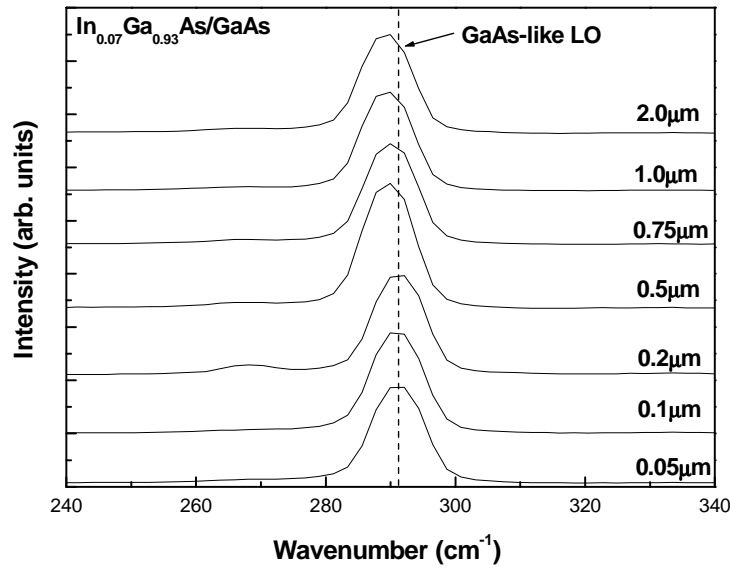


Figure 6.5: Raman spectra of $\text{In}_{0.07}\text{Ga}_{0.93}\text{As}/\text{GaAs}$ layers with thickness ranging from below to above the critical thickness.

From figure 6.5 it is clear that the optical phonons shift to slightly lower frequencies as the thickness of the epilayer changes. Although the total shift for $x = 0.07$ is only $\sim 2 \text{ cm}^{-1}$, which is of the order of the spectral resolution of the instrumentation (1 cm^{-1}), it is believed to be real; it was consistently observed for several sets of measurements on these samples. A broadening of the LO peak is expected with an increase in the thickness of the layer due to the introduction of defects (Groenen *et al.* 1997). This broadening is not apparent in this work. According to Groenen *et al.* for small compressive misfits ($x < 0.8$), the FWHM remains close to its intrinsic value.

Figure 6.6 shows the spectra for $x = 0.12$. There is a more significant peak shift as the thickness changes in this case, as compared to the layers with $x = 0.07$. The total Raman frequency shift is $\sim 4 \text{ cm}^{-1}$ for thicknesses ranging from $0.01 \mu\text{m}$ to $1 \mu\text{m}$. In figure 6.7, the total shift measured for $x = 0.14$ is $\sim 5 \text{ cm}^{-1}$.

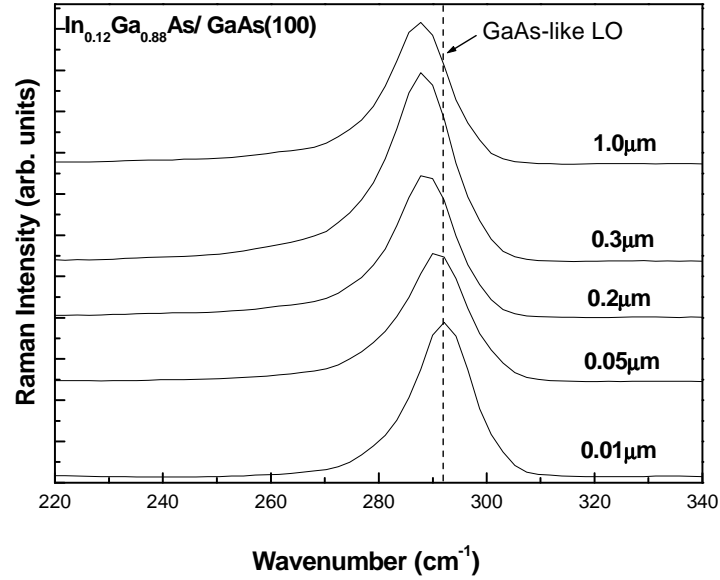


Figure 6.6: Raman spectra of $\text{In}_{0.12}\text{Ga}_{0.88}\text{As}/\text{GaAs}$ layers with thicknesses ranging from below to above critical thickness.

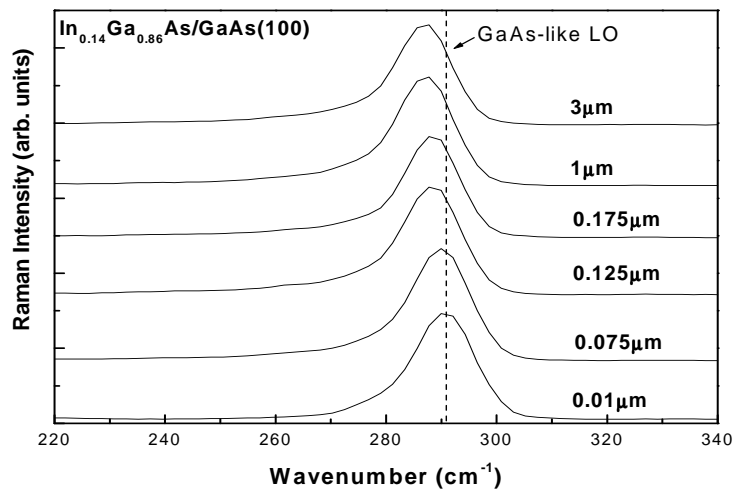


Figure 6.7: Raman spectra of $\text{In}_{0.14}\text{Ga}_{0.86}\text{As}/\text{GaAs}$ layers with thicknesses ranging from below to above critical thickness.

$\text{In}_x\text{Ga}_{1-x}\text{As}$ is subjected to compression, since its lattice constant is larger than that of the GaAs substrate. For $x = 0.07, 0.12$ and 0.14 , perpendicular x-ray strain was measured, and the results are listed in table 6.1. The measured LO phonon frequencies are also listed in the table. To calculate the phonon frequency due to strain in the layers, the elastic or actual strain must be determined. The relationship between the elastic and x-ray strain is given by (Bauer and Richter, 1996):

$$\varepsilon_{xx} = (\varepsilon_{\perp} + 1) \frac{a_s}{a_0^L} - 1 \quad (6.5)$$

where ε_{xx} and ε_{\perp} are elastic and x-ray strains, respectively and a_s and a_0^L are the lattice constants of the substrate and unstrained (freestanding) $\text{In}_x\text{Ga}_{1-x}\text{As}$. The elastic strains ε_{xx} (in-plane) and ε_{zz} (out-of-plane) are related by the equation (Bauer and Richter, 1996):

$$\varepsilon_{zz} = -2 \frac{C_{12}}{C_{11}} \varepsilon_{xx} \quad (6.6)$$

where C_{12} and C_{11} are the elastic stiffness constants of $\text{In}_x\text{Ga}_{1-x}\text{As}$.

The shifts due to stress or strain, measured from (100) oriented layers can be expressed as (Burns *et al.* 1987):

$$\Delta\omega_{\text{LO}} = p\varepsilon_{zz} + q(\varepsilon_{xx} + \varepsilon_{yy}) \quad (6.7)$$

where $\varepsilon_{xx} = \varepsilon_{yy}$ for the in-plane components of elastic strain. The phonon deformation constants p and q describe the change in the spring constant due to the strain (Ganesan *et al.* 1970). The phonon deformation constants have been obtained by interpolation for various crystal orientations by Anastassakis *et al.* (1970), Shin *et al.* (2000), Cerdeira *et al.* (1972) and Sood *et al.* (1985).

Using the phonon deformation constants (from Shin *et al.* (2000)), and the strain values extracted from the X-ray strain (listed in Table 6.1), the phonon frequency shift ($\omega - \omega_0$)

was calculated. From this the bulk or unstrained phonon frequencies ω_0 were calculated. The bulk frequencies are plotted together with strained frequencies in figure 6.8. From table 6.1, it is noticed that physically, the largest negative in-plane elastic strain (ϵ_{xx}) occurs for the thinnest layers, which are pseudomorphic (i.e. full strained) and hence the largest perpendicular strain (ϵ_{zz}) are expected for these layers. This will be shown in section 6.5. Compressive strain shift will shift the phonon frequencies to higher energies, hence it is expected that the thinnest layer for each composition should exhibit the largest frequency shift. This is confirmed by the results in table 6.1.

Table 6.1: The first two columns list the composition and, thicknesses of the layers. The next two columns are: the calculated X-ray strain and the measured LO mode frequency in the layer. The last three columns are calculated quantities: the elastic strain parallel (ϵ_{xx}), perpendicular (ϵ_{zz}) to the plane and the frequency shift.

Composition	Thickness (μm)	X-ray strain ϵ_{\perp}	LO (cm^{-1})	ϵ_{xx}	ϵ_{zz}	$\Delta\omega_{\text{LO}}$
0.07	0.05	0.0123	291.2	-0.0067	0.0061	3.7
0.07	0.5	0.0053	289.9	-0.0028	0.0025	1.5
0.12	0.05	0.0152	291.5	-0.0078	0.0072	4.2
0.12	0.2	0.0113	289.1	-0.0058	0.0054	3.1
0.14	0.01	0.0156	291.1	-0.0081	0.0074	4.3
0.14	0.125	0.0138	288.9	-0.0071	0.0066	3.8

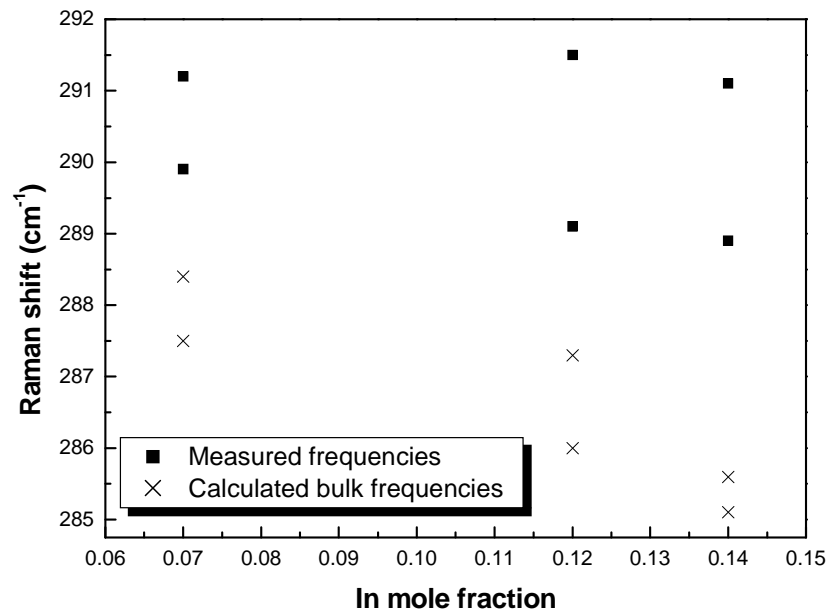


Figure 6.8: Solid squares are the measured phonon frequencies for unstrained/partially strained layers. For each strained layer, a corresponding bulk or unstrained frequency (cross) is calculated from the measured frequency and strain.

6.2.4 Critical layer thickness

In layers thinner than a critical layer thickness the mismatch is accommodated by elastic strain, while in thicker layers, lattice mismatch is accommodated by a combination of strain, dislocations and three dimensional growth (Hull and Bean, 1992). Although there has been considerable theoretical work on the prediction of the critical thickness (Fritz *et al.*, 1987), it is still difficult to predict it accurately. Figure 6.9 shows a comparison between two models commonly used to predict the critical layer thickness, for mismatched systems. The so-called energy balance model proposed by People and Bean (1985) predicts values that are much higher than those predicted by the mechanical equilibrium model of Matthews and Blakeslee (1974). These models have been summarized in section 4.1.2.

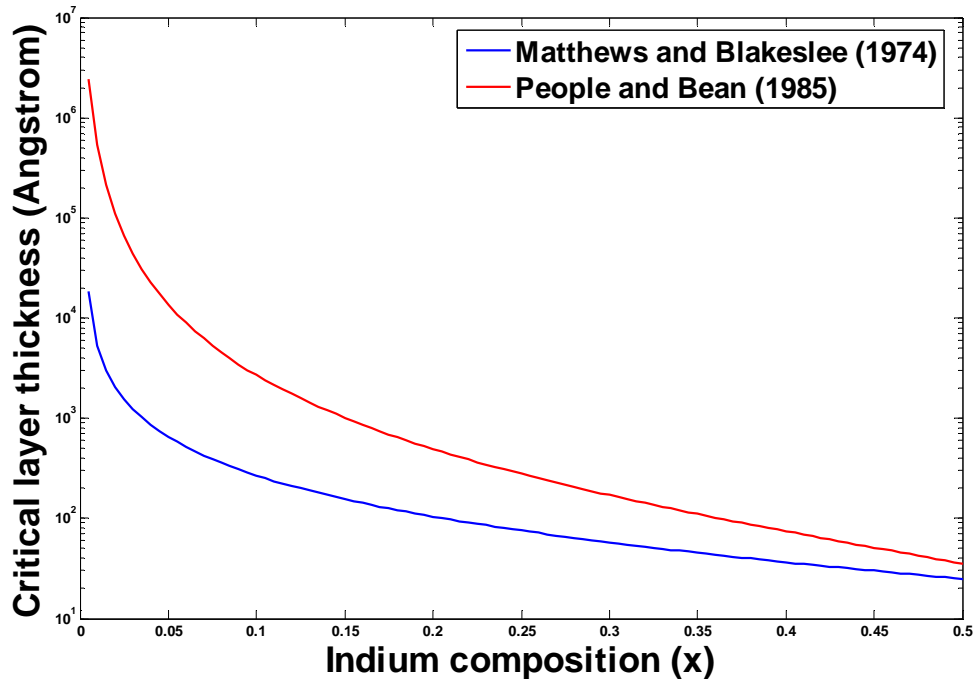


Figure 6.9: Comparison of the critical layer thickness as predicted by two theoretical models.

The critical layer thickness has been determined experimentally for arsenide, phosphide and Si-Ge single heterostructures using various techniques, such as transmission electron microscopy (TEM) (Reithmaier *et al.* 1989), X-ray diffraction (XRD) (Orders and Usher, 1987), and optical measurements (Grurley *et al.* 1988). The critical thicknesses measured were found to correspond either to the Matthews and Blakeslee model or the People and Bean models.

These inconsistencies in determining the exact value of the critical thickness probably arise from the sensitivity of the characterization technique employed for monitoring the onset of misfit dislocations. Fritz (1987) pointed out that the measured critical layer thickness will depend on the minimum detectable strain relaxation for the technique used. A technique such as Raman spectroscopy can detect the influence of low defect densities (Hull and Bean, 1992).

In this study, the critical thickness was determined using Raman spectroscopy. To do this, the Raman peak was observed for the series of layers mentioned in section 6.2.3. In the case of layers grown below the critical layer thickness, biaxial compressive strain shifts the phonons to higher wavenumbers, while for layers grown above the critical thickness, the peaks relax to their unstrained frequency positions. The thickness at which the Raman peak starts to shift to lower frequencies for each series is assumed here to be an indication of the onset of strain relief.

Figure 6.10 shows Raman spectra of $\text{In}_{0.14}\text{Ga}_{0.86}\text{As}$ layers with thickness ranging from below to above the critical thickness. As discussed above, the GaAs-like LO peak shifts to lower wavenumbers as the thickness increases. For this series of samples, the peak evidently starts to shift to lower energy for thicknesses greater than $0.075\ \mu\text{m}$. This is believed to be the thickness where the strain begins to relax and it is therefore a measure of the critical thickness for this composition.

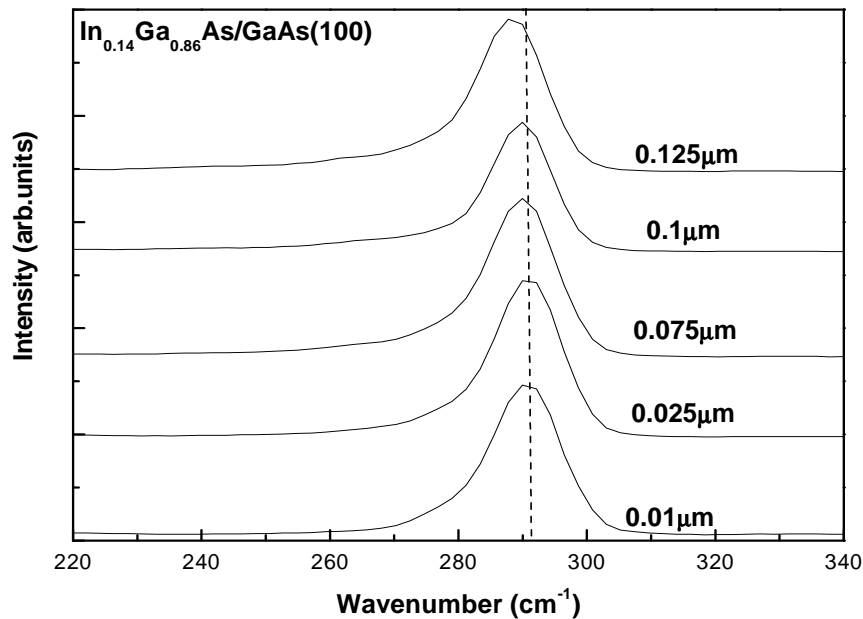


Figure 6.10: Raman spectra of $\text{In}_{0.14}\text{Ga}_{0.86}\text{As}$ layers with various thicknesses.

Figure 6.11 shows a plot of the LO phonon frequencies as a function of layer thickness for all three series investigated. The phonon frequency changes abruptly at some thickness, assumed to be the critical thickness, yielding values of around $0.2\ \mu\text{m}$, $0.075\ \mu\text{m}$ and $0.05\ \mu\text{m}$ for $x = 0.07$, 0.12 and 0.14 respectively. As expected, the critical layer thickness is a rapidly decreasing function of the composition, i.e. the thickness at which strain is relieved decreases strongly with increasing indium content.

For layers with thickness greater than the critical thickness, the strain is relieved fairly rapidly until it becomes negligible. According to Dodson and Tsao (1987), a large fraction of the original strain will be relaxed initially, after which strain relief becomes gradual (i.e. dislocation formation slows down). The structure will approach its equilibrium strain state ϵ_0 asymptotically. This latter part of the process is not consistent with the current measurements.

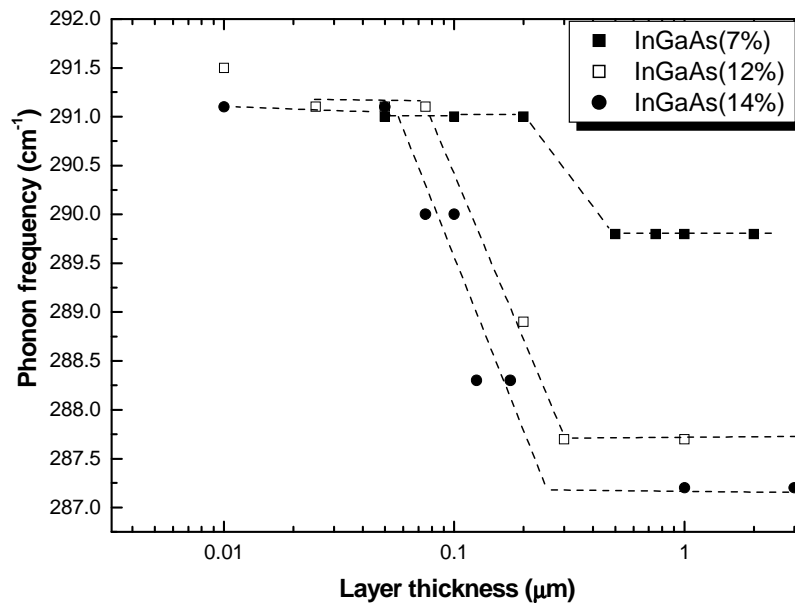


Figure 6.11: Plot of the phonon frequency as function of layer thickness for $\text{In}_x\text{Ga}_{1-x}\text{As}/\text{GaAs}$. The dotted lines are guides to the eye.

XRD can also be used to estimate the critical layer thickness. This technique is useful to characterize the crystalline properties of layers and can be used to monitor structural changes from the strained to the relaxed state, with increasing layer thickness. As previously mentioned in section 5.3, XRD measurements were carried out using the (400) reflection in order to obtain the lattice constant normal to the sample surface. The measured lattice constants for $x = 0.07, 0.14$ and 0.14 are listed in table 6.2. Lattice constants can be used to estimate the critical layer thickness. As the layer thickness increases for each composition, the perpendicular lattice constant decreases as expected. The thickness at which the lattice starts to relax is used as an indication of the critical layer thickness. When determining critical thickness using XRD, one needs to bear in mind that the technique is not very sensitive to low defect densities (Grurley *et al.* 1988).

In fact, XRD measures the critical layer thickness when a particular threshold dislocation density (or strain relaxation) has been exceeded. Hence, the critical layer thickness determined from this technique will be higher than the real thickness at the onset of strain relaxation (Sanchez *et al.* 1999). Figure 6.12 shows plots of the perpendicular lattice parameter as a function of the $\text{In}_x\text{Ga}_{1-x}\text{As}$ layer thickness. The results shown in the figure display similar behaviour with an increase in thickness for the three compositions. For the two compositions $x = 0.12$ and 0.14 the data points are indistinguishable from each other, due to the uncertainty (± 0.02) when calculating the indium content. From our results the critical thickness is estimated from the data points at which the lattice parameter begins to decrease.

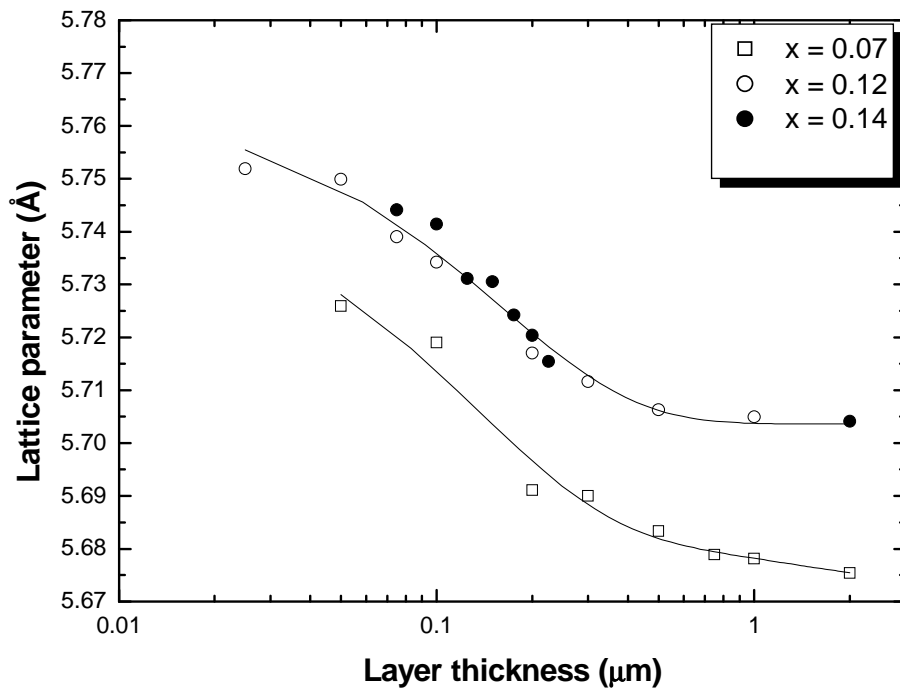


Figure 6.12: Plot of perpendicular lattice parameter determined from XRD as a function of $\text{In}_x\text{Ga}_{1-x}\text{As}$ layer thickness. The solid curves are guides to the eye.

Table 6.2: List of thicknesses from strained to unstrained, including calculated lattice constant and strain values for $x = 0.07, 0.12$ and 0.14 .

Composition	Thickness (μm)	a_{\perp} (\AA)	ϵ_{\perp}
x = 0.07	0.05	5.7259	0.0123
	0.1	5.7190	0.012
	0.2	5.6911	0.0067
	0.3	5.6900	0.0065
	0.5	5.6833	0.0053
	0.75	5.6789	0.0045
	1.0	5.6781	0.0044
	2.0	5.6754	0.00392
x = 0.12	0.025	5.7519	0.017
	0.05	5.7499	0.017
	0.075	5.7390	0.015
	0.1	5.7342	0.014
	0.2	5.7170	0.01
	0.3	5.7116	0.01
	0.5	5.7063	0.0094
	1.0	5.7049	0.0091
	3.0	5.6940	0.0072
x = 0.14	0.075	5.7441	0.016
	0.1	5.7414	0.016
	0.125	5.7311	0.014
	0.15	5.7305	0.014
	0.175	5.7242	0.013
	0.2	5.7204	0.012
	0.225	5.7154	0.011
	2.0	5.7041	0.009

In table 6.3, results from this work are compared with published data using various techniques to determine the critical layer thickness. It can be seen from the table that the experimental results obtained here follow the same pattern as the published ones, for similar indium content.

Table 6.3: Critical layer thickness estimated by Raman spectroscopy in this work compared with published data employing various techniques to estimate the critical thickness.

Technique	Composition(x)	Critical layer thickness (Å)
This work Raman	0.07	2000
	0.12	700
	0.14	500
This work XRD	0.07	1000 – 5000
	0.12 and 0.14	500 – 5000
Van Dyk (1994) PL (Shift)	0.06	1000 – 2000
	0.07	1000 – 2000
	0.13	500 – 1000
	0.14	500 – 750
Orders and Usher (1987) HR-XRD	0.07	2000
	0.14	1000
	0.25	300
Jeon <i>et al.</i> (1994) Raman PL (Shift)	0.16	1000
	0.20	400
Gal <i>et al.</i> (1987) MBE PL (Shift)	0.07	2000 - 4000
	0.14	500 - 1000
	0.25	200 – 500
Gal <i>et al.</i> (1987) MBE PL (FWHM)	0.07	2000 - 4000
	0.14	500 - 1000
	0.25	200 – 300
Morris <i>et al.</i> (1988) OMVPE PL (Intensity)	0.07	1200
	0.12	600
	0.19	200

In figure 6.13 the critical layer thickness values measured in this work using the Raman technique are compared to two theoretical models of critical thickness, namely the energy balance model by People and Bean (1985), and the mechanical equilibrium model by Matthews and Blakeslee (1974). The values predicted by these models differ by as much as two orders of magnitude, especially for low indium content (Orders and Usher, 1987). The solid squares in the figure represent our experimental data. There is good agreement between the mechanical equilibrium model and the experimental values, especially for the two experimental points at $x = 0.12$ and 0.14 . For the lowest indium content ($x = 0.7$) the experimental value is higher than the theoretical values predicted by the mechanical equilibrium model. The experimentally determined critical thickness values are often greater than the mechanical equilibrium model predictions (Hull and Bean, 1992), as can be seen from the figure. The discrepancies observed between the experimental data and theoretical predictions are thought to be due to the fact that the energy required for the propagation of dislocations is not typically available at growth temperatures (Jain *et al.* 1996). In high quality strained layers, the number of existing threading dislocations required for the generation of misfit dislocations is very low. When defects, which are the sources for dislocation generation, are not present, nucleation becomes homogeneous and needs large energy (Jain *et al.* 1996). This limits the generation of dislocations (Hull and Bean, 1992). The other factor that also contributes to these discrepancies is the sensitivity of the technique used. The experimental values of the critical thickness determined from techniques such as Raman, Photoluminescence (PL) and Hall measurements, which have good sensitivity, agree more closely with the theoretical predictions (Jain *et al.* 1996).

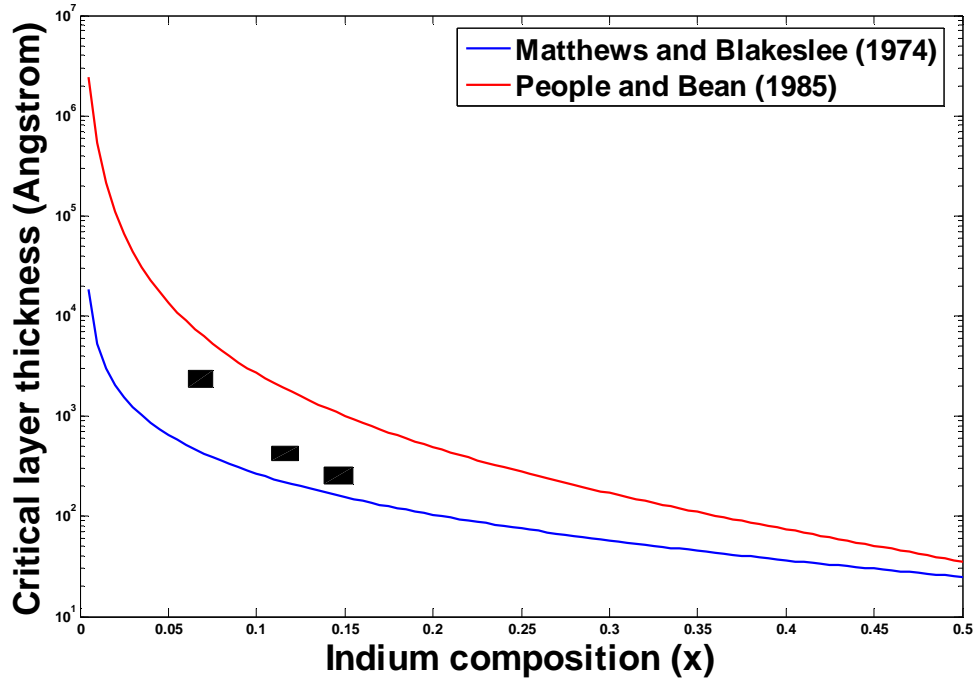


Figure 6.13: Theoretical and experimental values of critical thickness versus composition. The solid squares represent our experimental data, while the lines represent values predicted by two different theoretical models.

6.3 InAsSb

6.3.1 Compositional dependence of optical phonon frequencies

The mode behaviour observed in $\text{In}_x\text{Ga}_{1-x}\text{As}$, which was discussed in section 6.2.2, is not unique to this system, but also occurs in other III-V ternary alloys, such as $\text{InAs}_{1-x}\text{Sb}_x$ and $\text{In}_x\text{Ga}_{1-x}\text{Sb}$. In this section, the mode behaviour for the $\text{InAs}_{1-x}\text{Sb}_x$ ternary alloy is presented.

Samples with nominally the same thickness ($\sim 2.5\mu\text{m}$) but different Sb mole fractions were grown on GaAs 2° off (100) substrate. The composition of each layer was determined from XRD and ranged between 0.042 and 0.17. Raman spectra for these layers are shown in figure 6.14. The spectrum of a bulk InAs is also included for comparison. As expected, the InAs-like LO mode dominates, since the TO mode is forbidden for this configuration. The weak TO mode that is observed may be due to the departure from a pure backscattering geometry or to the presence of disorder (Li *et al.* 1992). With an increase in Sb content, both the InAs-like LO and TO vibrational modes shift away from the InAs optical mode region towards the InSb optical mode region.

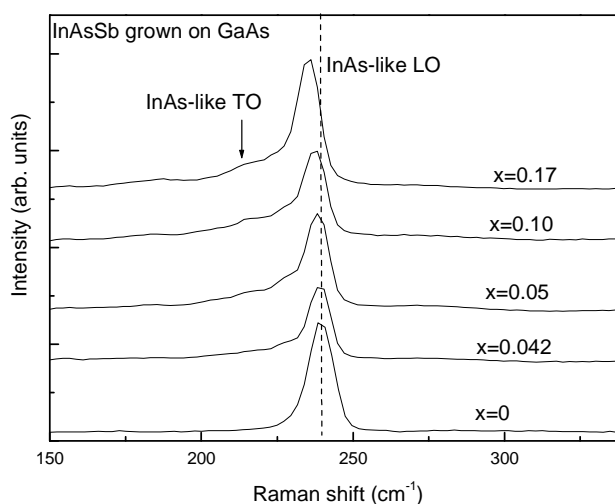


Figure 6.14: Raman spectra of $\text{InAs}_{1-x}\text{Sb}_x$ layer grown on GaAs 2° off (100) substrate with varying composition.

In the case of $\text{InAs}_{1-x}\text{Sb}_x$, the arsenic mass (74.92 a.u.) is bigger than the InSb reduced mass (59.1 a.u.). In this case, it is expected that $\text{InAs}_{1-x}\text{Sb}_x$ does not exhibit two-mode behaviour as discussed in section 3.3.4. However studies by Li *et al.* (1992) reported that the $\text{InAs}_{1-x}\text{Sb}_x$ ternary system does exhibit two-mode behaviour over the whole composition range. Figure 6.15 compares the compositional dependence of the phonon frequencies reported by Cherng *et al.* (1988) and Li *et al.* (1992) to the present results.

The results of this study exhibit the same trend for the variation with composition as those of Cherng *et al.* and Li *et al.* However, the present results are much closer to those reported by Li *et al.*, than those reported by Cherng *et al.* Results by Cherng *et al.*, appear to be scattered and there is a sudden change from one-mode to two-mode behaviour at ~ 0.6 . This discrepancy in the mode behaviour is believed to be related to the growth conditions of the samples studied (Li *et al.* 1992).

Li *et al.* reported that for the InAs-like LO mode frequency, the dependence on composition was linear and represented by the relationship:

$$\nu_{\text{InAs(LO)}} (\text{cm}^{-1}) = 238 - 32x \quad (6.8)$$

The InAs-like TO ($x \leq 0.23$) phonon frequency decreases with composition according to a linear relationship:

$$\nu_{\text{InAs(TO)}} (\text{cm}^{-1}) = 219 - 27x \quad (6.9)$$

The InSb-like LO mode frequency increases with composition and it is given by the relation:

$$\nu_{\text{InSb(LO)}} (\text{cm}^{-1}) = 177 + 12x \quad (6.10)$$

According to the work of Li *et al.* (1992), both the InAs-like and InSb-like LO modes are observed through the entire composition range, showing that the $\text{InAs}_{1-x}\text{Sb}_x$ ternary system exhibits “two-mode behaviour” (Chang and Mitra, 1968). This is contrary to the work of Cherng *et al.* (1988), in which mixed mode behaviour was reported. Cherng *et al.* observed that $\text{InAs}_{1-x}\text{Sb}_x$ displays one-mode behaviour for optical phonons, in the composition range $0 \leq x \leq 0.6$ and two-mode behaviour through the range $x > 0.6$.

Li *et al.* observed a weak peak at $\sim 138\text{cm}^{-1}$ for the entire composition range, while another peak at $\sim 154\text{cm}^{-1}$ was reported for $x \geq 0.7$. In both cases the frequency does not depend on x (Li *et al.* 1992). For layers with $x \leq 0.6$ Cherng *et al.* identified a broad band at $\sim 160\text{cm}^{-1}$, which was ascribed to disorder activated longitudinal acoustic (DALA) phonons (Cherng *et al.*, 1988). These DALA bands have also been observed in AlGaAs (Saint-Cricq *et al.* 1981) and InGaAs (Kakimoto and Katoda, 1982).

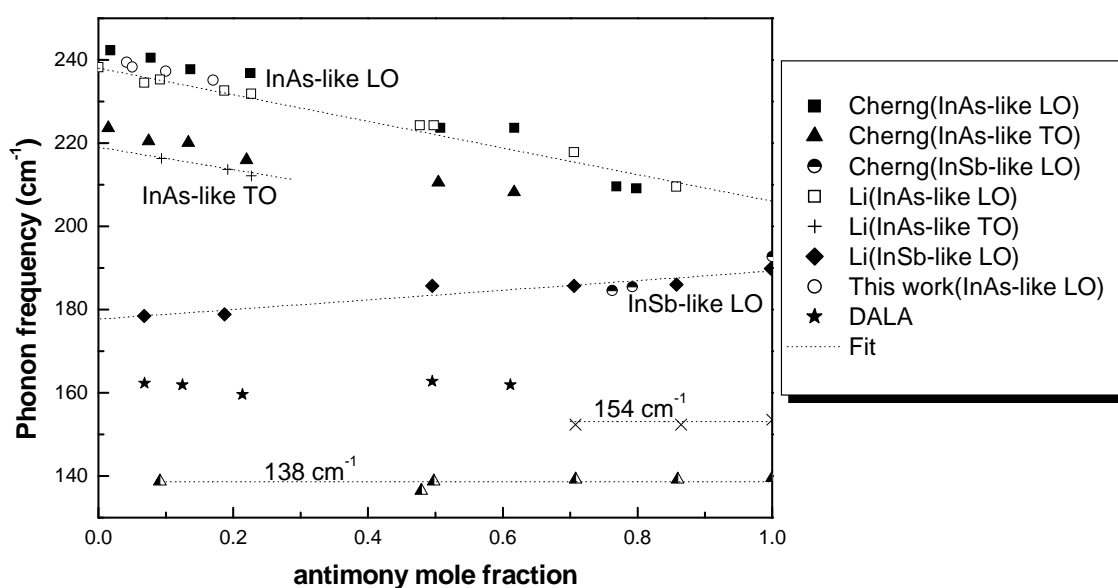


Figure 6.15: Compositional dependence of the phonon frequency in $\text{InAs}_{1-x}\text{Sb}_x$.

6.4 InGaSb

6.4.1 Incorporation of indium into GaSb lattice

Figure 6.16 shows the X-ray diffraction spectra of $\text{In}_x\text{Ga}_{1-x}\text{Sb}$ layers grown on 2° off (100) GaSb. The layers have nominally the same thickness ($\sim 2\ \mu\text{m}$). The increase in lattice mismatch is clearly indicated by the increased separation between the 400 reflection $K\alpha$ of layers relative to those of the GaAs substrate.

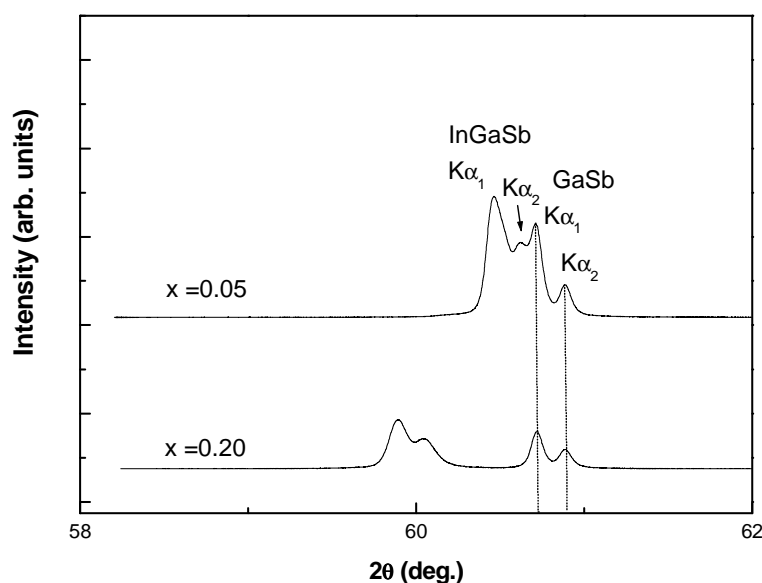


Figure 6.16: X-ray diffraction curves for the (400) reflection from $\text{In}_x\text{Ga}_{1-x}\text{Sb}$ layers of various compositions.

6.4.2 Compositional dependence of optical phonon frequencies

A series of four $\text{In}_x\text{Ga}_{1-x}\text{Sb}$ samples with nominally the same thickness ($\sim 2\ \mu\text{m}$) and In mole fractions x of 0.05, 0.10, 0.20 and 0.24 have been studied by Raman spectroscopy. Samples were grown on 2° off (100) GaSb substrate. The spectrum of a GaSb substrate included for comparison. Figure 6.17 shows the effect of composition on the optical phonon frequencies. The behaviour observed here is similar to that previously reported

for $\text{In}_x\text{Ga}_{1-x}\text{As}$ (Yamazaki *et al.* 1980) and $\text{InAs}_{1-x}\text{Sb}_x$ (Cherng *et al.* 1988). As expected, the GaSb-like LO mode is dominant in the spectra, and there is a vibrational mode shift to lower frequencies with increasing indium content. As previously mentioned for $\text{In}_x\text{Ga}_{1-x}\text{Sb}$ with low indium content, the reason that the InSb mode is not observed, is that the impurity mode produced by indium in the GaSb lattice is degenerate in frequency with phonons of the GaSb host (Brodsky *et al.* 1970).

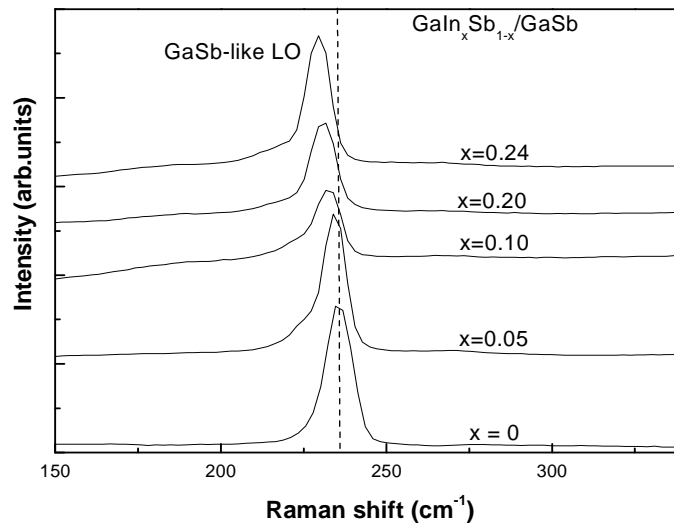


Figure 6.17: Room temperature Raman spectra of $\text{In}_x\text{Ga}_{1-x}\text{Sb}/\text{GaSb}$.

Figure 6.18 compares the compositional dependence of the LO and TO phonon frequencies reported by Brodsky *et al.* (1970), to the present results. The results of this study exhibit the same trend with a variation in composition as those of Brodsky *et al.* It is clear that the phonon GaSb-like frequencies measured in this study decrease linearly with an increase in indium content. The variations in the GaSb-like LO phonon frequencies with composition are linear because of mode coupling by long-range forces (Brodsky *et al.* 1970). The data can be approximated by two linear regions; i.e. $x < 0.5$ and $0.5 \leq x \leq 1$.

The variation in the GaSb-like TO phonon frequency is approximated by two linear segments; for small indium content (i.e. $x < 0.3$), the GaSb-like TO mode decreases less rapidly with composition as compared to higher indium content (i.e. $x > 0.3$). For the InSb-like TO mode, the compositional variation is linear for $x > 0.4$. The results presented here for $\text{In}_x\text{Ga}_{1-x}\text{Sb}$ and the earlier results shown for $\text{In}_x\text{Ga}_{1-x}\text{As}$ and $\text{InAs}_{1-x}\text{Sb}_x$ are representative of mixed mode behaviour discussed in section 3.3.3. For these materials the local mode is allowed, while the gap mode is not allowed (Brodsky *et al.* 1970). The local mode is produced by the substitution of In for Ga in GaSb.

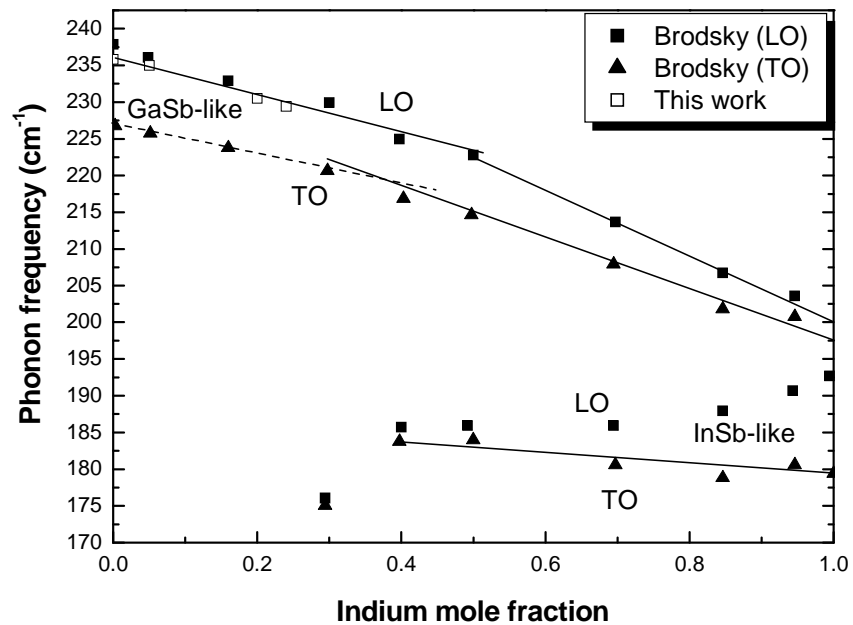


Figure 6.18: Compositional dependence of the phonon frequency in $\text{In}_x\text{Ga}_{1-x}\text{Sb}$. The lines are drawn to emphasize trends in the experimental data. The lines are guides to the eye.

6.4.3 Variation in optical phonon frequency with layer thickness

Just like $\text{In}_x\text{Ga}_{1-x}\text{As}/\text{GaAs}$, the lattice constants of GaInSb and GaSb are significantly different. In the case of thin layers, the lattice mismatch is accommodated by strain. As previously mentioned, beyond a critical thickness, the strain in the layer is relaxed by the formation of misfit dislocations at the interface.

Raman measurements were performed on five $\text{In}_x\text{Ga}_{1-x}\text{Sb}/\text{GaSb}$ layers with different thicknesses and an indium mole fraction $x = 0.21$. The layer thicknesses were chosen such that some layers should be fully strained, while others are partially relaxed or fully relaxed. The spectra obtained for the samples are shown in figure 6.19. It is clear that the optical phonons slightly shift to lower frequencies as the thickness of the epilayer increases. The phonon frequency changes at thicknesses above $0.01 \mu\text{m}$, thus it can be estimated that the critical thickness would range from $0.01 \mu\text{m}$ and $0.1 \mu\text{m}$. The estimation is compared to the predictions by People and Bean (1985); and Matthews and Blakeslee (1974). According to People and Bean model, the critical layer thickness for $x = 0.21$ is $\sim 0.04 \mu\text{m}$, while the Matthews and Blakeslee model predicts a critical layer thickness just below $0.01 \mu\text{m}$ for the same composition. As mentioned in section 6.5, the experimentally determined critical layer thickness is often greater than the Matthews and Blakeslee prediction.

A weak peak is observed at 188 cm^{-1} , the relative intensity of which appears to increase with thickness. It may be related to the defects induced as the lattice relaxes.

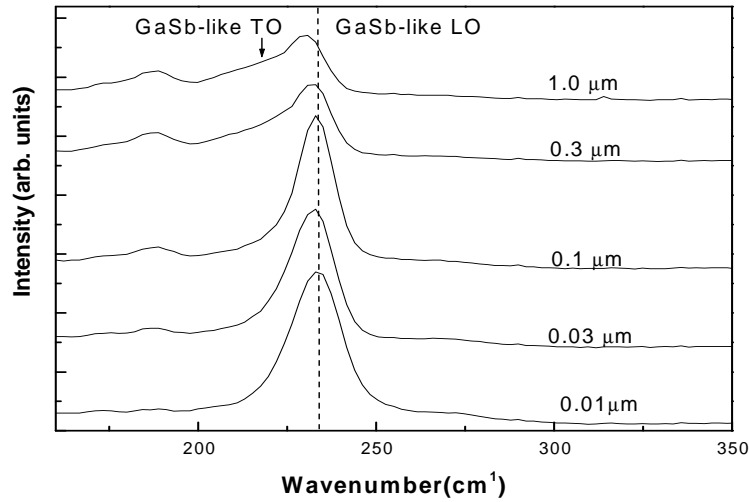


Figure 6.19: Raman spectra of $\text{In}_{0.21}\text{Ga}_{0.79}\text{Sb}/\text{GaSb}$ layers with thickness ranging from below to above critical thickness.

6.5 AlGaAs

6.5.1 Compositional dependence of optical phonon frequencies

In the case of a mixed crystal which exhibits two-mode behaviour, two optical bands are observed with frequencies characteristic of each binary end member and strengths roughly proportional to the respective concentrations (Jusserand, 1991). This is the behaviour expected for $\text{Al}_x\text{Ga}_{1-x}\text{As}$ (Jusserand, 1991). In this section four $\text{Al}_x\text{Ga}_{1-x}\text{As}$ samples grown on 2° off (100) GaAs substrate, with nominally the same thickness ($\sim 3 \mu\text{m}$) and mole fractions $x = 0.1, 0.23, 0.29$ and 0.36 , have been studied by Raman spectroscopy to confirm this mode behaviour.

Figure 6.20 shows the influence of composition on the variation in optical phonon frequencies. Two distinct Raman peaks belonging to GaAs-like LO and AlAs-like LO phonon modes and which lie below the pure GaAs and AlAs zone-center ones, respectively, are clearly observed. The GaAs-like TO and AlAs-like TO appear weakly in the spectra. The strength and frequency of each mode depend on composition x (Ilegems and Pearson, 1970). Each band shifts as the Al content increases: the GaAs-like mode

shifts to lower frequencies as expected, while the AlAs-like mode approaches that of the phonon in pure AlAs (i.e. 406 cm^{-1}) as the Al mole fraction approaches one (Ilegems and Pearson, 1970). The shift in the GaAs-like mode to lower frequencies is accompanied by a decrease in intensity when the concentration of Al increases. These observations show that substitutional Al displays a pure local-mode behaviour in the GaAs host crystal (Ilegems and Pearson, 1970). The concept of local mode behaviour was discussed in section 3.3.4.

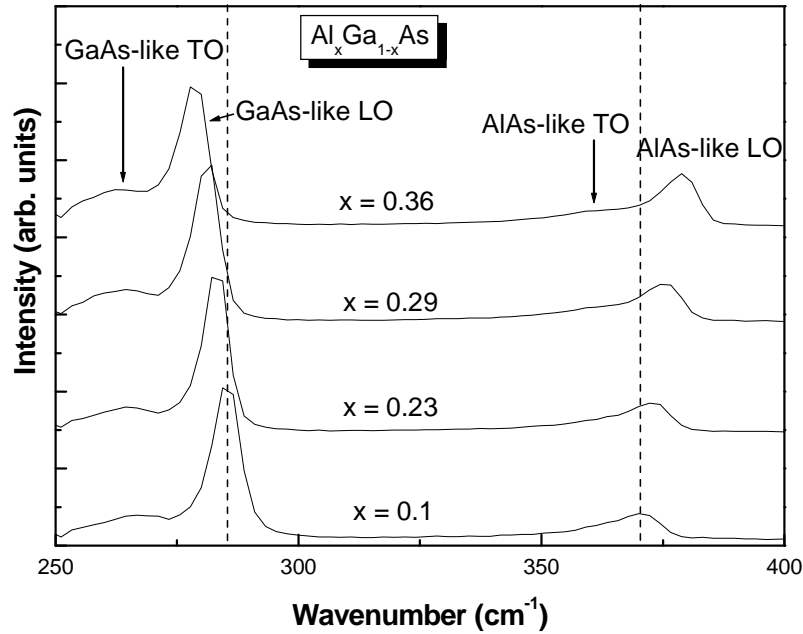


Figure 6.20: Room temperature Raman spectra of $\text{Al}_x\text{Ga}_{1-x}\text{As}/\text{GaAs}$.

It is expected that as the Al concentration increases, the GaAs-like phonon signal should broaden and become more asymmetric, while the reverse should happen for the AlAs-like phonon signal (Parayanthal and Pollak, 1984). In figure 6.20 the broadening of the GaAs-like phonon signal is not observed, but a narrowing of the AlAs-like signal is observed with increasing Al content. Disorder induced effects in $\text{Al}_x\text{Ga}_{1-x}\text{As}$, have been investigated previously using Raman scattering by Jusserand and Sapriel (1981) and Lao *et al.* (1989). The first effect is the asymmetric broadening of the GaAs and AlAs peaks,

which is due to crystalline defects. Apart from the broadening, additional peaks have been observed due to longitudinal (around 200 cm^{-1}) and transverse (around 100 cm^{-1}) acoustic modes (Jusserand and Sapriel, 1981). The above-mentioned effects are not apparent or observed in this work. The absence of the latter mode is not surprising, since it is below the cut-off of the notch filter used in this work.

Figure 6.21 compares the concentration dependence of the optical phonon modes as measured in this work to previous reported results by Feng *et al.* (1993) and Jusserand and Sapriel (1981). The GaAs-like and AlAs-like TO frequencies were extracted from the spectra in the figure 6.20 by fitting multiple Gaussian functions. There is an excellent agreement between all the experimental results shown in the figure. Any slight discrepancies that do exist may be attributed to sample defects and compositional inhomogeneities or to inaccuracies in the determination of composition (Jusserand, 1991).

The solid lines in figure 6.21 are polynomial fits to all the data. The LO mode frequency of the GaAs-like band and the TO mode frequency of the AlAs-like band vary linearly with composition, while the AlAs-like LO band and GaAs-like TO band have a nonlinear variation. The GaAs-like LO phonon frequency dependence on composition is described by the expression:

$$\nu_{\text{GaAs(LO)}} (\text{cm}^{-1}) = 291.7 - 37.3x \quad (6.11)$$

while the AlAs-like TO phonon frequency is best described by the relationship:

$$\nu_{\text{AlAs(TO)}} (\text{cm}^{-1}) = 360.3 - 0.6x \quad (6.12)$$

The AlAs-like LO phonon signal compositional variation is given by:

$$\nu_{\text{AlAs(LO)}} (\text{cm}^{-1}) = 361.6 - 53.2x - 12.9x^2 \quad (6.13)$$

Finally, the compositional variation of the GaAs-like TO phonon frequency is given by the expression:

$$\nu_{\text{GaAs(TO)}} (\text{cm}^{-1}) = 267.4 + 1.17x - 16.5x^2 \quad (6.14)$$

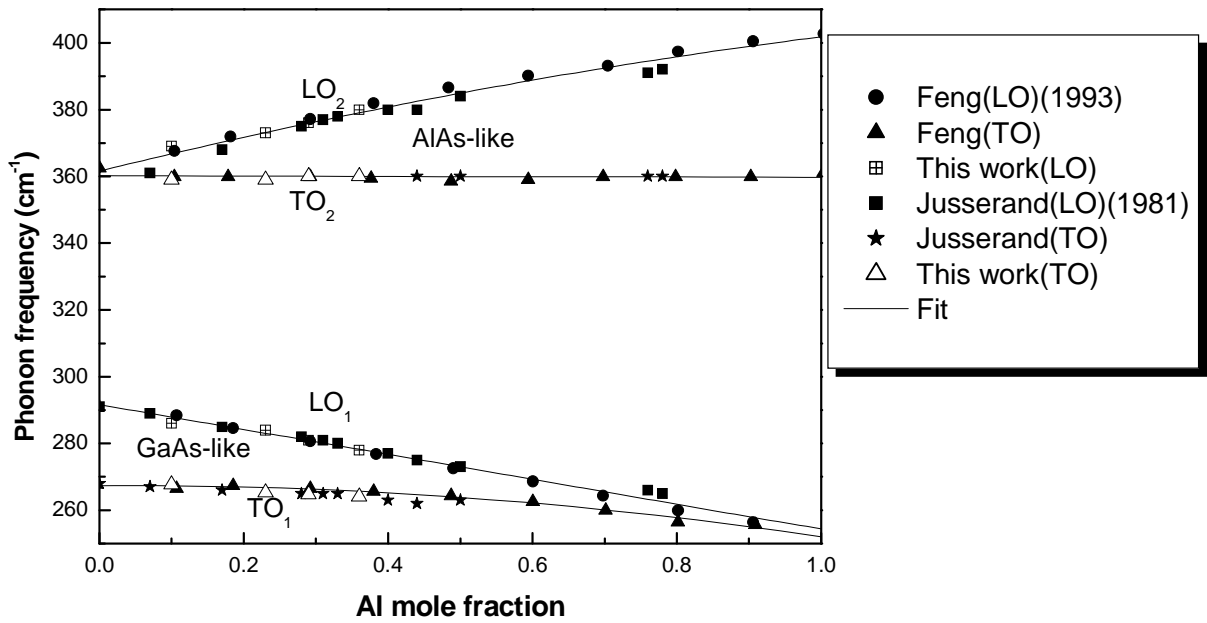


Figure 6.21: Compositional dependence of the phonon frequencies in $\text{Al}_x\text{Ga}_{1-x}\text{As}$. The solid lines are least-squares polynomial fits to the data.

Clearly the mode behaviour in $\text{Al}_x\text{Ga}_{1-x}\text{As}$ is different from that in $\text{In}_x\text{Ga}_{1-x}\text{As}$. For $\text{In}_x\text{Ga}_{1-x}\text{As}$ the behaviour was such that GaAs-like and the InAs-like bands merge into a single band at the In-rich end of the composition range (Ilegems and Pearson, 1969). As for $\text{Al}_x\text{Ga}_{1-x}\text{As}$, the bands remain well separated from each other for the entire composition range.

CHAPTER 7

CONCLUSIONS

The main objective of this work was to use a home-built Raman system for the characterization of $\text{In}_x\text{Ga}_{1-x}\text{As}$, $\text{InAs}_{1-x}\text{Sb}_x$, $\text{In}_x\text{Ga}_{1-x}\text{Sb}$ and $\text{Al}_x\text{Ga}_{1-x}\text{As}$ ternary systems.

InGaAs

The ability of Raman scattering to analyse a wide compositional range was used for the analysis of $\text{In}_x\text{Ga}_{1-x}\text{As}$ ternary alloys. A series of relaxed layers with nominally the same thickness and varying In mole fraction ($0 \leq x \leq 0.25$) were studied. Also included was an $\text{In}_{0.53}\text{Ga}_{0.47}\text{As}$ layer nominally lattice matched to InP(100). The layers were investigated to assess the effect of the incorporation of indium into the GaAs lattice.

The InGaAs spectra were dominated by GaAs-like LO modes at higher wavenumbers and weak GaAs TO modes. The Raman spectra are very sensitive to disorder induced by alloying. The frequencies of the LO and TO phonons shifted as the In content changed. The optical phonon mode behaviour characteristic of $\text{In}_x\text{Ga}_{1-x}\text{As}$ was the so-called mixed mode behaviour; that is, GaAs-like phonon modes were observed over the composition range $x < 0.14$, while InAs-like phonon modes were observed only over the composition range $x \geq 0.14$. For lower In content, the InAs mode is too weak to be detected experimentally, because the oscillator strength for the InAs-like mode is essentially zero (Yamazaki *et al.*, 1980). The dependence of the phonon frequencies on alloy composition in both the one-mode and two-mode regions was explained on the basis of the criteria by Brodsky and Lucovsky (1968).

The variation of strain with layer thickness was investigated with the purpose of quantifying the strain. Measurements were performed on layers with the same

composition but different thicknesses. As expected, with increasing thickness the GaAs-like mode LO shifted to lower frequencies. The frequency shifts of the optical phonons show that the epilayer grows pseudomorphically up to a certain thickness, beyond which the strain is gradually released.

The critical layer thickness was investigated using Raman spectroscopy and XRD. It was noted that the important factor in the determination of the critical layer thickness is the sensitivity of the measuring technique. Raman is more accurate because of its higher sensitivity in detecting the effect of low defect densities as compared to XRD (Grurley *et al.* 1988). The results of this work were compared with published data. The experimental results obtained follow the same pattern as the published ones, for similar indium content.

InAs_{1-x}Sb_x

InAs_{1-x}Sb_x samples of the same thickness but different composition were also studied. The spectra were dominated by the strong InAs-like LO mode, while the TO mode was observed only as a weak signal. Both the LO and TO frequency modes decreased as the Sb content increased.

As mentioned in chapter 6.6, a Raman study by Cherng *et al.* (1988) suggested that the InAs_{1-x}Sb_x ternary system exhibited mixed mode behaviour. Contrary to Cherng *et al.*, two-mode behaviour was observed over the entire compositional range by Li *et al.* (1992). Both InAs-like and InSb-like bands were observed throughout the composition range. In this study, it was not possible to conclude with certainty what the mode behaviour of the InAs_{1-x}Sb_x ternary system is due to the limited compositional range of the sample investigated.

In_xGa_{1-x}Sb

The compositional dependence of the optical phonon frequencies of In_xGa_{1-x}Sb samples was also presented. The behaviour was the same as that reported for the In_xGa_{1-x}As ternary system. The dominant GaSb-like LO mode shifted to lower frequencies with increasing In content. The lower frequency mode i.e. the InSb mode, was not observed in this study.

The results of this study exhibited the same trend for the variation with composition as those of Brodsky *et al.* (1970). Phonon frequencies measured in this study displayed a linear decrease.

The variation of strain with layer thickness was also investigated. Measurements were performed on layers with the same composition but different thickness. The LO phonon frequency shifted slightly to lower frequencies as the thickness increased from 0.01 μm to 0.1 μm.

Al_xGa_{1-x}As

The compositional dependence of the phonon frequencies of Al_xGa_{1-x}As layers was studied. It was found that, whatever the composition of the alloy, the Raman spectra showed two distinct bands, one belonging to the GaAs-like phonon mode and the other to an InAs-like phonon mode. Each of them appeared as a TO and LO pair. Even though the GaAs-like TO modes appeared weakly, they were sufficiently visible to determine the TO frequencies by curve fitting. The strength and frequency of these two bands depended on composition. Both bands shifted as the Al content increased: the GaAs-like phonon mode shifted to lower frequencies, while the AlAs-like mode approached that of the pure AlAs phonon.

Clearly Al_xGa_{1-x}As displays two-mode behaviour. This behaviour is quite different from that which was observed in In_xGa_{1-x}As i.e. mixed mode behaviour.

Further work may include:

- Using a micro-Raman system, rather than a conventional Raman system. When combined with a microscope objective lens, Raman spectroscopy can probe material properties on a micron scale.
- Using Raman scattering together with photoluminescence (PL), for the composition and strain analysis of the III-V semiconducting compounds. The objective is to make sure that there is consistency in the measurements.
- The entire compositional range should be investigated, especially for $\text{InAs}_{1-x}\text{Sb}_x$ and $\text{In}_x\text{Ga}_{1-x}\text{Sb}$, where uncertainties regarding the mode behaviour remain.

REFERENCES

- Adachi S.**, *Physical Properties of III-V Semiconductor Compounds: InP, InAs, GaAs, GaP, InGaAs, and InGaAsP* (John Wiley and Sons, New York, 1992).
- Adachi S.**, in *Properties of lattice-mismatched and strained indium gallium arsenide*, edited by Bhattacharya P.K., EMIS Datareviews no.8 Series (INSPEC, IEE, 1993) ch. 2 p. 47-57.
- Asai H.**, and Oe K., J. Appl. Phys. **54** (1983) 2052.
- Ashcroft N.W.**, and Mermin N.D., *Solid State Physics* (Saunders College, Philadelphia, 1976).
- Anastassakis E.**, Pinczuk A., Burstein E., Pollak F.H., and Cardona M., Solid State Commun. **8** (1970) 133.
- Baranska H.**, Labudzinska A., and Terpinski J., *Laser Raman Spectroscopy* (Ellis Horwood Limited, England, 1987).
- Barker A.S.** and Verleur H.W., Solid State Commun. **5** (1967) 695.
- Barker A.S.** and Sievers A.J., Rev. Mod. Phys. **47** (1975) S1.
- Bauer G.** and Richter W., *Optical Characterization of Epitaxial Semiconductor Layers* (Springer, Heidelberg, 1996).
- Bellani V.**, Bocchi C., Ciabattini T., Franchi S., Frigeri P., Galinetto P., Geddo M., Germini F., Guizzetti G., Nasi L., Patrini M., Seravalli L., and Trevisi G., Eur. J. Phys. **B 56** (2007) 217.
- Berolo O.** and Woolley J.C., Proceedings of the 11th International Conference on the physics of Semiconductors (ICPS), Warsaw, 1972, p. 1420.
- Born M.** and Huang K., *Dynamical Theory of Crystal Lattices* (Clarendon Press, Oxford 1954) p. 367.
- Bouarissa N.**, Amrane N., Aourag H., Infrared Phys. Technol. **36** (1995) 755.
- Brodsky H.** and Lucovsky G., Phys. Rev. Lett. **21** (1968) 990.
- Brodsky H.**, Lucovsky G., Chen M.F., and Plaskett T.S., Phys. Rev. Lett. **2** (1970) 3303.
- Burns G.**, Wie C.R., Dacol F.H., Pettit G.D., and Woodall J.M., Appl. Phys. Lett. **51** (1987) 1919.

- Carles R.**, Saint-Cricq N., Renucci J.B., Renucci M. A. and Zwick A., *Phys. Rev. B* **22** (1980) 4804.
- Casey, Jr. H.C.** and Panish M.B., *Heterostructure Lasers, Part A: Fundamental Principles* (Academic, New York, 1978) chaps. 4 and 5.
- Cerdeira F.**, Buchenauer C. J., Pollak F.H., and Cardona M., *Phys. Rev. B* **5** (1972) 580.
- Chang I.F.** and Mitra S.S., *Phys. Rev.* **172** (1968) 924.
- Chang I.F.** and Mitra S.S., *Adv. Phys.* **20** (1971) 359.
- Cherng Y.T.**, Ma K.Y., and Stringfellow G.B., *Appl. Phys. Lett.* **53** (1988) 886.
- Coderre W.M.** and Woolley J.C., *Can. J. Phys.* **46** (1968) 1207.
- Cripps S.A.**, Hosea T.J.C., Krier A., Smirnov V., Batty P.J., Zhuang Q.D., Lin H.H., Liu Po-Wei. and Tsai G., *Thin Solid films* **516** (2008) 8049.
- Cullity D.B.**, *Elements of X-ray Diffraction*, 3rd edn. (Addison-Wesley Publishing Company, London, Inc., 1967).
- Davydov A.**, *Molecular Spectroscopy of Oxide Catalyst Surfaces* (John Wiley and Sons, New York, 2003).
- Dettman J.W.**, *Introduction to Linear algebra and Differential Equations* (McGraw-Hill Book Company, New York, 1986).
- Dodson B. W.** and Tsao J.Y., *Appl. Phys. Lett.* **51** (1987) 1325.
- Dolling G.** and Waugh J.L.T., in *Lattice Dynamics*, edited by R. F. Wallis (Pergamon Press Inc., New York, 1965) p. 19.
- Eckbreth A.C.**, *Laser Diagnostics for Combustion Temperature and Species* (Abacus Press, Cambridge, 1988).
- Emura S.**, Gonda S., Matsui Y., Hayashi, *Phys. Rev. B* **38** (1988) 3280.
- Estreza J.P.**, Stevens P.D., Glosser R., Duncan W.M., Kao Y.C., Liu H.Y., and Beam E.A., *Appl. Phys. Lett.* **61** (1992) 1927.
- Fang Z.M.**, Ma K.Y., Jaw D.H., Cohen R.M., Stringfellow G.B., *J. Appl. Phys.* **67** (1990) 7034.
- Fekete D.**, Cha K.T., Ballantyne J.M., and Eastman L.F., *Appl. Phys. Lett.* **49** (1986) 1659.

- Feng Z.C.**, Perkowitz., Kinell D.K., Whitney R.L., Talwar D.N., Phys. Rev. **B 47** (1993) 13466.
- Ferraro, J.R.**, Nakamoto K., and Brown C.W., *Introductory Raman spectroscopy*, 2nd end. (Academic Press, California, 2003).
- Fritz I.J.**, Appl. Phys. Lett. **51** (1987) 1080.
- Gal M.**, Taylor P.C., Usher B.F., and Orders P.J., J. Appl. Phys. **62** (1987) 3898.
- Guo L.W.**, Han Y.J, Hu C.Y., Tan P.H., Yang F.H., Haung Q., and Zhou J.M., Phys. Rev **B 65** (2002) 125325.
- Ganesan S.**, Maraudin A.A., and Oitman J., Ann. Phys. (N.Y.) **56** (1970) 556.
- Genzel L.**, Martin T.P., and Perry C. H., Phys. Status Solidi **B 62** (1974) 83.
- Giannozzi P.**, de Gironcoli S., Pavone P., and Baroni S., Phys. Rev. **B 43** (1991) 7231.
- Goldberg Yu.A.**, *Handbook Series on Semiconductor Parameters*, Vol 2, Levishtein M., Rumyantsev S., and Shur M. (Eds.), (World Scientific, London, 1996a) p. 191- 213.
- Goldberg Yu.A.**, *Handbook series on Semiconductor Parameters*, Vol 2, Levishtein M., Rumyantsev S., and Shur M. (Eds.), (World Scientific, London, 1996b) p. 89-110.
- Groenen J.**, Landa G., Carles R., Pizani P.S., and Gendry M., Appl. Phys. **82** (1997) 803.
- Grurley P. L.**, Fritz I.J., and Dawson L.R., Appl. Phys. Lett. **52** (1988) 377.
- Hilsum C.** and Rose-Innes A.C., *Semiconducting III-V Compounds* (Pergamon Press Inc., New York, 1961).
- Hornstra J.** and Bartels W.J., J.Cryst. Growth **44** (1978) 513.
- Hull R.** and Bean J.C., Crit. Rev .Solid State Mater. Sci. **17** (1992) 507.
- Ichimura M.** and Sasaki A., J. App. Phys. **60** (1986) 3850.
- Ilegems M.** and Pearson G. L., Phys. Rev. **B4** 1576 (1970) 1576.
- Ingle J.D.** and Crouch S.R., *Spectrochemical Analysis* (Prentice-Hall, Inc., Upper Saddle River, NJ, 1988).
- Jain S.C.**, Willander M., and Mases H., Semicond. Sci. Technol. **11**, (1996) 641.
- Jeganathan V.**, Ramakrishnan V., and Kumar J., Cryst. Res. Technol. **34** (1999) 1293.
- Jeon H.I.**, Cha S.S., Lim K.Y., Suh E.K., and Lee H.J., J. Korean Phys. Soc. **27** (1994) 237.
- Jusserand B.** and Sapriel J., Phys. Rev. B **24** (1981) 7194.

- Jusserand B.**, in *Physical Properties of Aluminium Gallium Arsenide*, edited by Adachi S., EMIS Datareviews no.7 Series (INSPEC, IEE, 1991) ch. 2 p. 30-35.
- Kakimoto K.** and Katoda T., *Appl. Phys. Lett.* **21** (1982) 826.
- Kim O.K.** and Spitzer W.G., *J. Appl. Phys.* **50** (1979) 4362.
- Kuan T.S.**, Keuch T.F., Wang W.I., and Wilkie E.L., *Phys. Rev. Lett.* **54** (1985) 201.
- Lao P.**, Wade T.C., Madhukar A., and Chen P., *J. Appl. Phys.* **65** (1989) 1676.
- Lee E.C.W.** and Mousavi P., *Final Year Engineering Physics Project*, The University of British Columbia, 2004.
- Li Y.B.**, Dosanjh S.S., Ferguson I.T., Norman A.J., de Oliveira A.G., Stradling R.A., and Zallen R., *Semicond. Sci. Technol.* **7** (1992) 567.
- Lucovsky G.** and Chen M.F., *Solid State Commun.* **8** (1970) 1397.
- Maiman T.H.**, *Stimulated optical radiation in ruby*, *Nature.* **187** (1960) 493.
- Marée P.M.J.**, Barbour J.C., van der Veen J. F., Kavanagh K.L., Bulle-Lieuwma C.W.T., and Vieggers M.V.A., *J. Appl. Phys.* **62** (1987) 4413.
- Matthews J.W.** and Blakeslee A.E., *J. Cryst. Growth* **27** (1974) 118.
- Matossi F.**, *J. Chem. Phys.* **19** (1951) 161.
- Mikhailova M.P.**, *Handbook Series on Semiconductor Parameters*, Vol.1, M. Levinshtein, S. Rumyantsev and M. Shur, (Eds.), (World Scientific, London 1996) p. 147-168.
- Morris .D.**, Roth A .P., Masut R.A., Lacelle C., and Brebner J.L., *J. Appl. Phys.* **64** (1988) 4135.
- Muggli Z.** and Anderson M.E., *Solid State Technology*, **28** (1985) 287.
- Murakami N.**, Arafune K., Koyama T., Kumagwa M., Hayakawa Y., *J. Cryst. Growth* **275** (2005) 433.
- Orders P.J.** and Usher B.F., *Appl. Phys. Lett.* **50** (1987) 990.
- Ozolinsh J.V.**, Averkieva G.K., Ilvinsh A.F., Goryunova N.A., *Sov. Phys. Cryst.* **7** (1963) 691.
- Parayanthal P.** and Pollak F.H., *Phys. Rev. Lett.* **52** (1984) 1822.
- Pearsall T.P.**, Carles R., and Portel J.C., *Appl. Phys. Lett.* **42** (1983) 436.
- Pelletier M.J.**, *Analytical Application of Raman Spectroscopy* (Blackwell Science Ltd, Malden MA., USA, 1999).

- People R.** and Bean J.C., Appl. Phys. Lett. **49** (1985) 229.
- Pickering C.**, J. Electron. Mater. **10** (1981) 901.
- Pierret R.F.**, Semiconductor fundamentals (Addison-Wisely Publishing, New-York, 1989).
- Pinczuk A.**, Worlock J.M., Nahory R.E., and Pollack M.A., Appl. Phys. Lett. **33** (1978) 461.
- Porto S.P.S.** and Wood D.L., Opt. Soc. Am. **52** (1962) 251.
- Raman C.V.** and Krishnan K.S., A New Type of Radiation. Nature. **121** (1928) 501.
- Rakovska A.**, Berger V., Marcadet X., Vinter B., Bouzehoune K., and Kaplan D., Semicond. Sci. Technol. **15** (2000) 34.
- Reithmaier J.P.**, Cerva H., and Losch R., Appl. Phys. Lett. **54** (1989) 48.
- Saint-Cricq N.**, Carles R., Renucci J.B., Zwick A., Renucci M.A., Solid State Commun. **39** (1981) 1137.
- Sanchez J.J.**, Tijero J.M.G., Hernando J., Sanchez-Rojas J.L., Izpura I., J. Electron. Mater. **30** (1999) 363.
- Schroeder P.A.**, Infrared Spectroscopy in clay science: In CMS Workshop Lectures, Vol. 11, *Teaching Clay Science*, A. Rule and S. Guggenheim, (Eds.), The Clay Mineral Society, Aurora, CO, (2002) 181-206.
- Shahid M.A.**, Mahajan S., Laughlin D.E., and Cox H.M., Phys. Rev. Lett. **58** (1987) 2567.
- Shin H.K.**, Lockwood D.J., Lacelle C., and Poole P.J., J. Appl. Phys. **88** (2000) 6423.
- Skoog D.A.** and Leary J.J., *Principles of Instrumental Analysis*, 4th edn. (Saunders College Publishing, Philadelphia, 1992).
- Smekal A.**, Naturwiss. **11** (1923) 873.
- Sood A. K.**, Anastassakis E., and Cardona M., phys. Status Solidi **B 129** (1985) 505.
- Stringfellow G.B.** and Linnebach R., J. Appl. Phys. **51** (1980) 2212.
- Sze M.S.**, *Physics Semiconductor Devices* (John Wiley and Sons, New York, 1981).
- Tabata A.**, Benyattou T., Guillot G., Clark S.A., Macdonald J.E., Westwood D. I., and Williams R.H., Mater. Sci. Eng. **B 22** (1994) 222.
- Taylor D. W.**, Phys. Rev. **156** (1966) 1017.
- Thompson A.G.** and Woolley J.C., Can. J. Appl. Phys. **45** (1967) 2597.

- Van der Merwe J.H.**, J. Appl. Phys. **34** (1963) 123.
- Van dyk E.E.**, *PhD Thesis*, University of Port Elizabeth (1994).
- Van Vechten J.A.** and Bergstresser T.K., Phys. Rev. **B 1** (1970) 3351.
- Vankova V.**, *MSc Dissertation*, University of Port Elizabeth (2002).
- Vorlicek V.**, Moiseev K.D., Mikhailova M.P., Yakovlev Yu. P., Hulicius E., Simecek T., Cryst. Res. Technol. **37** (2002) 2-3.
- Vurgaftman L.**, Meyer J.R., Ram-Mohan L.R., J. Appl. Phys. **89** (2001) 5815.
- Welker Z.**, Naturforsch, **A 7** (1952) 744.
- Woolley J.C.** and Warner J., Can. J. Phys. **42** (1964) 1879.
- Yamazaki S.**, Ushirokawa A., and T. Katoda., J. Appl. Phys. **51** (1980) 3722.
- Yen M.Y.** and People R., Wecht K.W., J. Appl. Phys. **64** (1988) 952.
- Yu. P.Y.** and Cardona M., *Fundamentals of Semiconductors* (Springer, Heidelberg, 1996).